

# **DEVELOPMENT OF TUNGSTEN INERT GAS AND MICROWAVE TREATED CLADDINGS IN IMPROVING RESISTANCE TO WEAR AT ELEVATED TEMPERATURES**

Thesis

Submitted in partial fulfillment of the requirements for the degree of

**DOCTOR OF PHILOSOPHY**

by

**GUDALA SURESH**



DEPARTMENT OF MECHANICAL ENGINEERING  
NATIONAL INSTITUTE OF TECHNOLOGY KARNATAKA, SURATHKAL,  
MANGALORE – 575025

MAY, 2022

## DECLARATION

I hereby *declare* that the Research Thesis entitled “**DEVELOPMENT OF TUNGSTEN INERT GAS AND MICROWAVE TREATED CLADDINGS IN IMPROVING RESISTANCE TO WEAR AT ELEVATED TEMPERATURES**” which is being submitted to the **National Institute of Technology Karnataka, Surathkal** in partial fulfillment of the requirements for the award of the Degree of **Doctor of Philosophy in Department of Mechanical Engineering** is a *bonafide report of the research work carried out by me*. The material contained in this Research Thesis has not been submitted to any University or Institution for the award of any degree.

Register Number : 187033ME004

Name of the Research Scholar : GUDALA SURESH

Signature of the Research Scholar:



Department of Mechanical Engineering

Place : NITK, Surathkal

Date : 13-05-2022

## CERTIFICATE

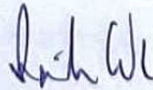
This is to *certify* that the Research Thesis entitled “**DEVELOPMENT OF TUNGSTEN INERT GAS AND MICROWAVE TREATED CLADDINGS IN IMPROVING RESISTANCE TO WEAR AT ELEVATED TEMPERATURES**” submitted by **Mr. GUDALA SURESH (Register Number: 187033ME004)** as the record of the research work carried out by him, is *accepted as the Research Thesis submission* in partial fulfillment of the requirements for the award of degree of **Doctor of Philosophy**.

**Research Guide**

  
13/05/2022  
**Dr. M R Ramesh**

Associate Professor

Department of Mechanical Engineering  
National Institute of Technology Karnataka



Chairman – DRPC

Date: 13.5.2022



## **ACKNOWLEDGMENT**

I would like to extend my gratitude to Dr. M R Ramesh, Associate Professor, Mechanical Engineering, National Institute of Technology Karnataka (NITK), Surathkal for the invaluable constructive guidance and encouragement extended throughout my study.

I would like to thank my Research Progress Assessment Committee members Dr. H. Shivananda Nayaka and Dr. A.V. Narasimhadhan for their valuable inputs.

I would like to thank Prof. Ravikiran Kadoli, Head of the Mechanical engineering department, and all the members of the faculty, Mechanical Engineering, NITK for their support throughout this research work.

Constant encouragement of my family to pursue higher studies has made it possible for me to reach this stage. I wish to thank all my family members for love, help, and encouragement provided. A special note of thanks to all my friends and well-wishers for their constant help, encouragement, and understanding.

## ABSTRACT

The remanufacturing of high-value engineering components is becoming a mainstream practice to reduce the environmental impact. The components such as cams, gears, and bearings rely on the integrity of their interacting surfaces where loads act over a small surface area, leading to high contact stresses, which may further influence the grater region of the surface. Especially at elevated temperatures, components used in the aero engine, gas and steam turbines, and bearings lose their efficiency due to the deterioration of material properties. The components used in such adverse conditions are important to adapt suitable surface modification techniques to increase the service life.

Cladding emerged as an effective surface modification technology and is widely used in many industries to protect the components against surface failures like wear, corrosion, and oxidation. Among many materials, titanium has numerous applications in a rocket motor, structural forgings and fasteners, pressure vessels, chemical gas pumps, marine components, and steam turbine blades, etc. Even though titanium alloy has a high specific strength and elevated melting temperature, it has low hardness and poor wear resistance. Hence the improvement of surface mechanical properties of titanium is essential to extend its application in an abrasive environment. The present work explores the TIG cladding technique and microwave hybrid heating (MHH) technique to enhance the surface properties of the titanium 31 alloy against wear at elevated temperatures.

Commercially available materials such as NiCrSiB/WC, Ag, BaF<sub>2</sub>, MoS<sub>2</sub>, and hBN are used as the cladding powders. Four types of composite coatings were prepared, namely NiCrSiB/WC/Ag/BaF<sub>2</sub>, NiCrSiB/WC/Ag/hBN, NiCrSiB/WC/MoS<sub>2</sub>/BaF<sub>2</sub>, and NiCrSiB/WC/MoS<sub>2</sub>/hBN, and deposited on Titanium 31 grade alloy substrate by TIG cladding and microwave cladding techniques at optimized parameters. The claddings were characterized using Scanning Electron Microscope (SEM), Energy Dispersive Spectroscopy (EDS), Electron Backscatter Diffraction (EBSD), and X-ray diffraction (XRD). Further, claddings are characterized for microstructural and mechanical properties (porosity, dilution, microhardness, fracture toughness) and evaluated their potential for high temperature environments in sliding wear conditions. At optimized

TIG and microwave hybrid techniques, less porosity (< 2%) and dilution were obtained.

The influence of solid lubricants, namely Ag, BaF<sub>2</sub>, MoS<sub>2</sub>, and hBN, on NiCrSiB/WC claddings is dealt with for tribological performance at elevated temperatures. Dry sliding wear behavior of titanium 31 substrate, NiCrSiB/WC/Ag/BaF<sub>2</sub>, NiCrSiB/WC/Ag/hBN, NiCrSiB/WC/MoS<sub>2</sub>/BaF<sub>2</sub>, and NiCrSiB/WC/MoS<sub>2</sub>/hBN is evaluated using high temperature pin on disc tribometer. All four coatings showed a synergistic lubrication effect at low and high temperatures. Due to the reduction of surface contact against the alumina counter body, claddings displayed a lower friction coefficient and wear rate than the substrate. Based on the weight loss data, the relative wear resistance of the both TIG and microwave claddings under dry sliding conditions is arranged in the following sequence: NiCrSiB/WC/Ag/BaF<sub>2</sub> > NiCrSiB/WC/Ag/hBN > NiCrSiB/WC/MoS<sub>2</sub>/hBN > NiCrSiB/WC/MoS<sub>2</sub>/BaF<sub>2</sub>. The combined lubricating effect of Ag and BaF<sub>2</sub> solid lubricants incorporated in the claddings was adequate to reduce material loss than other composite claddings. Comparatively, TIG processed clads showed lower wear rates than the MHH clads at all wear testing conditions. Developed claddings in the present study exhibit higher temperature resistance than titanium 31 alloy substrate making them suitable for components subjected to elevated temperature service conditions.

**Keywords:** *TIG cladding; Microwave Hybrid heating; Nickel-based alloy; Solid lubricants; Microstructure; High temperature wear.*

## CONTENT

Declaration	
Certificate	
Acknowledgment	
Abstract	
LIST OF FIGURES .....	5
LIST OF TABLES .....	13
ABBREVIATIONS .....	15
1. INTRODUCTION .....	17
1.1 CLADDING AS A SURFACE ENGINEERING METHOD .....	20
1.1.1 TIG Cladding .....	25
1.1.2 Microwave Cladding .....	27
1.2 Cladding materials .....	29
1.2.1 Nickel based alloys .....	30
1.2.2 Solid lubricants .....	31
2. Literature review .....	33
2.1 Nickel-based alloys .....	33
2.2 Self-lubricating coatings .....	36
2.3 TIG cladding .....	39
2.4 Microwave cladding .....	41
2.5 High temperature tribological studies .....	44
2.6 Objectives of the work .....	47
2.7 Outline of the thesis .....	48
3. Materials and Methods .....	49
3.1 Substrate .....	49
3.2 Coating material .....	49

3.3 TIG cladding .....	50
3.4 Microwave cladding .....	51
3.5 Porosity and dilution of the samples .....	53
3.6 Microhardness, fracture toughness and interfacial strength.....	53
3.7 Microstructure and phase analysis .....	54
3.8 Sliding wear test .....	54
4. RESULTS AND DISCUSSIONS .....	57
4.1 Morphology of the cladding powders .....	57
4.2 Visual inspection of the deposited clads .....	58
4.3 Porosity and dilution of the claddings.....	60
4.4 Microhardness and fracture toughness of the claddings .....	61
4.5 Microstructure of the deposited clads .....	63
4.5.1 NiCrSiB/WC TIG claddings.....	63
4.5.2 NiCrSiB/WC/Ag/BaF <sub>2</sub> TIG claddings.....	65
4.5.3 NiCrSiB/WC/Ag/hBN and NiCrSiB/WC/MoS <sub>2</sub> /hBN TIG claddings.....	70
4.5.4 NiCrSiB/WC/MoS <sub>2</sub> /BaF <sub>2</sub> TIG claddings.....	73
4.5.5 NiCrSiB/WC MHH clad.....	74
4.5.6 NiCrSiB/WC/Ag/BaF <sub>2</sub> MHH clad.....	75
4.5.7 NiCrSiB/WC/Ag/hBN and NiCrSiB/WC/MoS <sub>2</sub> /hBN MHH clads.....	78
4.5.8 NiCrSiB/WC/MoS <sub>2</sub> /BaF <sub>2</sub> MHH clad.....	81
4.6 Phase analysis of the clads .....	84
4.6.1 XRD analysis of the NiCrSiB/WC and NiCrSiB/WC/Ag/BaF <sub>2</sub> TIG clads.	84
4.6.2 XRD analysis of the NiCrSiB/WC/Ag/hBN and NiCrSiB/WC/MoS <sub>2</sub> /hBN TIG clads.....	84
4.6.3 XRD analysis of the NiCrSiB/WC/ and NiCrSiB/WC/ Ag/BaF <sub>2</sub> MHH clads.....	85
4.6.4 XRD analysis of the NiCrSiB/WC/Ag/hBN and NiCrSiB/WC/MoS <sub>2</sub> /hBN MHH clads.....	86



4.6.5 XRD analysis of the NiCrSiB/WC/MoS <sub>2</sub> /BaF <sub>2</sub> clads processed by TIG and MHH techniques.....	87
4.7 High temperature tribological performance of coatings .....	88
4.7.1 NiCrSiB/WC and NiCrSiB/WC/Ag/BaF <sub>2</sub> TIG claddings.....	88
4.7.2 NiCrSiB/WC and NiCrSiB/WC/Ag/BaF <sub>2</sub> MHH claddings.....	95
4.7.3 NiCrSiB/WC/Ag/hBN and NiCrSiB/WC/MoS <sub>2</sub> /hBN TIG claddings.....	101
4.7.4 NiCrSiB/WC/Ag/hBN and NiCrSiB/WC/MoS <sub>2</sub> /hBN MHH claddings...	108
4.7.5 TIG and MHH claddings of NiCrSiB/WC/MoS <sub>2</sub> /BaF <sub>2</sub> .....	116
4.7.6 Comparative Discussion.....	124
5. CONCLUSIONS.....	125



## LIST OF FIGURES

Figure 1. 1 Dilution of the clad.....	22
Figure 1. 2 Schematic of TIG Cladding.....	27
Figure 1. 3 Schematic representation of Microwave Cladding.....	28
Figure 3. 1 Experimental setup of the TIG cladding method.....	51
Figure 3. 2 Schematic representation of microwave hybrid heating mechanism. ....	52
Figure 3. 3 Vickers microhardness tester.....	54
Figure 3. 4 Pin on disc tribometer experimental set up. ....	56
Figure 4. 1 Morphology of the cladding powders (a) NiCrSiB/WC (b) NiCrSiB/WC/Ag/BaF <sub>2</sub> (c) NiCrSiB/WC/Ag/hBN (d) NiCrSiB/WC/MoS <sub>2</sub> /BaF <sub>2</sub> (e) NiCrSiB/WC/MoS <sub>2</sub> /hBN.....	57
Figure 4. 2 morphology of the solid lubricant powders (a) Ag (b) MoS <sub>2</sub> (c) BaF <sub>2</sub> (d) hBN.....	58
Figure 4. 3 Images of the TIG cladding layers processed at various process parameters (a) NiCrSiB/WC (b) NiCrSiB/WC/Ag/BaF <sub>2</sub> (c) NiCrSiB/WC/Ag/hBN (d) NiCrSiB/WC/MoS <sub>2</sub> /hBN (e) NiCrSiB/WC/MoS <sub>2</sub> /BaF <sub>2</sub> .....	59
Figure 4. 4 Images of the Microwave clads processed at optimized process parameters (a) NiCrSiB/WC (b) NiCrSiB/WC/Ag/BaF <sub>2</sub> (c) NiCrSiB/WC/Ag/hBN (d) NiCrSiB/WC/MoS <sub>2</sub> /hBN (e) NiCrSiB/WC/MoS <sub>2</sub> /BaF <sub>2</sub> .....	59
Figure 4. 5 Cross sectional SEM images of the NiCrSiB/WC clad processed at (a) 70 A (b) 95 A.....	64
Figure 4. 6 Magnified SEM image of NiCrSiB/WC clad at (a) clad-interface region; (b) substrate-interface region; (c) clad morphology.....	64
Figure 4. 7 EDX results of elemental distribution of NiCrSiB/WC clad in the selected regions (a) region A; (b) region B; (c) region C; (d) region d. ....	65

Figure 4. 8 Cross sectional SEM images of the NiCrSiB/WC/Ag/BaF <sub>2</sub> produced at the scanning speed of 2 mm/sec and process current of (a)70A; (b) 75A; (c) 80A; (d) 85A; (e) 90A; (f) 95A. ....	66
Figure 4. 9 Magnified cross sectional images of the NiCrSiB/WC/Ag/BaF <sub>2</sub> (a) Near to the interface of 70A current clad and clad morphology; (b) Near to the interface of 95A clad and clad morphology. ....	67
Figure 4. 10 EDX results of distribution of different phases in the NiCrSiB/WC/Ag/BaF <sub>2</sub> clad (a) phase A; (b) phase B; (c) phase C. ....	67
Figure 4. 11 EDX results of elemental distribution of NiCrSiB/WC/Ag/BaF <sub>2</sub> clad in the selected areas (a) Area D; (b) Area E; (c) Area F; (d) Area G .....	68
Figure 4. 12 EDX Elemental mapping of NiCrSiB/WC/Ag/BaF <sub>2</sub> clad cross section near to the top at 70A current .....	69
Figure 4. 13 EBSD IPF maps and grain distribution of the NiCrSiB/WC/Ag/BaF <sub>2</sub> clad along the cross-section. (a) IQ map at 70 A and (b) grain size distribution map at 70 A. (c) IPF map at 70 A, (d) IQ map at 95 A, (e) grain size distribution map at 95 A (f) IPF map at 95 A (g) grain size distribution in the fractioned area at 70 A and (h) grain size distribution in the fractioned area at 95 A. ....	<b>Error! Bookmark not defined.</b>
Figure 4. 14 Cross-sectional SEM images of the NiCrSiB/WC/Ag/hBN clad developed at the process current of (a) 90 A (b) 95 A (c) 100 A; NiCrSiB/WC/MoS <sub>2</sub> /hBN process current of (d) 90A (e) 95A (f) 100 A. ....	71
Figure 4. 15 Surface morphology of the NiCrSiB/WC/Ag/hBN clad (at different magnification) produced with a process current of (a) 90 A (b) 95 A (c) 100 A; NiCrSiB/WC/MoS <sub>2</sub> /hBN process current of (d) 90A (e) 95A (f) 100 A. ....	71
Figure 4. 16 (a) IPF map of coatng A at 90 A (b) Phase map at 90A (c) Grain distribution map at 90 A (d) IPF map of coatng A at 100 A (e) Phase map at 100A (f) Grain distribution map at 100 A. ....	<b>Error! Bookmark not defined.</b>
Figure 4. 17 Cross sectional SEM image of TIG clad produced at (a) 90 A (b) 100 A (c) 110 A. ....	73

Figure 4. 18 SEM image of TIG clad at 90 A (a) top region of the clad (b) bottom region of the clad (c) clad-substrate interface region.....	74
Figure 4. 19 (a) A typical cross-sectional FESEM image of NiCrSiB/WC microwave clad, (b) Top region of the clad at higher magnification. ....	75
Figure 4. 20 (a) The cross sectional morphology of NiCrSiB/WC/Ag/BaF <sub>2</sub> clad, (b) Bottom region (c) Top region. ....	76
Figure 4. 21 EDS analysis of the NiCrSiB/WC/BaF <sub>2</sub> clad in the regions of Fig 4c. (a) region A, (b) region B, (c) Region C.....	77
Figure 4. 22 EDS elemental distribution of various elements of NiCrSiB/WC/Ag/BaF <sub>2</sub> clad.....	77
Figure 4. 23 EBSD analysis of NiCrSiB/WC/Ag/BaF <sub>2</sub> clad (a) IQ map, (b) IPF map, (c) Phase map.....	<b>Error! Bookmark not defined.</b>
Figure 4. 24 Microstructure of the NiCrSiB/WC/Ag/hBN clad across the cross-section (a) clad area, (b) interface area, (c) dispersion of WC particles in the nickel alloy matrix, and (d) WC dissolution.....	79
Figure 4. 25 EDS elemental mapping of NiCrSiB/WC/Ag/hBN clad across the cross-section. ....	79
Figure 4. 26 Microstructure of the NiCrSiB/WC/MoS <sub>2</sub> /hBN clad across the cross-section (a) clad area, (b) interface area, (c) dispersion of WC particles in the nickel alloy matrix, and (d) WC dissolution.....	80
Figure 4. 27 EDS elemental mapping of NiCrSiB/WC/MoS <sub>2</sub> /hBN clad across the cross-section.....	80
Figure 4. 28 EBSD analysis on the cross section of NiCrSiB/WC/Ag/hBN clad (a) IPF map, (b) Phase map, and (c) grain size distribution map.	<b>Error! Bookmark not defined.</b>
Figure 4. 29 The cross-sectional SEM image of MHH clad.....	81
Figure 4. 30 SEM image of MHH clad (a) clad-interface region (b) just above the interface region (c) top region of the clad.....	82

Figure 4. 31 EDS analysis of MHH clad across the cross section (a) region A (b) region B (c) region C. ....	83
Figure 4. 32 EDS mapping of MHH clad across the cross section.....	83
Figure 4. 33 XRD patterns of the coatings at processing current 70A (a) NiCrSiB/WC clad (b) NiCrSiB/WC/Ag/BaF <sub>2</sub> clad.....	84
Figure 4. 34 XRD patterns of the clads developed at 90 A (a) NiCrSiB/WC/Ag/hBN clad (b) NiCrSiB/WC/MoS <sub>2</sub> /hBN clad. ....	85
Figure 4. 35 X-ray diffraction patterns of MHH clad (a) NiCrSiB/WC (b) NiCrSiB/WC/Ag/BaF <sub>2</sub> .....	86
Figure 4. 36 XRD patterns of NiCrSiB/WC/Ag/hBN (clad A) and NiCrSiB/WC/MoS <sub>2</sub> /hBN (clad B) clads.....	87
Figure 4. 37 X-ray diffraction pattern of NiCrSiB/WC/MoS <sub>2</sub> /BaF <sub>2</sub> clads deposited by (a) TIG cladding (90A) (b) MHH cladding. ....	88
Figure 4. 38 Variation of weight loss of the NiCrSiB/WC clad and NiCrSiB/WC/Ag/BaF <sub>2</sub> clad at different test temperatures and loads .....	89
Figure 4. 39 Friction coefficient of the coatings with respect to sliding time (a) Titanium 31 substrate at 200 °C (b) Titanium 31 substrate at 600 °C (c) NiCrSiB/WC clad at 200 °C (d) NiCrSiB/WC clad at 600 °C (e) NiCrSiB/WC/Ag/BaF <sub>2</sub> clad at 200°C (f) NiCrSiB/WC/Ag/BaF <sub>2</sub> clad at 600 °C .....	90
Figure 4. 40 SEM images of wear scars under 20N load (a) NiCrSiB/WC clad at 200°C; (b) 400°C; (c) 600°C; (d) NiCrSiB/WC/Ag/BaF <sub>2</sub> clad at 200°C; (e) 400°C; (f) 600°C.....	91
Figure 4. 41 SEM images of wear scars under 40N load (a) NiCrSiB/WC clad at 200°C; (b) 400°C; (c) 600°C; (d) NiCrSiB/WC/Ag/BaF <sub>2</sub> clad at 200°C; (e) 400°C; (f) 600°C.....	92
Figure 4. 42 EDX Elemental mapping of worn surface of NiCrSiB/WC/Ag/BaF <sub>2</sub> clad at 200°C, 20N loading condition.....	93

Figure 4. 43 EDX Elemental mapping of worn surface of NiCrSiB/WC/Ag/BaF <sub>2</sub> clad at 600°C, 20N loading condition.....	93
Figure 4. 44 XRD Patterns of worn surfaces of the NiCrSiB/WC clad at (a) 600°C (b) 200°C.....	94
Figure 4. 45 XRD Patterns of worn surfaces of the NiCrSiB/WC/Ag/BaF <sub>2</sub> clad at (a) 200°C (b) 600°C .....	95
Figure 4. 46 Variation of wear rate of both clads at various temperatures and loads..	96
Figure 4. 47 Variation in friction coefficient with respect to sliding time for NiCrSiB/WC clad (a) 200°C (b) 600°C (c) NiCrSiB/WC/Ag/BaF <sub>2</sub> clad at 200°C (d) 600°C.....	97
Figure 4. 48 The SEM images of NiCrSiB/WC/Ag/BaF <sub>2</sub> worn surfaces under 10N load: (a) 200°C, (b) 400°C, (c) 600°C; Under 20N load: (d) 200°C, (e) 400°C, (f) 600°C.....	98
Figure 4. 49 The SEM images of the worn surface at 20N load: NiCrSiB/WC at (a) 200°C, (b) 600°C; Titanium 31 substrate at (c) 200°C, (d) 600°C.....	98
Figure 4. 50 3d surface profiles of the worn surfaces. (a-c) NiCrSiB/WC/Ag/BaF <sub>2</sub> clad (d-f) NiCrSiB/WC clad. ....	99
Figure 4. 51 XRD analysis of NiCrSiB/WC/Ag/BaF <sub>2</sub> clad worn surface after sliding wear test at 20N load (a) 200°C, (b) 600°C. ....	100
Figure 4. 52 weight loss of NiCrSiB/WC/Ag/hBN clad and NiCrSiB/WC/MoS <sub>2</sub> /hBN clad at different temperatures and loads. ....	102
Figure 4. 53 Variation in coefficient of friction with respect to sliding time. ....	103
Figure 4. 54 Wear rate of the coated samples at different temperatures under various loads.....	103
Figure 4. 55 SEM images of the wear scars of NiCrSiB/WC/Ag/hBN (a) 200 °C, 20N (b) 400 °C, 20 N (c) 600°C, 20 N (d) 200 °C, 40 N (e) 200 °C, 40N (c) 600 °C, 40 N. ....	105

Figure 4. 56 SEM images of the wear scars of NiCrSiB/WC/MoS <sub>2</sub> /hBN clad (a) 200 °C, 20N (b) 400 °C, 20 N (c) 600°C, 20 N (d) 200 °C, 40 N (e) 200 °C, 40N (c) 600 °C, 40 N.....	105
Figure 4. 57 XRD patterns of the worn surfaces of NiCrSiB/WC/Ag/hBN clad at operating temperature of (a) 200 °C (b) 600 °C. ....	106
Figure 4. 58 XRD patterns of the worn surfaces of NiCrSiB/WC/MoS <sub>2</sub> /hBN clad at operating temperature of (a) 200 °C (b) 600 °C. ....	107
Figure 4. 59 3D surface profiles of the worn surfaces (a-c) NiCrSiB/WC/Ag/hBN clad (d-e) NiCrSiB/WC/MoS <sub>2</sub> /hBN clad.....	108
Figure 4. 60 Variation of coefficient of friction of NiCrSiB/WC/Ag/hBN clad (clad A) and NiCrSiB/WC/Mo <sub>2</sub> /hBN clad (clad B) at different temperatures and loads. .	109
Figure 4. 61 Wear rate of the NiCrSiB/WC clad and titanium alloy at different temperatures and loads.....	110
Figure 4. 62 Wear rate of NiCrSiB/WC/Ag/hBN clad (clad A) and NiCrSiB/WC/Mo <sub>2</sub> /hBN clad (clad B) at different temperatures and loads. ....	111
Figure 4. 63 FESEM images of the wear scars under 10 N (a) NiCrSiB/WC clad at 200 °C, (b) NiCrSiB/WC clad at 600 °C, (c) Titanium 31 alloy at 200 °C, and (d) Titanium 31 alloy at 600 °C. ....	112
Figure 4. 64 FESEM images of the wear surfaces of NiCrSiB/WC/Ag/hBN clad at (a) 200 °C:10 N, (b) 200 °C:20 N, (c) 400 °C:10 N, (d) 400 °C:20 N, (e) 600 °C:10 N, and (f) 600 °C:20 N.....	113
Figure 4. 65 FESEM images of the worn surfaces of NiCrSiB/WC/Mo <sub>2</sub> /hBN clad at (a) 200°C:10 N, (b) 200°C:20 N, (c) 400°C:10 N, (d) 400°C:20 N, (e) 600°C:10 N, and (f) 600°C:20 N.....	114
Figure 4. 66 XRD patterns of the NiCrSiB/WC clad after wear tests under 10 N load at (a) 200 °C, and (b) 600 °C. ....	115
Figure 4. 67 XRD patterns of the NiCrSiB/WC/Ag/hBN clad after wear tests under 10 N load at (a) 200 °C, (b) 400 °C, and (c) 600 °C.....	115



Figure 4. 68 XRD patterns of the NiCrSiB/WC/Mo <sub>2</sub> /hBN clad after wear tests under 10 N load at (a) 200 °C, (b) 400 °C, and (c) 600 °C.....	116
Figure 4. 69 3D optical profile of the worn surfaces under 10 N load: NiCrSiB/WC/Ag/hBN clad at (a) 200 °C, (b) 400 °C, (c) 600 °C, and NiCrSiB/WC/Mo <sub>2</sub> /hBN clad at (d) 200 °C, (e) 400 °C, (f) 600 °C. ....	116
Figure 4. 70 Variation of weight loss of NiCrSiB/WC/MoS <sub>2</sub> /BaF <sub>2</sub> TIG and MHH clads at various temperatures and loads.....	117
Figure 4. 71 Variation of friction coefficient with respect to sliding time for NiCrSiB/WC/MoS <sub>2</sub> /BaF <sub>2</sub> TIG clad at various temperatures and loads. ....	118
Figure 4. 72 SEM results of worn surfaces of NiCrSiB/WC/MoS <sub>2</sub> /BaF <sub>2</sub> TIG clads under 20 N load at (a) 200 °C (b) 400 °C (c) 600 °C, MHH clad under 20 N load at (d) 200 °C (e) 400 °C (f) 600 °C. ....	120
Figure 4. 73 SEM results of worn surfaces of NiCrSiB/WC/MoS <sub>2</sub> /BaF <sub>2</sub> TIG clads under 40 N load at (a) 200 °C (b) 400 °C (c) 600 °C, MHH clad under 40 N load at (d) 200 °C (e) 400° C (f) 600 °C. ....	121
Figure 4. 74 X-ray diffraction pattern of worn surface of NiCrSiB/WC/MoS <sub>2</sub> /BaF <sub>2</sub> MHH clad (90A) at (a) 200 °C (b) 600 °C, TIG clad at (c) 200 °C (d) 600 °C. ....	122
Figure 4. 75 3d surface profiles of the worn surfaces of NiCrSiB/WC/MoS <sub>2</sub> /BaF <sub>2</sub> TIG clad under 20 N load (a) 200 °C (b) 600 °C; texture profiles of TIG clad under 20 N (c) 200 °C (d) 600 °C.....	123
Figure 4. 76 3d surface profiles of the worn surfaces of NiCrSiB/WC/MoS <sub>2</sub> /BaF <sub>2</sub> MHH clad under 20 N load (a) 200 °C (b) 600 °C; texture profiles of MHH clad under 20 N (c) 200 °C (d) 600 °C.....	124



## LIST OF TABLES

Table 3. 1 Chemical composition (wt. %) of Titanium 31 alloy. ....	49
Table 3. 2 Chemical composition of NiCrSiB/WC composite powder (wt. %). ....	50
Table 3. 3 Composition of various coating powders for wear test (wt. %). ....	50
Table 3. 4 TIG cladding experimental processing conditions. ....	51
Table 3. 5 The microwave cladding processing conditions. ....	52
Table 3. 6 Wear test parameters.....	56
Table 4. 1 Porosity and dilution of the TIG clads.....	60
Table 4. 2 Porosity and dilution of the MHH clads. ....	61
Table 4. 3 Average microhardness values the TIG and MHH claddings. ....	62
Table 4. 4 Average fracture toughness of the TIG and MHH clads. ....	63
Table 4. 5 Elemental distribution of the selected regions from the NiCrSiB/WC clad EDX results.....	65
Table 4. 6 Elemental distribution of the selected phases and areas from the NiCrSiB/WC/Ag/BaF <sub>2</sub> clad EDX results.....	68
Table 4. 7 EDS analysis corresponding to SEM images shown in Fig. 3.....	72
Table 4. 8 R <sub>a</sub> values of the clads at various temperatures at 20N load.....	100



## ABBREVIATIONS

TIG	: Tungsten Inert Gas
MHH	: Microwave Hybrid Heating
Ag	: Silver
MoS <sub>2</sub>	: Molybdenum disulfide
hBN	: Hexagonal Boron Nitride
BaF <sub>2</sub>	: Barium Fluoride
Al <sub>2</sub> O <sub>3</sub>	: Aluminium Oxide
Cr	: Chromium
Cr <sub>23</sub> C <sub>6</sub>	: Chromium Carbide
Ni	: Nickel
NiO	: Nickel Oxide
TiO	: Titanium Oxide
Ag <sub>2</sub> F	: Silver subfluoride
SEM	: Scanning Electron Microscope
EBSA	: Electron Backscatter Diffraction
COF	: Coefficient of Friction



# CHAPTER 1

## INTRODUCTION

Surface engineering plays a vital role in modifying or changing surface properties. It is an interrelated activity that includes coatings technology accompanied for optimizing the surface properties with wear and other mechanical properties followed by the evolution of surfaces in terms of qualitative and quantitative characterization. Surface engineering techniques are being used in many sectors such as automotive, biomedical, textile, petroleum, petrochemical, aerospace, construction, etc (Cotell et al. 1994). In recent years, various technologies of been developed for the processing of materials. Based on the application, different surface engineering techniques are evolved. These techniques are usually used to enhance the required surface properties, including physical, chemical, magnetic, electronic, mechanical, wear, and corrosion resistance at the substrate surfaces. Recently, there has been a paradigm shift in surface engineering mechanisms from electroplating to efficient technologies such as physical vapor deposition (Mo and Zhu 2009), chemical vapor deposition (Sitek et al. 2013), thermal spray processes (Medabalimi et al. 2019; Prasad et al. 2019a; Ramesh et al. 2011), and welding using advanced heat sources like a laser (Torres et al. 2018), ion (Budzynski et al. 2006), electron (Weglowski et al. 2015), plasma (da Silva et al. 2019), and microwave (Gupta and Sharma 2011a; Mishra and Sharma 2017a; Prasad et al. 2018), etc. Many engineering components require surface engineering treatment to attain benefits such as lower manufacturing costs, easy recyclability, increased lifetime, lower environmental impact, etc.

Tribology is also one of the main causes of rising energy dissipation, environmental emissions, and overall operating costs globally. The overall energy consumption due to tribological issues is increasing primarily because of industrial sector growth. The required performance levels of machinery and mechanical components are also raised to some extent. So, the reduction of adverse effects of failures is essential for achieving better surface characteristics. The surface is crucial for most material failures like wear, fatigue, and corrosion (Dearnley 2017). The

degree of surface degradation due to various tribological failures can be evaluated based on multiple experimental procedures. Among those wear is the predominant phenomenon found on any surface. This ubiquitous failure especially appears on solid surface interaction with the working environment, including a type of load, nature of the contact, and type of opposing material. Wear is the gradual deterioration of a solid surface caused by the mechanical action of a working medium (solid, liquid, and gas). It is an inevitable phenomenon that typically induces a degree of material degradation. Wear can be classified in numerous ways based on the nature of the contact, mechanism of operation and lubrication conditions, etc. Wear can be broadly categorized as mechanical, chemical, and thermal wear. However, these are not sufficient to predict wear rates and models. The descriptive term mechanical wear elucidates different wear modes: adhesive, abrasive, erosive, and fatigue wear. Similarly, chemical wear explains tribo-chemical reactions at the contact surface due to the medium of lubricants and air. Thermal wear happens because of the melt zone due to frictional heating. The nature of the contact of the material and surface contact condition are the main factors for optimal surface roughness, further influencing friction. Thermal spraying has been widely used for surface modification by depositing coatings among several surface engineering techniques owing to its high versatility. However, thermal spraying causes poor metallurgical bonding, oxides, and porosity. Also, it further leads to the delamination of coating and reduction of wear properties. The arc-assisted surface engineering method like TIG (tungsten inert gas) cladding could be a better alternative to overcome these limitations. This method helps in achieving better metallurgical bonding between the coatings and the substrate. Also, recently, the processing of bulk metallic materials with microwave energy gained attention because of its rapid and uniform bulk heating characteristics. The melting of bulk metallic materials using microwave energy reduces power consumption (2-3 times) significantly than other conventional sources and offers atomic level heating in less time (Chandrasekaran et al. 2011; Mishra and Sharma 2017b). Due to the volumetric level of heating, thermal distortion, porosity, and crack formation reduced significantly.

Substrates such as stainless steel, aluminum, nickel, titanium, and copper are generally suitable for cladding. The substrate must also have sufficient thermal



conductivity to form a metallurgical bond. Titanium alloys are promising structure materials mainly used in aviation and marine industries due to their high specific strength and low density. Titanium has a very high melting point (1678 °C), indicating good creep resistance over a significant temperature range. In addition to aerospace applications, these attractive high-temperature properties have been extended to field turbines. To improve the surface properties of titanium alloys, such as high temperature tribological and corrosion aspects, the usual approach is to modify the surface with the material having higher hardness and lower coefficient friction than the substrate. They have a great potential to overcome limitations caused by steel and aluminum in the aerospace industry (Gogia 2005). However, the functionality of titanium alloys in practical industrial fields like intermediate brakes, fans, bearings, and compressor plates is limited because of their low hardness and poor wear resistance (Zhao et al. 2019). Also, they are widely applied in aerospace, medical, and automotive industries due to their superior material properties under extreme environmental conditions. The surface mechanical properties of the titanium alloys can be improved using several surface modification techniques to extend their application in severe environments (Mendez et al. 2014). Nickel-based alloys can be used as the coating material to protect the surface from wear, fatigue, and corrosion (Weng et al. 2016). However, nickel-based alloy coatings are ineffective without hard ceramic phases such as TiC, WC, SiC, Cr<sub>2</sub>C<sub>3</sub>, and Al<sub>2</sub>O<sub>3</sub> (Zhou et al. 2008). Among those, tungsten carbide is a rigid material that exhibits excellent corrosion and wear properties. It is widely used in cutting tools, drilling, and preparing corrosion-resistant coatings (Sabzi et al. 2018a). Also, ceramic inclusion causes no change in density and other internal properties of the coatings. Hard composite coatings show greater wear resistance. However, they are susceptible to cracking (Luo et al. 2015). It is challenging to determine the optimum amount of ceramic phase required to prepare the coating to improve the essential material properties (Fallah et al. 2010; Tian et al. 2010; WANG et al. 2009). Further, the ceramic phase possesses higher frictional values at elevated temperatures. The subsequent addition of solid lubricant reduces frictional values. Friction is the resistance force that occurs when two relative surfaces contact each other. The coefficient of friction of the surface can be calculated using the frictional force divided by the normal load on the contact. For lubricated contacts,

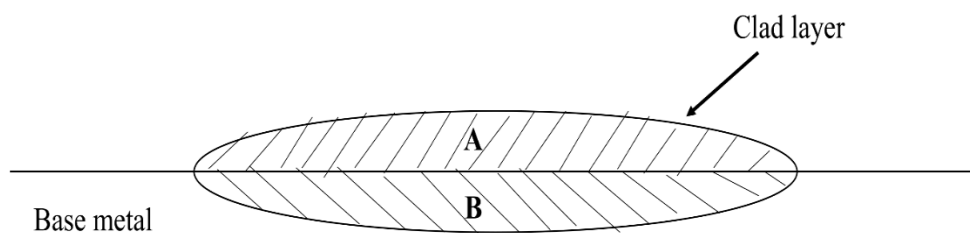
the fluid film forms between the surfaces reduce the coefficient of friction. The reduced coefficient friction can be as low as 0.01. In high-temperature working environments ( $>350$  °C), surface damage usually happens during a prolonged operation period. In such cases, solid lubricants are indispensable in developing a lubricant glaze layer, increasing efficiency and reducing material damage. Many researchers have used solid lubricants in coatings to enhance the tribological performance. The use of solid lubricants in the cladding can improve the tribological characteristics of composite coatings.

### **1.1 CLADDING AS A SURFACE ENGINEERING METHOD**

Cladding is defined as a surface melting process in which assisted process is used to fuse an alloy addition to the surface (Ion 2005). The machine parts used in the industry, such as rails, turbine blades, and conveyors, are usually subjected to abrasive wear. To minimize the cost of the operation, repairing the components would be a better choice than replacing the new parts. In such cases, hardface or clad layer deposition by welding or microwave can be done automatically or manually, depending on the operating and other circumstances. The type of material used on the surface depends on the type of wear to be protected against. Mainly, wear mechanisms can be divided into four for simplicity. In friction and adhesion, mainly metallic surfaces roll and contact each other. For example, cable and sheave, bearing and shaft usually contact each other. Due to the contact pressure, surface finish, and material structure, wear occurs. Likewise, abrasion wear occurs in the transport of minerals, dredging in the mining industry. The impact and shock usually occur in crushers and excavator buckets. In these applications, a higher percentage of manganese can be used in tungsten and chromium alloys, as it produces a hard surface with a ductile matrix interior. The tools which are exposed to cyclic thermal loads lead to fatigue failures. Also, cracks appear on the materials due to the oxidative environment. In this case, nickel and cobalt alloys are usually used for better abrasive wear, thermal fatigue, and corrosion resistance. The alloy is usually introduced during or before the operation as wire or powder. The object is to melt a thin layer of the substrate material with as much alloy addition possible. With the minimum amount of substrate melting, the nominal chemical composition of the alloy is produced, which

would further affect the mechanical properties. It is mainly used for non-ferrous metal and metal matrix development on the substrate for tribological applications. Generally, gas and turbine power plant machinery have shorter service life because they frequently fail due to surface phenomena like wear, corrosion, and oxidation. Selection of coating method must be made based on the application. No universal coating can be used for all conditions. The selection of coating method usually involves considering the operating conditions, material compatibility, substrate conditions, cost, safety, and environmental aspects. Heat sources like flame, arc, beam, and inductive heat are very effective for modification of surface to resist wear. Different cladding methods such as CO<sub>2</sub> welding, submerged arc welding, shielded metal arc welding, Laser welding, TIG (Tungsten inert gas) welding, MIG (Metal inert gas) welding, PTA (plasma transferred arc), and microwave cladding are developed based on their application, access, economic and material conditions, etc. In recent years, metals, ceramics, and intermetallics were used for the cladding of metallic materials. The negligible dilution of the cladding enhances surface protection, particularly for tribological applications. Also, cladding is cost-effective than many thermal spray techniques. Many industries such as turbines, power plants, material processing plants are very prone to wear, loss of mechanical properties due to their higher operating temperatures. Because of their flexibility of depositing thick layers, good tribological properties can be achieved. It is also testified that arc heating has a greater impact on chemical compositions in the clad layer affects their performance. Most of these processes usually melt the parent material, which leads to the metallurgical bonding between the parent material and the filler material. The melt depth, surface temperature, and heating and cooling rates of the sample are primarily important to the mechanical properties. The melting of the parent material in the process is the main advantage of the cladding process. However, the change of chemical composition of the clad layer occurs due to the dilution further effect. However, dilution should be as minimum as possible to attain better properties of the clad layer. The dilution not only depends on the selected cladding process but also depends on various parameters. In general, the amount of heat input per scanning time or running time of the external heat source changes the dilution levels. Also, the selection of the cladding technique depends on the following factors: property and

quality requirements, workpiece physical and metallurgical characteristics, and cost. As a quality requirement, mainly controlling the dilution is essential for better characteristics of the material. A minimum dilution is crucial for metallurgical bonding, but the extent of the dilution is further detrimental to the mechanical properties. However, higher dilution may be acceptable in some cases, where built-up layer formation is required. The schematic representation of dilution of cladding operation is shown in Fig. 1. The cladding of 2-3 layers leads to the thermal cracking and fracture of the component. Also, little mixing of the body material into the cladding is an important concern to avoid degradation of the parent material. To attain better properties and minimize dilution, the foundation layer with the low hard material must be added first on the surface before applying the required hard alloy layer.



$$\text{Dilution Percentage} = \frac{B}{A+B} \times 100$$

Figure 1. 1 Dilution of the clad.

Due to the rapid heat transfer into the substrate in the cladding operation, a metallurgical bond would be formed between the clad and the substrate. Due to the considerable difference of thermal gradient between the substrate and clad, cracks may happen. The creep magnitude formed in the HAZ further influences the residual stress state. The physical characteristics such as weight, size, and shape of the workpiece are also important due to their work zones involved in the processes. Similarly, metallurgical requirements are essential while working with various materials. For example, low hydrogen processes or electrodes are required while working with alloy steels to prevent hydrogen cracking. Some processes need

preheating and post-heating based on the process, base, and clad material. The coefficient of thermal expansion of the clad material is also important to know the thermal stresses involvement. Differences in the cladding and base material thermal expansion can generate thermal fatigue failures. Thermal stresses induced in the specimen can be expressed as follows

$$\sigma_T = E (\alpha_{clad} - \alpha_{substrate}) \Delta_T$$

Where  $\alpha$  is the coefficient of thermal expansion,  $\Delta_T$  is the temperature difference,  $E$  is the young's modulus, and  $\sigma_T$  is the thermal stress induced in the specimen. The elements like labor and materials are the critical factors for overall cost. The distortion and residual stress are involved due to the sudden rise and cool down of the deposit. The required preheat temperatures in the process usually depend on the material and process conditions. The preheating can further avoid cracking near the HAZ clad regions. Cladding competes with a large number of coating processes, particularly thermal spraying-related methods. The close inspection of the dilution and other process conditions in the process ensures a good quality microstructure. In comparison, the thickness of the coating can be produced with the methods such as laser, submerged arc welding, metal inert gas welding, tungsten inert gas welding, plasma spraying, flame spraying, high-velocity oxy-fuel process, plasma arc is 0.2-2.0, 2-10, 1-6, 0.5-3.0, 0.1-0.2, 0.8-2, 0.3-1.5 and 1-5 respectively. To summarize, developing sophisticated electronic systems for various cladding systems to enhance the quality control would increase the cladding applications despite the ever-growing coating processes in the marketplace. Previously many researchers, including Ion (2005) and Bao et al. (2006) studied the cladding mechanisms and reviewed by many researchers such as Vilar (1999) and Wu and Li (2006) (BAO et al. 2006; Ion 2005; Vilar 1999). By examining the required characteristics of the cladding, the attributes of the components and other conditions, and materials that favor the process on technical and economic grounds can be identified.

#### **Applications and future scope:**

The potential and current cladding applications can be used in diesel engine cylinder liner, turbine blades, pump shafts, camshafts, diesel engine valve seat inserts, die casting dies, gears, automotive steering assembly, turbine blades, Autogas engine

bore, etc. The machinery parts used in the paper-pulp and textile industry, such as cutter blades, grinders, rollers, and other moving mechanical assemblies, were beneficial due to the application of hard coatings. Also, the components used in the automotive industry against particle erosion and wear at higher temperatures, such as turbine blades and compressor blades, usually need both hard and soft coatings to extend their lifetime and retain accuracy.

Cladding surfaces direct competition from thermal spray and thin coating methods. However, cladding produces a diffused interface with the substrate. It is essential to generate an extensive database for cladding materials for corrosion and tribological applications at ambient and elevated temperatures. Process automation during cladding with different processes is another important area that is at a rapid pace. In the coming years, with advanced technology, surface absorptivity, temperature, and other conditions can be changed according to the material requirement. Despite the extensive research work, a broad scope is available to establish the limitations of existing potential methods to pave the way for further industrial applications in process technology and materials.

### **Sliding wear:**

When two surfaces in contact sliding movement, one or both of the surfaces will suffer wear. Wear is associated with the detachments of fragments of material from the asperities, and the volume of each other fragment will depend on the size of the asperity junction from which it originated. It is assumed that the volume of material removed by wear,  $\delta V$ , will be proportional to the cube of the contact dimension  $a$ , which implies that the shape of the wear particle should be independent of its size. The volume can be taken to be that of a hemisphere of radius  $a$ , giving

$$\delta V = 2\pi a^3/3 \quad (1)$$

Not all asperity contacts give rise to wear particles. Let us assume only  $k$  portion does so. The average volume of material  $\delta Q$  worn away per unit sliding distance due to sliding of the one pair of asperities through a distance  $2a$  is given by

$$\delta Q = k\delta V/2a = k\pi a^2/3 \quad (2)$$

And the overall wear rate  $Q$  arising from all the asperities contacts is sum of the contributions over whole real area of contact:

$$Q = \Sigma \delta Q = k/3 \Sigma \Pi a^2 \quad (3)$$

The total normal load is given by

$$W = \Sigma \delta W = P \Sigma \Pi a^2 \quad (4)$$

And hence

$$Q = kW/3P \quad (5)$$

It is convenient to combine factor of  $1/3$  into the account of proportionality. By putting  $K = k/3$  and assume that  $P = H$ , the indentation hardness. We can rewrite the equation in the form:

$$Q = \frac{KW}{H} \quad (6)$$

The above equation, relating the volume worn per unit sliding distance,  $Q$ , to the microscopic quantities  $W$ , normal load, and  $H$  is the hardness of the softer surface, is often called the Archard wear equation. The dimensional wear coefficient  $K$  is of fundamental importance, and provides a valuable means of comparing the severity of wear processes in different systems.

### 1.1.1 TIG Cladding

Tungsten inert gas welding (TIG) is a well-recognized process mainly used for industrial manufacturing applications. It is an arc-assisted surface engineering process. The arc generates at the tungsten electrode tip fuse the base metal with or without filler material. Filler material can be in the form of wire or powder. Usually, molten material is protected by helium or argon to prevent oxidation. The selection of shielding gas level is also an important aspect as it impacts the hardness of the clad material. The Increase of shielding gas level decreases the hardness of clad. In TIG cladding, three different techniques can be used to deposit a clad layer: powder blown method, wire feed method, and powder preplacement method. Among those, the powder preplacement method is a flexible and easy to operate method. Literature suggests that optimum process parameters are required for a better quality of the clad

layer. Current and scan speed are more significant parameters in the TIG process. Exotic alloys can also be joined with TIG welding due to their exceptional stability. Also, it gives excellent microstructural refinement in a single pass. TIG surfacing method can acquire good wear resistance and hardness by changing the microstructure of a material. Tadayuki suggested a shielding arrangement while working with titanium alloys. Secondary shielding is required to protect the weld pool from oxidation. Bottom purging can also be used while working with thin sheets less than 2mm. The TIG process is very much helpful while working for complex clad shapes where space constraints are essential. Internal cladding of nuclear reactor pipes is an example where space is a constraint. Also, there is no other alternative to deposit complex clad shapes with higher-end automation. Deposition of buffer layers can be done by TIG cladding technique, which can be useful for different base materials to weld together. The repair of work pieces also can be done with this method to enhance the service life. Usually, components expose to certain stress patterns due to impact stress, thermal shocks, wear, and other environmental conditions. Fig. 2 represents schematic of the TIG cladding process. The composite powder is usually mixed with a lubricant like PVA or organic binder to make a paste-like substance. Then the metallic mask of desired thickness is used to create a layer on the substrate before the TIG torch melting. The added lubricants will evaporate at room temperature. During the melting of the alloy powder, steep temperature gradients form between the molten pool center and the leading edge of the pool. The gradients in the surface tension of the molten pool further drive the fluid flow (Marangoni) and further stirs the fluid flow leads to the homogenization of the clad. The dilution is also an important issue. The minimum melting of substrate material while having a strong metallurgical bond is a difficult task. Dilution impacts the chemical composition of the clad, which can change the mechanical properties. So, the optimization of TIG process parameters is crucial to acquire good quality clads. The advancement of power supply devices of cladding systems is also an important factor for arc-assisted surface engineering devices. Earlier, electromagnetic amplifiers were used to supply the welding current. Thyristors are also used for processes where higher currents are required. Later, pulsed current control was dominated many power systems due to their better control over porosity, spatter, and deep penetration in the GTAW process.



With the TIG welding source, the welding speed can be easier during deposition of optimum layer height for better grain refinement and tempering. Also, minimum passes are enough to deposit the clad with better microstructural refinement. The tampering effects of pulsing in operation minimize the preheat requirement while working the materials such as hardened steel. Marine engine diesel valves, process control valves can be cladded with the TIG cladding technique. Also, superheater tubes in coal-fired power plants and incinerators, exhaust valves, casting rollers, blast furnace bells, forging die block, and ball mill shell interior can be cladded to extend the life. The hard facing alloys such as nickel-based, cobalt-based, iron-based can be used to engineer the surfaces based on the application.

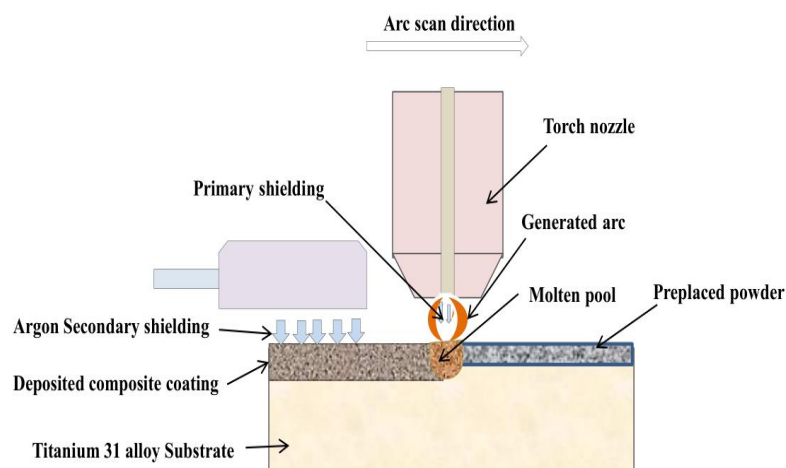


Figure 1. 2 Schematic of TIG Cladding

### 1.1.2 Microwave Cladding

Interest in consuming microwave energy to fuse metal powders started in the 1990s. Conventional furnaces like cupola furnace, blast furnace consumes a lot of energy compared to microwave energy for melting materials. Also, microwave energy is effective in less time and is better in terms of safety. Also, it is cost-effective than many other cladding techniques. Conventional heating causes poor microstructure due to its higher thermal gradient. In microwave heating, molecular level heating causes

finer microstructure without porosity and thermal cracks. However, the microwave absorption coefficient of many metals is very low at room temperature. Due to the thermal instability of metallic powders, melting of metallic materials with microwave energy becomes a problematic task at room temperature. To overcome this issue, a microwave hybrid heating (MHH) mechanism is developed. Usually, in MHH, a susceptor (microwave absorbing material) transfers heat to metal powders by conduction until their threshold temperature. After reaching the threshold temperature, powders will start absorbing the microwave energy. Mainly, charcoal powder is used as a susceptor material, and a thin graphite sheet separator is used to prevent contamination of molten pool. To hold the temperatures for a more extended period of time, microwave transparent materials (Alumina, glass wool, etc.) will be used. In recent years, microwave hybrid heating has emerged as a rapid processing technique. Also, this technique is used for cladding of materials to resist engineering failures like wear and corrosion in gas and turbine power plants. In Figure 1.3, microwave cladding is presented in a schematic representation.

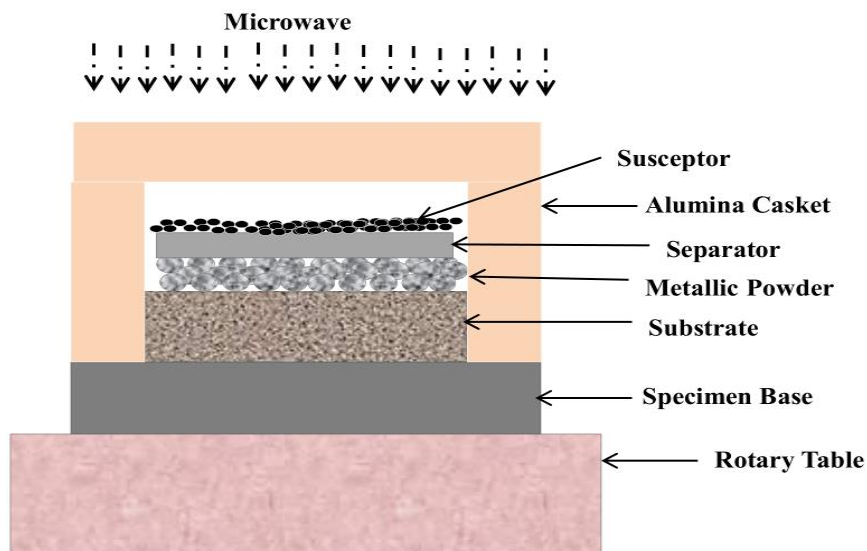


Figure 1. 3 Schematic representation of Microwave Cladding.

The microwave melting can be used for sintering, casting, cladding, and joining, etc. (Kumar et al. 2020; M S et al. 2011a; Singh and Zafar 2019; TAKAYAMA et al. 2008; Zafar and Sharma 2015). Despite the competitive welding techniques and thermal spray coatings, microwave heating remains indispensable in several

applications due to the possibility of obtaining better quality products, rapid processing time, and providing excellent microstructure. Also, it is noted that microwave heating decreases 3-5 times CO<sub>2</sub> emission than conventional heating. Compared with traditional heating methods, the microwave heating method reduces the energy consumption by 60-80 %, which is attributed to the interaction of electric and magnetic fields that result in heating with dielectric loss, joule loss, and magnetic loss.

In comparison with the conventional methods, microwave processing is characterized by:

- Digital monitoring and control of system process parameters and material processing is possible
- As the process is non-contact type materials processing, no thermal distortion and thermal defects would occur.
- Melting of materials would occur due to the propagation of electromagnetic waves
- Due to the molecular level, heating occurred from inward-outward rather than outward-inward, processed parts show good microstructure.
- A minimum shielding medium is needed while working with highly reactive materials like titanium, niobium, molybdenum, etc.
- Reproducibility,
- Joining or cladding of dissimilar metals that other conventional fabricating methods cannot join.

The efficiency of the microwave process mainly depends on the physical and chemical properties of the material and system parameters. Due to its microwave energy capability, manufacturing processes like brazing, cladding, sintering, and microwave-assisted machining can be done, which has recently drawn significant attention in industry and academia.

## **1.2 Cladding materials**

Selecting materials which are having low cost and good wear properties is a challenging task. Metallic powder composed by a ductile metal matrix with hard ceramic reinforcement known to be very effective for wear applications. Nickel-based alloy powders are known for their efficient bond strength and excellent wear

resistance. The reinforcement phases like whiskers, monofilaments, fibers, etc., have been efficient in increasing MMC wear performance. Among those reinforcement particles, tungsten carbide is an extremely hard material with excellent corrosion and wear properties which are widely used in cutting tools, drills, and corrosion-resistant coatings. Selecting coating materials for a particular surface engineering process is also a crucial problem. Here several factors play an important role, namely service conditions, application choice, and coating compatibility with the substrate. The selection of cladding materials can be taken by factors such as wear resistance, cost, base material, deposition process, thermal properties, impact, corrosion, and oxidation resistance. Generally, wear resistance increases with the carbide content, but their inclusion reduces the impact resistance. There are five different hard-facing materials: built-up alloys, metal-to-metal wear alloys, metals-to-earth abrasion alloys, tungsten carbide, and non-ferrous alloys. However, metallurgical characteristics of the material also need to be considered. The most popular cladding alloys for layer fabrication are nickel, iron, and cobalt. The substrates made of carbon-manganese alloy, stainless steel, tool steels, and other alloys such as aluminum, nickel, iron, and magnesium can be used for cladding applications.

### **1.2.1 Nickel based alloys**

Nickel-based alloys are used in hardfacing processes due to their abundance availability and superior characteristics for tribological applications. Nickel is a versatile element and will alloy many metals. The face-centered cubic structure of the nickel matrix ( $\gamma$ ) can be strengthened by precipitation hardening, carbide precipitation, solid-solution strengthening, etc. The nickel alloys are widely used to design the components to overcome wear and corrosion-related problems. The most available nickel alloys are boride containing alloys, carbide containing alloys, and laves phase containing alloys. At first, boride-containing alloys were available as powder form but are now obtainable as tubular wires. The silicon content in the alloy has a significant influence on wear resistance. Also, the hard boride content present in the coating influences the abrasion resistance. The carbide-containing nickel alloys were developed as similar to cobalt-based alloys to resist abrasion, galling, corrosion, etc. The large fraction of chromium carbides in the clad volume makes the alloy prone

to cracking after deposition. In the laves phase alloys, NiMoSi or Ni<sub>3</sub>Mo<sub>2</sub>Si or both present to provide oxidation and corrosion resistance. Usually, the laves phase constitutes are approximately 50 vol.% (Mason and Rawlings 1994). The wear resistance depends on the volume fraction of the laves phase on the volume fraction (Mason and Rawlings 1989). Among nickel alloys, NiCrSiB alloy has wide applications in bearings, engine valves, shafts, dies, molds, stem guides etc. Titanium, tungsten, and chromium carbides can be added to the nickel and cobalt alloy in various proportions to enhance abrasion and erosion performances, particularly at elevated temperatures. However, higher proportions of carbide additions in these alloys increase the chance of thermal fatigue cracks. Nickel matrix dispersed with tungsten carbide can provide better wear resistance to abrasive wear. The carbide particles in the coating act as a wear-resistant barrier to abrasives (Berns 2003). It is also noted that abrasive wear increased with the degree of dissolution of carbide content. This degradation of primary carbide and other process parameters used in the process also affects the mechanical and wear properties.

### **1.2.2 Solid lubricants**

Liquid lubricants such as oil, animal fats, and grease are ineffective at higher temperatures due to their lower saturation points. Many researchers have been used solid lubricants as coating materials and added them to the metal matrix. It is reported that the coatings proved to be efficient at higher temperatures. Transition metal dichalcogenides such as MoS<sub>2</sub>, WS<sub>2</sub>, BaF<sub>2</sub> have been widely used. Also, soft metals such as Ag, Cu, and lead show good lubricant properties below 400°C, and hexagonal boron nitride type materials can withstand up to 900 degrees due to their lamellar structure. Halides sulfates of rare earth metals also withstand up to 500°C. Despite many advantages like high temperature and load stability, these materials increase frictional coefficient and cannot provide cooling effects like liquid lubricants. So, the appropriate amount of lubricant phase in the metal matrix is always beneficial while working at higher temperatures. Solid lubricants include soft metals (such as Ag, Pb, and Cu), transition metal dichalcogenides (TMD) (WS<sub>2</sub>, MoS<sub>2</sub>, TiS<sub>2</sub>, BaF<sub>2</sub>, and TaS<sub>2</sub>), metal oxides (NiO, MoO<sub>3</sub>, and CuO), and alkaline halides (BaF<sub>2</sub>, CeF<sub>2</sub>, and CaF<sub>2</sub>) (Aouadi et al. 2008; Babuska et al. n.d.; Cura et al. 2015; Gustavsson and Jacobson

2016; Jin et al. 2016; Li et al. 2016; Quan et al. 2016). The TMD monolayers ( $\text{MoS}_2$ ,  $\text{BaF}_2$ ) have no inversion center, allowing charge carriers to attain a new degree of freedom. Usually, mixing TMDs with other 2D materials like graphene and hexagonal boron nitride (hBN) would be better to develop vander Waals heterostructures. However, using a single solid lubricant cannot provide adequate lubrication over a broad temperature range. Solid lubricants have many advantages such as high temperature and pressure stability, lubricity at high vacuum environments, longer shell life. Presently, solid lubricants used in industrial applications solve friction and machine tool problems in forming mold, bearing, and seal (Blanchet et al. 2002; Liu et al. 2018; Wang 2004). Although considerable progress has been made in developing and investigating the lubricating mechanism concerning temperatures, high-temperature tribology still lacks the fundamental theory. More investigation should be focused on the synergistic lubrication effect of the novel solid lubricants for better lubricity at a wide temperature range for a long-life duration.

## CHAPTER 2

### LITERATURE REVIEW

The application of alloys has been expanded from medical, automobile, chemical, aerospace, robotics, construction, owing to their excellent chemical and physical properties, less weight, wear, corrosion resistance and other specific characteristics. With the increasing growth of industries and large-scale development of metal sources, the applications of alloys have matured faster than other structural materials. Engineering alloys are usually comprised of one or more metallic (e.g. Ni, Cr, Fe, Al, Ti, and Mg) or non-metallic elements (e.g. N, C, O, and H). According to the statistical results, composite material systems with added ceramic powders have become commonly used for coating of engineering alloys. Based on various properties like low density, specific strength, temperature resistance, wear and corrosion resistance alloys will be chosen for specific applications (Bandyopadhyay et al. 2020; Fashu et al. 2020). Recently, an enormous amount of research has been done on the surface modification techniques, novel engineering alloys, optimization of parameters in various surface engineering techniques to improve service life of the components.

#### 2.1 Nickel-based alloys

Remarkable achievements have been made in the preparation of various metallic coatings. Nickel alloys have many advantages like wear, corrosion resistance and hardness etc. over other materials. Self-fluxing alloys are the first choice for cladding techniques. Mainly, Nickel, cobalt, iron-based coatings present good adaptability for titanium, aluminium, and magnesium alloys substrates with exceptional properties (Liu et al. 2021b). Ramesh et al. revealed that nickel-based alloy coatings have better bonding strength and excellent abrasive and adhesive wear resistance. These coatings have many engineering applications due to their superior thermal stability and mechanical properties (Ramesh et al. 2010). Recently many researchers nickel-based coatings were applied on different engineering parts such as turbine blades, plungers, extruders, cutting tools, and wearing plates etc. The coating techniques such as

thermal spraying, electrodeposition, electroplating, electrophoretic deposition, cold spraying, physical vapor deposition, chemical vapor deposition etc. were used nickel-based coatings for improve surface properties.

Similarly, Leunda et al. also studied the tungsten carbide reinforced NiCr claddings by laser cladding technique. To attain homogenous coating, parameters such as power and feed rate was optimized. The low dilution of 5-10 % is always essential to avoid clustering of the carbide particles used in the study. Due to the higher density WC particles than the nickel alloy, more carbide content was deposited near the interface. Due to the formation of carbide rich region, higher mechanical properties were achieved (Leunda et al. 2016). Weng et al. studied the effect of WC content in improving wear resistance at elevated temperatures. The higher WC particle content in the coating enhanced the microhardness due to the reduction in the formation of the dendritic size of the nickel alloy. At both room and higher test temperatures, wear performance increases gradually as increasing the WC content (Weng et al. 2016). Ming et al. developed deposited nickel alloys such as colmonoy 6, colmonoy 88, and AI-1236 on stainless steel using laser cladding technique. From results it was observed that colmonoy 6 has more  $\gamma$ -nickel dendrites, nickel borides, and nickel silicides. Similarly, colmonoy 88 consists of matrix carbides than the AI-1236. However, due to the higher quantity of mixed carbides and tungsten carbides in the clad, wear resistance of the AI-1236 was enhanced than the other nickel alloys (Ming et al. 1998). Conde et al. studied the Ni-Cr-Si-B alloy with the low Cr-B-Si alloy on carbon steel by laser cladding and. It was observed that Ni-Cr-Si-B alloy having low Cr-B-Si consists of  $\gamma$ -Ni and was found to be more complex. There were more intermetallics formed with boron, chromium and nickel. Similarly, the Ni-Cr-Si-B alloy with high Cr-B-Si alloy consists of Ni solid solution and other intermetallic like  $\text{Ni}_3\text{Si}$  (Conde et al. 2002). In another study, it was found that rolling contact behaviour of the NiCrSiB/WC-Ni coating is better than the NiCrSiB coating. Hardness of the coating also increased due to the WC addition, which further reduce wear rate and coefficient of friction (Xiang et al. 2014). Also, application of nickel-based coatings is important in thermal barrier coatings to prevent component from high temperature and corrosive atmosphere. Nickel based coatings have remarkable applications in jet engine and powder plant components. The repair of the components



such as turbine blades, engine cylinders nickel alloy claddings can be useful to achieve longer life (Wang et al. 2017a). Various nickel-based alloys such as Inconel 718, Inconel 100, Ni-Al, NiCrAl, Tribaloy 66, Tribaloy T-800 were deposited earlier to enhance the surface properties of the various substrate material (Abboud et al. 1995; Dehm 2002; Singh and Mazumder 1987).

By adding the tough ceramic particles like SiC, WC, TiC, La<sub>2</sub>O<sub>3</sub>, and Cr<sub>2</sub>C<sub>3</sub> to the nickel and cobalt based alloys, wear resistance of composites would be increased significantly. The WC reinforcement in the nickel alloy matrix differs from NbC, TiC and B<sub>4</sub>C etc. The tungsten carbides usually will not form in situ during solidification and, which must survive welding cycle. However, the heat sensitivity of the WC eliminates higher productivity processes involving higher melts, from being used. The nickel tungsten consumables are typically available with a NiCrSiB or NiBSi matrix. The phases in the matrix are usually comprised of soft primary nickel dendrites, hard borides, silicides, and carbides (Cockeram 2002). The interdendritic phases present in the alloy increases the hardness of the matrix. Addition of boride in the matrix decrease the melting temperature of the alloy, thereby enhance the solidification temperature range. The challenges in fabrication of materials determine the type of process used. Ni-WC alloys require that the carbides are introduced as a secondary phase in the melt. The dissolution of carbides is the main challenge in Ni-WC alloy system (Mendez et al. 2014). Luo et al. studied the cracking susceptibility by adding different percentages of NiCrSiB content in the NiCrSiB-Ni/WC laser clad. It was found that the appropriate percentage of NiCrSiB/WC reduced the thermal defects. The optimum addition of 21 % Ni, 30 % WC-NiCrSiB clad was favourable to the improvement in wear resistance of the coating. The solid lubricants can be used to reduce thermal distortion defects while operating at high temperatures (Luo et al. 2015). Farahmand et al. fabricated the nickel-tungsten carbide composite coatings using a diode laser with induction heating. The results showed that the deposited clads attained good porous free and mechanical properties (Farahmand et al. 2014). Niranatlumpong et al. developed the nickel alloy coatings such as NiCrSiB/WC and NiSiB-WC using electric arc method and found that microstructure of the NiCrSiB/WC coating consists mainly of WC/W<sub>2</sub>C phase with the other phases like NiCr and NiCrW solid solutions. Similarly, NiBSi coating mainly consists of Ni and

NiW solid solutions. Usually, chromium is useful for formation of hard phases. Due to the absence of chromium in the NiBSi coating, hardness was reduced. However, due to the detachment of tungsten carbide particles in the NiCrSiB/WC coating, more wear rate was observed than the NiBSi coating (Niranatlumpong and Koiprasert 2011). The tribological properties of the Ni-WC composite coatings were evaluated by Surrender et al. and observed that addition of WC in Ni increases the microhardness. Also, addition of WC cause reduction of coefficient of friction of 0.34, when compared to pure nickel coating (0.62) and steel substrate (0.54) (Surrender et al. 2004). However, failure of the WC added coating usually happens due to crack formation, which is due to the WC/W<sub>2</sub>C separation in the coating. In addition, WC carburize and forms W<sub>2</sub>C phases, which further lower the mechanical properties (Farayibi et al. 2011; Sliney et al. 1994). From the extensive literature, NiCrSiB alloys have better microstructural and mechanical properties due to the formation of high-volume fraction of boride and carbide phases as these alloys have more quantity of chromium, carbon and boron.

## **2.2 Self-lubricating coatings**

The inclusion of Solid lubricants in the coating material can be the viable alternative to reduce the friction coefficient and enhance the tribological performance, especially at higher operating temperatures (above 350 °C) (Allam 1991; Bello et al. 2016; Peterson et al. 1959). Liquid lubricants rapidly degrade at above 350°C. Many industries include aerospace (gears, bearings, satellite components), tooling, diesel engines, which operate at higher operating temperatures (Aouadi et al. 2009). Solid lubricants can withstand extreme conditions like a heavy load, higher speed, and temperature without any surface deterioration (Zhu et al. 2019).

Torres et al. studied the performance of self-lubricating laser coatings at elevated temperatures and compared the results with those observed for the reference nickel alloy coatings. The results revealed that the composite coating containing lower and higher temperature solid lubricants (Ag and WS<sub>2</sub>) effectively lowered the friction and wear at high temperatures (Torres et al. 2020). Sahoo et al. revealed that the percentage of CaF<sub>2</sub> present in the composite TiC-Ni coating affected the value of the coefficient of friction value. As the CaF<sub>2</sub> percentage was increased from 5% to 20%,

the coefficient of friction (COF) value decreased from 0.7 to 0.4 (Sahoo and Masanta 2017). Huang et al. studied the effect of solid lubricant content on the properties of the NiCr/Cr<sub>3</sub>C<sub>2</sub> coating. The results revealed that a eutectic content of less than 10% for BaF<sub>2</sub>.CaF<sub>2</sub> yielded better tribological performance. It also revealed that the microhardness and tensile strength decreased as the solid lubricant percentage in the coating increased beyond 10% (Huang et al. 2009). Doddamani et al. studied the tribological performance of the composite coating composed of a mixture of CaF<sub>2</sub> and CaSO<sub>4</sub>. The results showed an improvement in wear resistance. The reduction in the coefficient of friction was attributed to the lubrication effect exhibited by the coatings (Doddamani et al. 2018). Likewise, hexagonal boron nitride (hBN) exhibited good lubrication properties up to 900 °C because of its graphite-like structure (Kimura et al. 1999; Lipp et al. 1989). Lu et al. reported that an hBN content of 10% in the nickel-based coating showed outstanding performance at 600 °C (Lu et al. 2016). Xiaoliang et al. developed Ni<sub>3</sub>Al self-lubricating composites with different proportions of solid lubricants such as Ag, hBN, and WS<sub>2</sub> by spark plasma sintering technique. The solid lubricant percentage of 15% in the composites was effective for reducing the coefficient of friction and wear rates at room temperature to 800 °C. The solid lubricant encapsulation in the composites has widened the operating temperature range. The solid lubricants such as Ag and WS<sub>2</sub> were acted effectively at lower temperatures, and hBN was provided adequate lubricity at higher temperatures (Shi et al. 2014). Ding et al. fabricated nickel-based alloy coating with the Ag and BaF<sub>2</sub>/CaF<sub>2</sub> solid lubricants and observed that the solid lubricant phases in the composites were beneficial to enhance the crack resistance and tensile strength (Ding et al. 2008). The crystal structure of hBN is very similar to graphite and exhibits excellent lubricity. However, hBN can be very effective at a higher temperature than graphite due to their strong Vander Waals forces (Tyagi et al. 2011). Similarly, MoS<sub>2</sub> forms an effective glaze layer at lower temperatures ( $\leq 400$  °C) because of their lamellar structure (like graphite and Ag), which can act as an effective lubricant at lower temperatures (Aouadi et al. 2008; Gulbiński and Suszko 2006). Wang et al. developed the laser cladded self-lubricating wear-resistant ceramic composite coatings by encapsulating CaF<sub>2</sub> solid lubricant in the Al<sub>2</sub>O<sub>3</sub> ceramic matrix. Compared with the Al<sub>2</sub>O<sub>3</sub> coatings, Al<sub>2</sub>O<sub>3</sub>/CaF<sub>2</sub> coating showed superior wear resistance and a lower friction coefficient

(Weng et al. 2016). Qu et al. studied the microstructure and wear behavior of the laser clad coatings by changing MoS<sub>2</sub> content in the coating. The coatings produced with 6 % MoS<sub>2</sub> content enhanced the wear resistance. The increase of MoS<sub>2</sub> content in the coating leads to a detrimental effect on mechanical properties (Qu et al. 2019). Gao et al. developed a self-lubrication composite coating by adding the TiS/WS<sub>2</sub> in the TiN reinforced matrix. The results indicate that the wear rate and friction rates were significantly reduced. Besides, the 20 % WS<sub>2</sub> encapsulated Ni-TiN coating showed good anti-wearing and friction-reducing effects (Gao et al. 2019). Wang et al. fabricated NiCr+Cr<sub>23</sub>C<sub>6</sub>+Ag+BaF<sub>2</sub>/CaF<sub>2</sub> composite coating using a laser cladding technique on a stainless-steel substrate. The addition of Ag and BaF<sub>2</sub>/CaF<sub>2</sub> solid lubricants reduced material loss at a wide range of temperatures. The optimum amount of solid lubricant content in the coating further reduces the microhardness (Wang et al. 2012). Liu et al. fabricated Co-Ni/WS<sub>2</sub> composite coating by pulse electrodeposition process. The addition of WS<sub>2</sub> enhance the microhardness due to the change of orientation. Also, the WS<sub>2</sub> powders further reduced the fluctuation of friction curve at higher temperatures. Due to the embedded WS<sub>2</sub> in the coating, crevices, gaps, and micro holes were filled, which further effectively prevented the corrosion medium to reach the substrate, endowing Co-Ni/WS<sub>2</sub> coating with excellent corrosion resistance (Liu et al. 2020). MoS<sub>2</sub> solid lubricant plays very important role in space filed application owing to their excellent properties in space environment such as superior thermal stability radiation and adhesive wear resistance. However, pure MoS<sub>2</sub> additives in the coating increases the friction coefficient due to its instability against oxides. To enhance the performance of the MoS<sub>2</sub> film, additives such as metallic (Pb, Au, Ti, Ag) and non-metallic (graphene, graphitic carbon nitride, etc.) can be mixed to improve the multi-layer composite films for better performance (Savan et al. 2000). Similarly, Zhang et al. used magnetron sputtering to obtain MoS<sub>2</sub>/Pb nano composite coating on stainless steel. The Pb additives in the MoS<sub>2</sub> coating improved the wear performance and oxidation resistance. The obtain properties can improve the reliability and life of the space components (Wang et al. 2017c). Zhu et al. prepared nickel based self-lubricating NiCrAlY/Ag<sub>2</sub>O/Ta<sub>2</sub>O<sub>5</sub> coating on Inconel alloy and studied the tribological performance at elevated temperatures. Ag contributed lubrication at room temperature, but ineffective at

temperatures higher than 550 °C. The other phases formed on the operation like NiO and CrO<sub>2</sub> were provided adequate lubrication at higher temperatures. At 750 °C, phases such as AgTaO<sub>3</sub> and Ag<sub>2</sub>Ta<sub>4</sub>O<sub>11</sub> were worked together with the TaO<sub>2</sub>, CrO<sub>2</sub> and NiO to provide adequate lubrication for a wide temperature range. In another study, Xiang et al. cladded TC4 alloy with  $\gamma$ -NiCrAlTi/TiC/CaF<sub>2</sub> coating by laser cladding technique. Further, high temperature tribological performances of the coatings were studied. It was learned that CaF<sub>2</sub> encapsulation leads to the splashing, poor interface compatibility, and gasification because of their low density. To overcome this limitation, various lubricant additives were added such as WS<sub>2</sub> and MoS<sub>2</sub>. Consequently, lubricating phases formed between the friction pair were improved friction properties. During the wear test, the plastic deformation of the subsurface of the worn sample squeezed out the lubricant layer to the worn surface. The nanoscale solid lubricants not only provide better lubricating mechanism but also act as reinforcement particles in the matrix. From the extensive literature, it was clear that solid lubrication in the coatings or composites are essential for achieving high performance, efficiency, and durability at elevated temperatures.

### **2.3 TIG cladding**

The selection of cladding technique and coating materials usually taken based on the desired surface properties, quality and their performance. Among other techniques, TIG cladding is an economical process which can reduce overall cost of the operation. It also reduces porosity in the clad layer and enhances the metallurgical bonding of clad with the substrate. The selection of clad alloys will be chosen based on their compatibility with substrate material, cost, dilution and other service conditions. Various studies have been focused on TIG process parameter optimization, microstructure, and mechanical properties. Idriss et al. modified steel surface with TiC particles by TIG technique. The resolidified melt zones occurred at room temperatures are very resistant to wear. At higher temperature (600 °), formed oxide layer increase the contact uniformity and reduces the friction coefficient (Md Idriss et al. 2017). The optimum amount of TiC content on the surface reduced the wear loss. Also, friction coefficient stabilized at 0.2 and remains constant until 500 m.

Sabzi et al. developed nickel tungsten carbide composite coatings on plain carbon steel by TIG cladding technique and observed that as increasing the tungsten carbide particles in the coating, wear resistance increased gradually (Sabzi et al. 2018b). Ulutan et al. showed that the dilution control of the coating and dissolution of reinforcement plays a vital role in forming hard phases in the coating layer (Ulutan et al. 2011). Das et al. reported that the larger dilution requires higher fusion temperatures, the cooling rate influences the microstructures and hardness of the clad layer (Das et al. 2007). Aytakin and Akcin revealed that the composite TIG claddings developed with reinforcement particles in the nickel alloy matrix showed high hardness and corresponding wear resistance (Aytakin and Akçin 2013). Zhang et al. iron based self-fluxing coating on the carbon steel and optimized the process parameters like current, scan speed, and arc height to achieve better microstructural and mechanical properties. It was observed that coating composed of fine equal axial grains at the top and coarse cellular grains at the bottom. At optimum parameters (180 A current, 90 mm/min scan speed, and 6 mm arc height), wear rate of the clad was increased 4 times than that of the carbon steel substrate. From this study, it was observed that optimizing the process parameters to decrease dilution levels is very important for achieving better cladding characteristics in the convectional arc welding based processes (Zhang et al. 2017). Similarly, Buytoz et al. applied TIG cladding techniques for fabricating the tungsten carbide powder on the steel substrate. The study proved that optimum parameters used the fabrication can alter the microstructure (Buytoz et al. 2005). In another study, abbas eghlimi et al. deposited on the super duplex steel and found that slower cooling rate of the constant current of the cladding led to the formation of austenite content reformation and higher corrosion resistance (Eghlimi et al. 2014). The surface of the duplex steel modified by lailatul et al. with SiC material using TIG cladding technique. The TIG current of 80 A, 90 A, 100 A and energy input of 648, 768, and 1440 J/mm were taken as process variables. It was noted that resolidified clad layer was 3.3 times harder than the substrate material. The dendritic formation due to the complete melting of SiC was beneficial to get the higher hardness clads. Even though number of methods are available in the industry, TIG cladding is considered as one of the important methods for development of claddings since it is flexible, cost effective, and simple. It was

extensively used in military applications in second world war on various air craft components made with aluminium, magnesium, and stainless steel.

#### **2.4 Microwave cladding**

In microwave heating, molecular level interaction happens, and it usually depends on two factors like power absorption and microwave depth penetration. The skin depth and dielectric loss factor of the material are important factors while melting bulk metallic materials. As the skin depth and dielectric loss factor of metallic materials is low, the increase of surface temperature influences the permeability and conductivity of the material. Microwave energy emerged as a potential technology owing to its commercial and scientific advantages. Also, it primarily reduces material and energy consumption where environmental regulations are satisfied. Several studies focused on bulk metallic materials for cladding (M S et al. 2011b; Phanendra Kumar et al. 2020; Singh and Zafar 2020; Zafar and Sharma 2015), joining (Cho and Lee 2008; TAKAYAMA et al. 2008), and casting (Mishra and Sharma 2017b) using microwave energy. Several studies have been conducted on the melting of metallic materials using microwave irradiation, including magnesium, aluminium, molybdenum, nickel, 316L stainless steel, 434L stainless steel, iron, chromium, cobalt, W-18Cu, W-7Ni-3Cu, WC-6Co, WC10Co2Ni, Ni-B<sub>4</sub>C, and WC-12Co (Chhillar et al. 2008; Mondal et al. 2009; Panda et al. 2006; Saitou 2006).

In recent years, many investigations have been carried out on spatial distribution microwave processing of materials (Ohlsson 1989). Many researchers have studied theoretical studies based on the thermal transport of microwave phenomena. The heating rate and degree of uniformity are significant features in the process. Also, the developed microwave clads showed no signs of thermal distortion, porosity, and solidification cracks due to the volumetric heating. Gupta et al. developed WC10Co2Ni cladding through microwave hybrid heating. It was observed that the developed clads were metallurgically bonded with the stainless-steel substrate due to the partial dilution of a thin layer of the substrate. It was evident that the processed clads had no cracks, porosity, and solidification cracks. Due to the uniform distribution of hard phases in the clad, microhardness values of the clad ( $1064 \pm 99$  Hv) have minimal deviation throughout the clad depth. Also, the developed clad was

shown very high resistance to sliding wear (Gupta and Sharma 2011b). Similarly, Nair et al. developed high entropy alloy microwave treated claddings by varying Al fraction ( $\text{Al}_x\text{CoCrFeNi}$ ) ( $x = 0.1$  to 3). The clad was mainly composed of cellular structure and intermetallic phases, which were segregated and formed in the intercellular region. The interface was observed to be free of cracks and minimum porosity ( $< 1\%$ ). The intercellular regions of equimolar and three molar Al were mainly composed of B2 and A2 phases. The average hardness of the clads was two to three folds higher than the steel substrate. The results noted that the microwave synthesized high entropy claddings showed superior tribological properties for equimolar composition (Nair et al. 2019). In another study, nickel-based clad layer composed of EWAC + 20 % Cr23C6 was developed by microwave hybrid heating and reported that the clads had good microstructural and mechanical characteristics. The produced clads were free of porosity and other thermal defects. It was reported that the change of microstructure by cladding micro and nanostructured WC-12 Co materials. The clad produced with micrometric materials showed skeleton-type carbides in the metallic matrix. In comparison, nanostructured clad showed a uniform distribution of hard phases. A significant increase in hardness was observed with the decrease of particle size. The microhardness values of micrometric and nanometric clad were observed to be  $1564 \pm 50$  HV and  $1138 \pm 90$  HV. Due to the higher volume fraction of hard phases, nanometric clad showed superior wear resistance. Compared to the micrometric clad, the nanometric clad exhibited 54 % higher wear resistance. The grain pull-out was noted in the micrometric clad due to the non-uniform distribution of carbides. However, the nanometric clad showed no three-body abrasion due to the excellent distribution of nano carbides in the matrix (Zafar and Sharma 2015). Likewise, synthesized Ni-SiC composite claddings were developed using microwave irradiation. Different cladding systems were developed by varying weight fractions and particle size. The microstructure of the claddings was mainly composed of a columnar structure with the formation of precipitated intermetallic compounds. The developed clads were free of porosity and metallurgically bonded with the substrate. Among all material systems, Ni-10 wt. %SiC showed superior cavitation erosion resistance, which was about 7-8 times higher than the stainless-steel substrate. The Ni-SiC bimodal materials showed the highest microhardness and fracture



toughness. In microwave clad components, the splat boundaries and better adhesion were two significant effects that lead to resistance against cavitation erosion. It was observed that the microwave synthesized Ni-SiC material systems were outperformed the thermal spray coatings (Babu et al. 2019). In another study, Ni + 20 % Cr<sub>7</sub>C<sub>3</sub> composite clads were developed on the CA6NM turbine steel using microwave hybrid heating technique. The microstructural characteristics of the cladding material were studied by varying exposure times of 15 min, 25 min, 35 min, and 45 min. The clad processed at 35 min showed rod-like carbide structures. At 45 min exposure time, the microstructure of the clad was improved and showed fine dendritic type carbide structures. From the results, the weight loss of the components clad at 35 minutes and 45 minutes was reduced significantly by 29 % and 45 % than turbine steel substrate. The improved erosion resistance of the sample 4 attributed to the uniform distribution of dendritic phases. It was observed that the nano hardness of samples 3 and 4 was increased to two times that of sample 2. As indicated by XRD analysis, sample 2 was mainly constituted with Ni. In sample 3, hard phases like FeSi, Cr<sub>3</sub>Si, and Ni<sub>3</sub>C were detected. These hard phases were reported to be in the range of 9.3-11.77 GPa. Among four processed samples, sample 4 was mainly constituted of fine carbides. These hard phases were found in the range of 19.3-21 Gpa. Whereas nano hardness values of coarse carbides in sample 3 were found in the range of 17-19.5 Gpa. It was noted that the mean nano hardness value of the sample processed at 45 minutes was increased by 27 % as compared to the sample processed at 35 minutes. The standard deviation of nano hardness of sample 4 was lower among the remaining samples, which might be due to the uniform distribution of high-volume fraction of carbides (Singh and Zafar 2019). Mishra et al. developed the finite difference in the time domain model to predict time vary with temperature. Also, the effect of particle size, emissivity, and susceptor heating rate was studied (Mishra et al. 2006). Gupta et al. developed nickel-based alloy clad on the austenitic stainless-steel substrate with the help of microwave hybrid heating technique. The microstructure of the clad is free of porosity and micro-cracks with cellular morphology. The clad average microhardness was found to be 2 times compared with the stainless-steel substrate due to the formation of Cr<sub>23</sub>C<sub>6</sub> phase and intermetallic phases NiSi and FeNi<sub>3</sub> (Gupta et al. 2012). Sharma et al. developed metal ceramic

composite cladding using microwave irradiation. Clads are metallurgically bonded with the substrate. The reinforcement phase was uniformly distributed in the coating. The formation of intermetallic phases NiSi, NiW, and carbides  $W_2C$ ,  $Co_3W_3C$  in the clad increase microhardness (Sharma and Gupta 2012). In recent years, microwave energy also emerged as a novel surface engineering technique because of its higher processing speed and porous free microstructures. Kaushal et al. deposited the nickel-based alloy clad using the microwave hybrid heating technique on the steel. Results showed that the microhardness of cladding was 3.7 times that of the substrate material. The hardness of the clad was increased due to the formation of the intermetallic compound  $Ni_4W$  (Kaushal et al. 2018). Dheeraj Gupta et al. revealed that WC-12CO clad developed with microwave irradiation significantly increases microhardness. Due to the uniform distribution of nano carbides in the clad layer, wear resistance increased significantly (Gupta and Sharma 2011a). Phanendra kumar et al. carried out microwave cladding to enhance the surface properties of chromium-austenitic stainless steel. It is observed that the wear resistance of clad surface was improved by 4 times than the unclad surface. Also, 200 times less thick oxide layer was formed because of Si and Cr oxides (Phanendra Kumar et al. 2020). Durga Prasad et al. remelted the HVOF deposited coating by microwave heating to enhance the microstructural and mechanical properties. The remelted coating showed minimum porosity, excellent metallurgical bonding with the substrate, greater hardness, and higher wear resistance than the as-sprayed coating (Prasad et al. 2019b). The microwave processing gained attention due to its advantages like lower power consumption, minimum porosity, absence of thermal defects due to their atomic level volumetric heating.

## **2.5 High temperature tribological studies**

Haoliang et al. studied the high temperature tribological performance of the graphene modified WC-12Co coatings. At higher temperatures, graphene modified coating showed lower adhesion strength and hardness. However, coefficient of friction was reduced by 50 %. The graphene encapsulated coating exhibited better wear resistance than the WC-12Co coating. Various solid lubricants like soft metals, fluorides, and disulfides used in various studies. However, over usage of these lubricant additives

decrease the hardness and other mechanical properties. The selection of lubricants for specific application is also a vital task. For example, sulfides cannot use in humid environments because of their oxidation properties. Also, sulfides forms oxide layer on the surface at elevated temperatures. Likewise, fluorides and alkaline earth metals show better tribological properties at higher temperatures, but they are very brittle at lower temperatures (Si-yue 2012; Wang et al. 2017b).

In space applications, adaptive self-lubricating coatings were used by adding solid lubricants such as Ag and BaF<sub>2</sub>/CaF<sub>2</sub> in the matrix phases (NiCr, NiCo, and NiMoAl) (Dellacorte and Fellenstein 1997; Sliney et al. 1994). Li et al. improved the tribological properties of the Cr18Ni9Ti alloy discs at elevated temperatures by adding lubricant additives Ag and BaF<sub>2</sub>/CaF<sub>2</sub>. With the increasing of temperature, coating showed lower coefficient of friction and wear rate due to the synergistic lubrication effects of Ag, BaF<sub>2</sub>/CaF<sub>2</sub>, Ag<sub>2</sub>MoO<sub>4</sub>, and BaMoO<sub>4</sub>. The optimum amount of the lubricant additives in the coating enhances tribological properties. Many researchers have also studied the extensive use of solid lubricants in the composites. The high strength intermetallics with solid lubricants like Ag/BaF<sub>2</sub>.CaF<sub>2</sub>, MoS<sub>2</sub>/hBN, and Ag/BaCrO<sub>4</sub> etc. were prepared recently by various techniques like spark plasma sintering and hot-pressed sintering (Shi et al. 2013; Zhang et al. 2016; Zhu et al. 2011). It was evident from the results that the encapsulation of lubricant phase in the composite coating further enhanced the wear and friction properties at wide range of temperatures. Bayata et al. performed high temperature wear test for Inconel 751 super alloy and stainless steel. It was observed that formation of mixed spinal oxides on these alloy structures support the formation of tribo layer. Also, the carbides and other formed precipitates in the coating changed the transition from severe wear regime to the mild wear. These Ni<sub>3</sub>(Ti, Nb, Al) and Ni<sub>3</sub>Nb precipitates and other formed carbides have significant role to achieve wear properties (Bayata and Alpas 2021). Bhosale et al. investigated the high temperature wear behaviour of the WC-Cr<sub>3</sub>C<sub>2</sub>-Ni plasma sprayed coatings. Due to the development of tribo-film in the process, specific wear rates of the coatings were declined rapidly after 600 °C. As Ni-alloy has superior wear resistance than the other alloys, WC-Cr<sub>3</sub>C<sub>2</sub>-Ni can be used in the high-temperature gas cooled nuclear reactors. The presence of WO<sub>3</sub> and MWO<sub>4</sub> phases formed on both coatings controls the wear rates at elevated temperatures

(Bhosale et al. 2020). Liu et al. studied the high temperature wear behaviour of VN/Ag composites. During the high temperature process, Ag,  $\text{Ag}_3\text{VO}_4$ ,  $\text{AgVO}_3$ , and  $\text{V}_2\text{O}_5$  were formed, which were further reduced wear rate by providing adequate lubrication. The lubricant layer formation on the surfaces reduced the wear and thus contributed to the improvement of reliability and service life (Liu et al. 2021a). Tan et al. performed tribological studies on the Al-Si/SiAlON composites. The results showed promising results due to the addition of SiAlON ceramic particles. Also addition of SiAlON improved the load bearing effect and dispersion strengthening effect, which were beneficial for the formation of tribolayer on the surface (Tan et al. 2021). Karmakar et al. analysed comparative high temperature wear behaviour of stellite 6 and stellite 6/30% WC alloy. The presence of WC particles in the clad improved the wear resistance up to 650 °C. The formed micro-cuts in the wear operation have no detrimental effect for abrasive wear resistance. The wear loss of the laser remelt surfaces was increased uniform manner. However, wear rate of laser clad stellite 6 composite layers varied without any trend (Karmakar et al. 2021). Zhou et al. improve the wear resistance of the machine tools by incorporating the  $\text{WS}_2$  and  $\text{Ti}_3\text{AlC}_2$  reinforcements in the NiCoCrAlY coating. With the addition of  $\text{WS}_2$  and  $\text{Ti}_3\text{AlC}_2$  in the coatings, COFs of the coatings were reduced further by 20.9 % and 39.1 %, respectively. The wear rates also reduced by 35 % and 65 %, indicating that the self-lubricating phases significantly improve the wear resistance at elevated temperatures. In these coatings mainly adhesive wear is the main mechanism. Whereas oxidative wear and abrasive wear accelerate material loss in the process (Zhou et al. 2021). Franco et al. studied the wear behaviour of the  $\text{ZrO}_2\text{-Al}_2\text{O}_3$  plasma spraying coatings for glass industry applications where high temperature is involved. At room temperatures, wear by ductile formation was observed. As increasing the temperature from room temperature to 500 °C, brittle formation was observed. However, at very high temperatures like 1000 °C, both ductile and brittle formation was observed. This may be happened due to the softening of alumina, zirconia, and glass with the rise of temperature (Franco et al. 2021). To summarize, elevated temperature mainly effects the tribological properties through following aspects: bulk properties, reactivity, and tribo layer formation. The mechanical properties and other material properties remarkably depend on various environmental factors such as

temperature, atmosphere, therefore, investigating the elevated temperature tribological performance of nickel-based coatings has considerable research and practical significance.

## **2.6 Objectives of the work**

From the literature, it is observed that tribological performance studies of microwave treated clad layer are limited. Following are proposed objectives.

1. Development of self-lubricating composite coatings by TIG and microwave claddings with optimum process parameters.
2. To study the effect of major TIG processing parameters i.e. current and scan speed on hardness value and micro structure of the developed composite coatings.
3. To study the effect of exposure time in microstructure and mechanical properties of microwave processed clad.
4. The microstructure and mechanical properties (optical and scanning electron image with composition analysis, XRD, micro hardness, porosity, scratch resistance, fracture toughness, interfacial bond strength and EBSD studies) will be studied to evaluate the potential of the high temperature wear resistant coatings.
5. To evaluate the adhesive wear behavior of composite coatings at elevated temperatures under various test parameters using pin on disc apparatus, and assess the comparative study of wear behavior of TIG and Microwave clads.

Despite these number of findings on nickel alloy coatings, studies on the deposition of nickel alloy coating on titanium alloy with TIG cladding and microwave cladding method is limited. Also, there is no combined study found on the effect of high and low-temperature solid lubricant phases on the tribological performance for both TIG and microwave clads. Henceforth, the amendment of titanium 31 alloy substrate surface was done with nickel alloy coatings containing reinforcement and various lubricating phases with both cladding techniques. Furthermore, the effect of current in TIG cladding technique and exposure time in microwave cladding technique on the microstructure, microhardness, fracture toughness, grain refinement, and high-temperature wear performance were investigated. The clad samples are characterized using Scanning Electron Microscope (SEM), Energy Dispersive Spectroscopy (EDS)

and X-ray diffraction (XRD), optical profilometer, electron back scatter diffraction (EBSD). Micro hardness, fracture toughness, and porosity. High-temperature tribological behaviour of the clads were further studied at different testing parameters.

## **2.7 Outline of the thesis**

The systematic study conducted with respect to above objectives is presented in the thesis. A brief skeletal structure of the thesis is detailed as below.

- Chapter 1 aims at providing necessary details of the research in various cladding materials, TIG and microwave claddings.
- Chapter 2 focuses on exhaustive literature survey of nickel alloys and cladding techniques, self-lubricating claddings, and high temperature tribological performance followed by objectives of the present work.
- Chapter 3 focuses on the substrate and coating powders used to develop the composite claddings, cladding techniques adopted and testing methodology.
- Chapter 4 presents the experimental results of microstructural and mechanical characterization, wear behaviour of the composite claddings at elevated temperature.
- Chapter 4 highlights the significant conclusions drawn from the results obtained in the study.

## CHAPTER 3

### MATERIALS AND METHODS

#### 3.1 Substrate

In the present study, Grade 31 titanium alloy is selected as a substrate material procured from Midhani Ltd. India. It has high strength to weight ratio and shows high specific strength even at elevated temperatures. It has numerous applications in rocket motor, structural forgings and fasteners, pressure vessels, chemical gas pumps, marine components and steam turbine blades etc. The chemical composition of titanium 31 alloy is presented in Table 3.1. The wire-cut EDM was used to trim the substrate samples to the required dimension prior to the cladding processes. For wear studies, samples of dimension 5.2 x 5.2 x 6 mm are used. The chemical composition of the titanium 31 alloy substrate material is listed in Table 3.1.

Table 3. 1 Chemical composition (wt. %) of Titanium 31 alloy.

C	O	N	H	V	Al	Fe	Others		Ti
							Each	Total	
0.01	0.1751	0.0031	0.0042	3.91	6	0.04	<0.10	<0.40	Balance

#### 3.2 Coating material

The commercially available NiCrSiB/WC powder of particle size ranging from 20 to 70  $\mu\text{m}$  was chosen as the base coating material. The chemical composition of NiCrSiB/WC composite powder is shown in Table 3.2. The nickel alloy powder was gas atomized and procured from Hogan's India Ltd. The solid lubricants Ag (10–30  $\mu\text{m}$ ), BaF<sub>2</sub> (10–40  $\mu\text{m}$ ), and hBN (20–40  $\mu\text{m}$ ) were procured from Alpha Chemica Ltd. The solid lubricant MoS<sub>2</sub> (10–30  $\mu\text{m}$ ) was procured from Loba Chemie Pvt Ltd, Mumbai, India. The commercially available solid lubricants Ag, MoS<sub>2</sub>, BaF<sub>2</sub>, hBN were mixed with the nickel alloy powder proportionately mixed well using a tumbler.

mixer by rotating around 24hrs. The composition of the powders used for clad preparation is presented in Table 3.3.

Table 3. 2 Chemical composition of NiCrSiB/WC composite powder (wt. %).

Ni	Cr	Si	B	Fe	C	W	Others
Balance	7.33	2.21	1.67	1.91	2.37	47.7	<0.10

Table 3. 3 Composition of various coating powders for wear test (wt. %).

Coating	NiCrSiB/WC	Ag	BaF <sub>2</sub>	MoS <sub>2</sub>	hBN
NiCrSiB/WC/MoS <sub>2</sub> /BaF <sub>2</sub>	85	----	10	5	----
NiCrSiB/WC/MoS <sub>2</sub> /hBN	85	----	----	5	10
NiCrSiB/WC/Ag/BaF <sub>2</sub>	85	5	10	----	----
NiCrSiB/WC/Ag/hBN	85	5	----	----	10

### 3.3 TIG cladding

The TIG cladding experiment was conducted using the Fronius Magic Wave 400 machine equipped with a water-cooled head torch. The experimental set up of the TIG cladding is shown in Fig. 1. The TIG torch was attached to the CNC table to make the controllable linear movement. Primary shielding gas flow from the nozzle could protect the instantaneous clad pool and secondary gas flow located behind the torch head was used to protect the clad layer from the oxidation, respectively. Prior to cladding operation, the plates of dimension 50 × 50 × 6 mm were cut, and the surface was polished using emery papers and cleaned using acetone to remove any oxide layer or to remove contaminants prior to cladding. The composite powders were mixed with 10% polyvinyl alcohol to make the paste-like solution. The sample was precoated to form a uniform 1 mm-thick layer on the substrate with the help of a



metallic sheet. The experimental processing conditions of TIG cladding for various claddings are shown in Table 3.4.

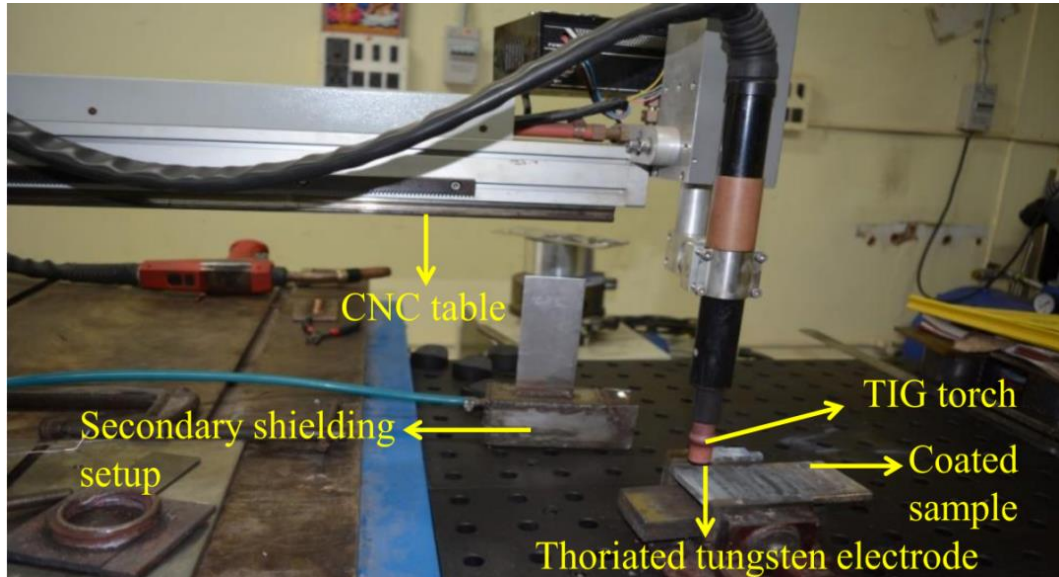


Figure 3. 1 Experimental setup of the TIG cladding method.

Table 3. 4 TIG cladding experimental processing conditions.

Electrode	2 % Thoriated tungsten of diameter 2.4 mm
Current, A	70, 75, 80, 85, 90, 95, 100, 105, 110
Scan speed, mm/s	1.6, 2
Shielding gas, l/min	Primary 10, Secondary 20 (99.99% pure argon)
Electrode gap, mm	3

### 3.4 Microwave cladding

The microwave cladding setup is developed using an alumina casket with a hot zone of 40mm (LG, India, Solar DomModel No: ML-3483FRR). The commercially available graphite sheet (Graphite India Ltd. India) of 1mm thickness placed between silicon carbide susceptor and coating powder. Before the cladding process, the substrate having size 20 x 20 x 6 mm, is polished with 600 grit emery papers and

subsequently cleaned with acetone. The powder is mixed with 10 % polyvinyl alcohol (PVA) and evenly applied to the substrate with a metallic mask. The pre-coated substrate was kept on the muffle furnace for 2 hours at 50°C. The PVA aid the powdered particles cohesively bonded and uniformly distributed on the substrate. Fig. 2 shows the experimental setup of microwave hybrid heating system. The microwave processing conditions for all composite clads is shown in Table.



Figure 3. 2 Experimental set up of microwave hybrid heating mechanism.

Table 3. 5 The microwave cladding processing conditions.

Power, W	900
Frequency, GHz	2.45 GHz
Exposure time, min	5, 10, 15, 20
Silicon carbide, mm	25 x 25 x 8
Graphite sheet, mm	1

### 3.5 Porosity and dilution of the samples

The porosity of the coatings is measured as per ASTM (B276-05) standard. Image analyzer with biovis materials plus software is utilized to determine the porosity values. In all clads, various locations are considered in each sample and the average value is reported. The dilution is calculated using the equation suggested by Yaedu and d'Oliveira (Yaedu and D'Oliveira 2005) as follows:

$$D (\%) = \frac{T_{i_{coating}} - T_{i_{powder}}}{T_{i_{substrate}}}$$

(Eq 1)

where  $T_{i_{coating}}$  represents the percentage of the Ti content in the coating,  $T_{i_{powder}}$  is the amount of Ti content in the powder, and  $T_{i_{substrate}}$  is the Ti content in the substrate material.

### 3.6 Microhardness, fracture toughness and interfacial strength

The microhardness of the coatings was measured using the OMNITECH Vickers microhardness tester, and the indentations were performed on the polished cross-section of the sample using a normal load of 300 g. The dwell time was 10 sec. The fracture toughness of the coating is calculated by the following equation proposed by Evans and Wilshaw (Evans and Wilshaw 1976). The Vickers indentation tester is shown in Figure 3.4.

$$K_{IC} = 0.079 \left( \frac{P}{a^{3/2}} \right) \log \left( 4.5 \frac{a}{c} \right) \text{ for } 0.6 \leq \frac{c}{a} \leq 4.5$$

(2)

where P = applied load, a = half indentation diagonal, c = (crack length + half indentation diagonal).

To know the substrate-coating interfacial strength, indentations of 500 gf, 1000 gf, 2000 gf were performed along the interface using Vickers indentation technique.

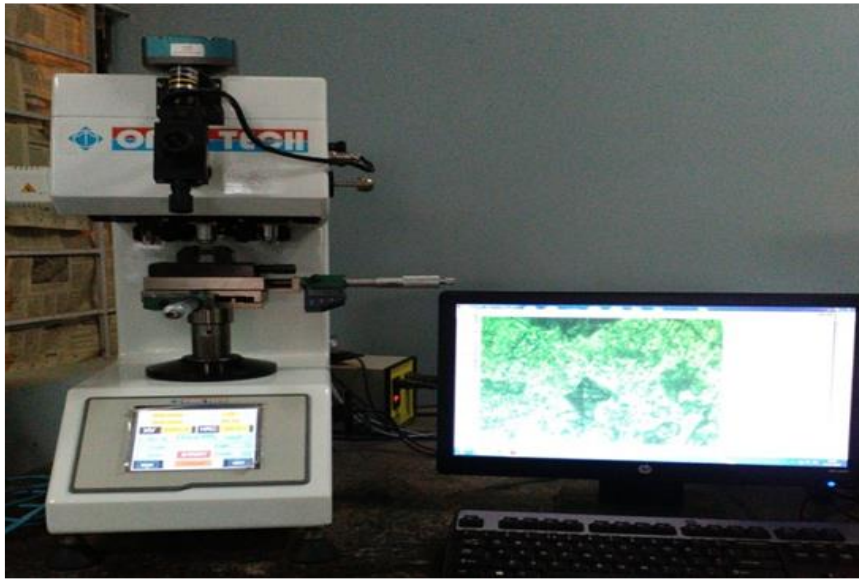


Figure 3. 3 Vickers microhardness tester.

### **3.7 Microstructure and phase analysis**

The clad samples are sectioned using slow cutting machine and polished for metallographic examination. The cross-sectional images of each coating were observed using the scanning electron microscopy (SEM) equipped with energy dispersive X-ray analysis (EDX) (TESCAN Vega 3LMU, made in the Czech Republic). The X-ray diffraction (XRD) studies were conducted on an analytical Empyrean diffractometer (30 kV and 20 mA with Cu  $K_{\alpha}$  radiation), with a step size of 0.02. Grain size distributions in the area fraction and inverse pole figure (IPF) maps were extracted and studied using the EBSD technique.

### **3.8 Sliding wear test**

The tribological studies are conducted using pin on disc tribometer (TR-20LE-PHM 400 - CHM 600, Ducom Instruments Pvt Ltd, Bangalore, India). The high-temperature wear studies were conducted using the pin on disc wear machine. Prior to wear studies, samples were cut into  $5.2 \times 5.2 \times 6$  mm, and polished the coating surface with 600 grit emery paper to make the surface flat for better contact with the alumina ( $Al_2O_3$ ) disc. Test is conducted under dry conditions as per (ASTM G99-05) standard. Alumina disc is used as the counter body. The wear test parameters used in the study is presented in Table 3.6. The experimental set up of the tribometer is shown

in Figure 3.5. A computer-aided data acquisition system is utilized to concurrently record both height loss (using in built displacement transducer) and frictional force. Friction coefficient is computed by dividing the frictional force by normal load. The experimental set up of the pin on disc apparatus is shown in Figure 3.5. The effect of load and temperature on weight loss, coefficient of friction, and wear rate was investigated. The wear rates are calculated using weight loss method. After the wear studies, contact surfaces were considered for morphological studies with SEM and XRD analysis. Surfaces were analyzed using a 3D surface profilometer to study the topography of the worn-out samples.

**Sample Calculations:**

$$\text{Time} = \text{sliding distance}/\text{sliding velocity}$$

$$\text{Sliding velocity (v)} = \pi DN/60$$

$$\text{Volume loss (mm}^3\text{)} = \text{contact area} \times \text{material worn out}$$

$$\text{Wear rate} = \text{volume loss}/\text{sliding distance (mm}^3\text{/m)}$$

In order to calculate wear rate by weight loss method Eq. 2 was used.

$$W_r = \frac{\Delta m}{F.L.\rho} \times 10^6$$

Where  $W_r$  is wear rate in term of  $\text{mm}^3\text{/N m}$ , and  $\Delta m$  is a loss of weight in term of mg,  $F$  is applied force in N, and  $L$  is the sliding distance in m, and  $\rho$  is coating density in  $\text{g/cm}^3$ .



Figure 3. 4 Pin on disc tribometer experimental set up.

Table 3. 6 Wear test parameters

Test Parameters	Variables
Load, N	10, 20
Temperature, °C	200, 400, 600
Sliding Distance, m	1000

## CHAPTER 4

### RESULTS AND DISCUSSIONS

#### 4.1 Morphology of the cladding powders

Scanning micrographs of the composite powders NiCrSiB/WC, NiCrSiB/WC/Ag/BaF<sub>2</sub>, NiCrSiB/WC/Ag/hBN, NiCrSiB/WC/MoS<sub>2</sub>/BaF<sub>2</sub>, NiCrSiB/WC/MoS<sub>2</sub>/hBN are presented in Figure 4.1. Also, various solid lubricant powders used in the study are shown in Figure 4.2.

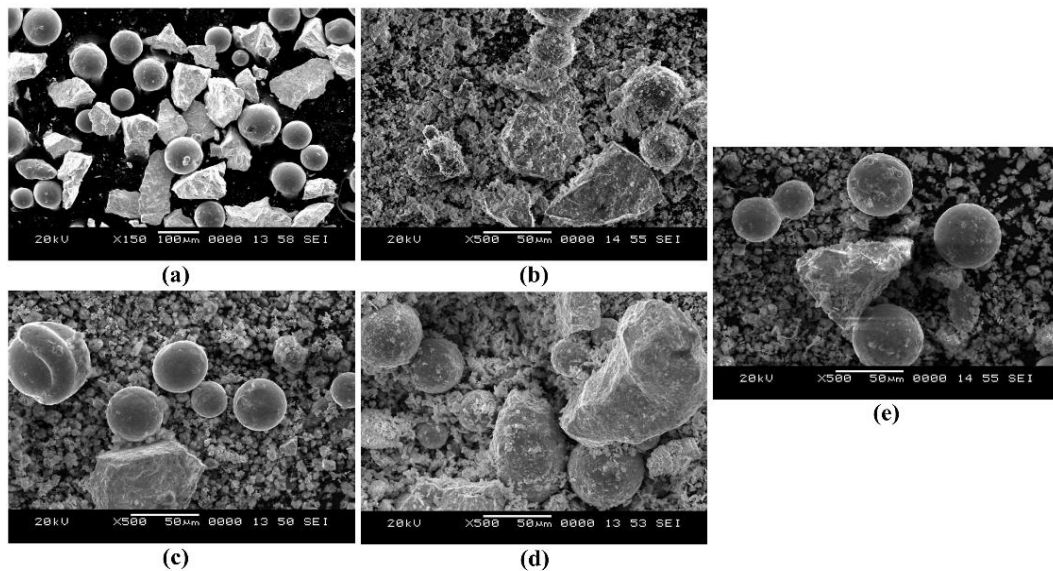


Figure 4. 1 Morphology of the cladding powders (a) NiCrSiB/WC (b) NiCrSiB/WC/Ag/BaF<sub>2</sub> (c) NiCrSiB/WC/Ag/hBN (d) NiCrSiB/WC/MoS<sub>2</sub>/BaF<sub>2</sub> (e) NiCrSiB/WC/MoS<sub>2</sub>/hBN.

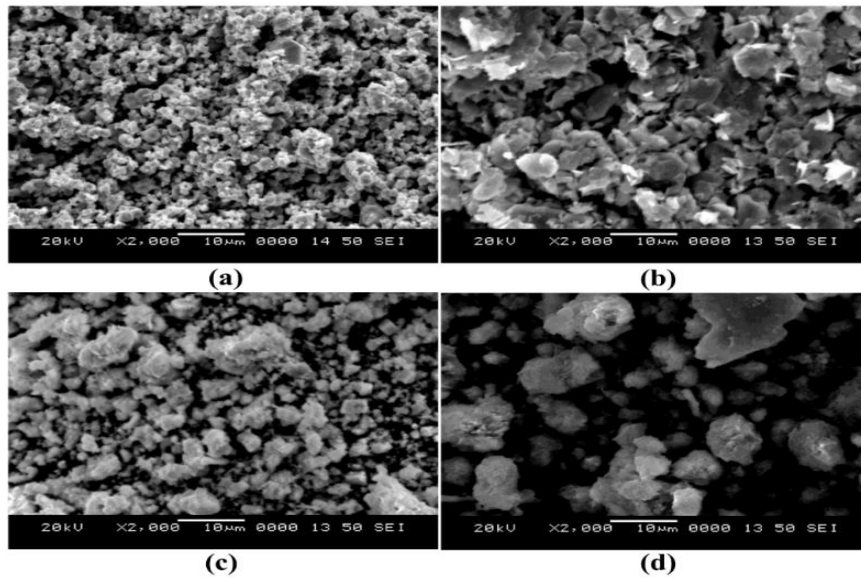


Figure 4. 2 morphology of the solid lubricant powders (a) Ag (b) MoS<sub>2</sub> (c) BaF<sub>2</sub> (d) hBN.

The powders are mixed using Tumbler mixer around 24 hours to attain uniform mixture. It can be seen from Figure 4.1 that powders are well mixed affirming suitability and feasibility of the tumbler mixing method.

#### 4.2 Visual inspection of the deposited clads

The images of the deposited TIG clads are shown in Figure 4.3. It can be seen that all clads are free from surface cracks. TIG current and scan speed are varied during deposition of clad layers. Based on the microstructural and mechanical properties, appropriate clad layer is selected for testing of tribological performance. Similarly, images of the microwave clads are shown in Figure 4.4. Based on the microstructural characterization, various clads were selected based on optimum exposure time. The color of appearance of the various clads was changed due to the involvement of solid lubricant particles.



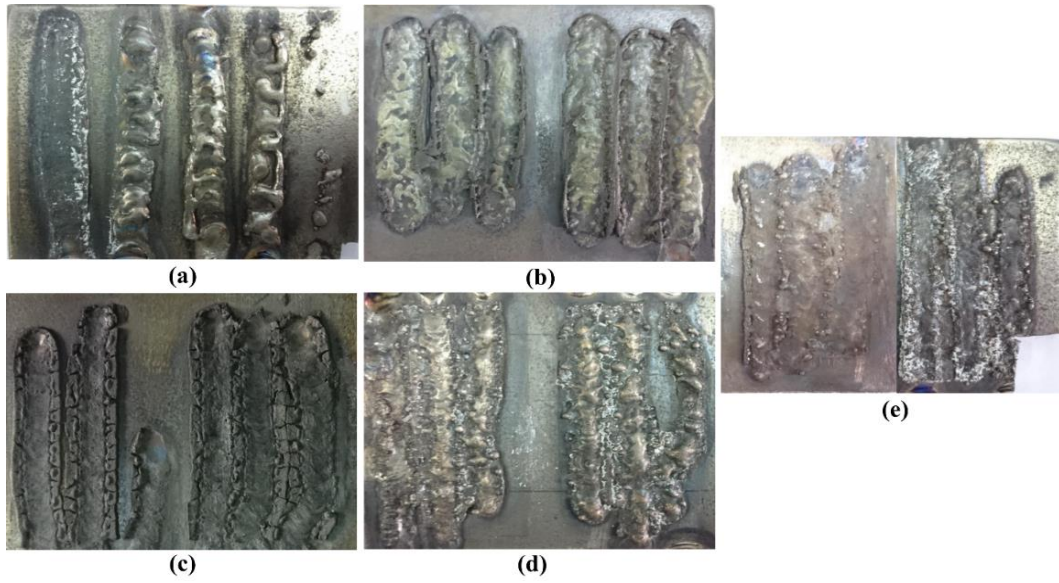


Figure 4. 3 Images of the TIG cladding layers processed at various process parameters  
 (a) NiCrSiB/WC (b) NiCrSiB/WC/Ag/BaF<sub>2</sub> (c) NiCrSiB/WC/Ag/hBN (d)  
 NiCrSiB/WC/MoS<sub>2</sub>/hBN (e) NiCrSiB/WC/MoS<sub>2</sub>/BaF<sub>2</sub>.

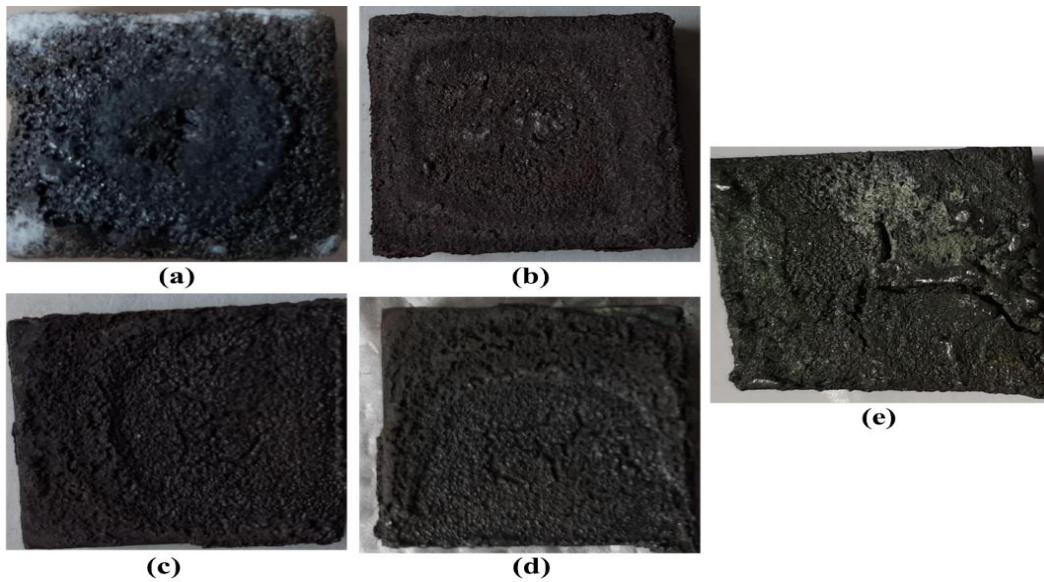


Figure 4. 4 Images of the Microwave clads processed at optimized process parameters  
 (a) NiCrSiB/WC (b) NiCrSiB/WC/Ag/BaF<sub>2</sub> (c) NiCrSiB/WC/Ag/hBN (d)  
 NiCrSiB/WC/MoS<sub>2</sub>/hBN (e) NiCrSiB/WC/MoS<sub>2</sub>/BaF<sub>2</sub>.

### 4.3 Porosity and dilution of the claddings

The porosity of the claddings is the prime importance for obtain better tribological properties. The porosity of the claddings is evaluated using optical microscope attached with image analyser. Based on the classification of pore sizes and involved phases, porosity percentage was calculated. The porosity values of the TIG clads are presented in Table 4.1. The thermal gradient has significant effect on porosity. A decrease in porosity was observed as the heat input increased. Similarly, porosity of the microwave clads are presented in Table 4.2. The dilution also is an important concern to obtain quality clads with better mechanical properties. The dilution of the TIG clads obtained at various process parameters is shown in Table 4.1. Similarly, dilution of the MHH clads at optimized exposure time is shown in Table 4.2.

Table 4. 1 Porosity and dilution of the TIG clads.

TIG Cladding	Average porosity (%)	Average dilution (%)
NiCrSiB/WC	1.49±0.25	10.18±5.43
NiCrSiB/WC/Ag/BaF <sub>2</sub>	1.20±0.30	9.43±1.65
NiCrSiB/WC/Ag/hBN	1.60±0.28	18.65±2.5
NiCrSiB/WC/MoS <sub>2</sub> /hBN	1.50±0.21	22.22±6.0
NiCrSiB/WC/MoS <sub>2</sub> /BaF <sub>2</sub>	1.50±0.32	23.04±3.2

Table 4. 2 Porosity and dilution of the MHH clads.

MHH Cladding	Average porosity (%)	Average dilution (%)
NiCrSiB/WC	0.99±0.15	2.12±0.36
NiCrSiB/WC/Ag/BaF <sub>2</sub>	0.70±0.10	2.64±0.72
NiCrSiB/WC/Ag/hBN	0.85±0.22	3.56±0.65
NiCrSiB/WC/MoS <sub>2</sub> /hBN	0.95±0.19	3.82±0.50
NiCrSiB/WC/MoS <sub>2</sub> /BaF <sub>2</sub>	0.93±0.22	3.22±0.95

#### 4.4 Microhardness and fracture toughness of the claddings

The indentations were performed along the cross section using Vickers hardness tester throughout the clad depth. As the TIG current increases from 70 A to 110 A, reduction in micro hardness value was observed. Also, it is noted that the clad surface holds higher hardness value, and gradual reduction of hardness value is observed towards the interface. Due to the collected WC particles at the bottom, there is a sudden increment in micro hardness. The phases obtained in all TIG processed clads such as Cr<sub>23</sub>C<sub>6</sub>, WC, W<sub>2</sub>C, WB, Cr<sub>7</sub>Ni<sub>3</sub> and intermetallic phase Ni<sub>4</sub>W are mainly responsible for achieving high hardness. It is clear that the 15% encapsulation of solid lubricant phase in the composite clads leads to the reduction in hardness value. The micro hardness values of the all TIG bulk composite clads varied from 1500 HV<sub>0.3</sub> - 650 HV<sub>0.3</sub>, which is about 2.03 to 4.68 times as that of the titanium 31 substrate (approximately 320 HV<sub>0.3</sub>). The microhardness of the TIG clads is shown in Table 4.3.

Also, in MHH claddings, reduction of microhardness value is observed as moving from clad surface to the substrate. The results show that the microhardness of the reinforcement phase significantly higher than the nickel matrix phase. The hardness of the nickel alloy matrix increased to some extent because of the WC dissolution. In MHH cladding also, reduction of microhardness value is observed as moving from clad surface to the substrate. The deviation of microhardness values

along the clad depth indicates the random distribution of hard phases in the clad because of diffusion, thermal gradient, and the availability of alloying elements. The average microhardness values of the MHH deposited clads at optimum exposure time is shown in Table 4.3.

Table 4. 3 Average microhardness values the TIG and MHH claddings.

Cladding	TIG cladding (70 A – 110 A)	MHH cladding (15 min)
	(HV)	(HV)
NiCrSiB/WC	925-725 ± 18	710 ± 20
NiCrSiB/WC/Ag/BaF <sub>2</sub>	830-638 ± 15	675 ± 15
NiCrSiB/WC/Ag/hBN	1054-628 ± 20	650 ± 20
NiCrSiB/WC/MoS <sub>2</sub> /hBN	1152-489 ± 20	680 ± 25
NiCrSiB/WC/MoS <sub>2</sub> /BaF <sub>2</sub>	970-550 ± 25	620 ± 35

The fracture toughness values of the clads were noted for both TIG and MHH clads on the clad region. Loads such as 500 gf, 1000 gf and 2000 gf were indented on the clad region. The calculations were done by considering the crack parameters. It was noted that the cracks mainly appeared at 2000gf, which was mainly due to ceramic phase included in the clad. The fracture toughness of both TIG and MHH clads are shown in Table 4.4.

Table 4. 4 Average fracture toughness of the TIG and MHH clads.

Cladding	TIG cladding	MHH cladding
NiCrSiB/WC	3.39	5.7
NiCrSiB/WC/Ag/BaF <sub>2</sub>	4.83	6.35
NiCrSiB/WC/Ag/hBN	5.25	6.42
NiCrSiB/WC/MoS <sub>2</sub> /hBN	5.76	6.76
NiCrSiB/WC/MoS <sub>2</sub> /BaF <sub>2</sub>	6.22	6.91

#### 4.5 Microstructure of the deposited clads

##### 4.5.1 NiCrSiB/WC TIG claddings

The cross-sectional SEM images of NiCrSiB/WC clads fabricated on titanium 31 substrate are shown in Figure 4.5. Figure 4.6 represents the magnified cross-sectional images of TIG clad deposited at 70A current. It can be seen that clad is metallurgically bonded with the substrate. Near to the interface, interdendritic eutectic precipitations are found, as can be seen in Figure 4.6b. Figure 4.6a shows blocky white shaded particles (region B), and grey shaded particles (region C) are primarily containing W and C and W and Ni (shown in Table 4.5), respectively. Figure 4.6b shows the magnified SEM image of the substrate-interface region. The dendritic structures formed on the substrate growing towards the clad layer. These dendritic structures at the interface (region C) are rich in titanium and nickel (shown in Figure 4.7), and the matrix (region D) is containing nickel alloy.

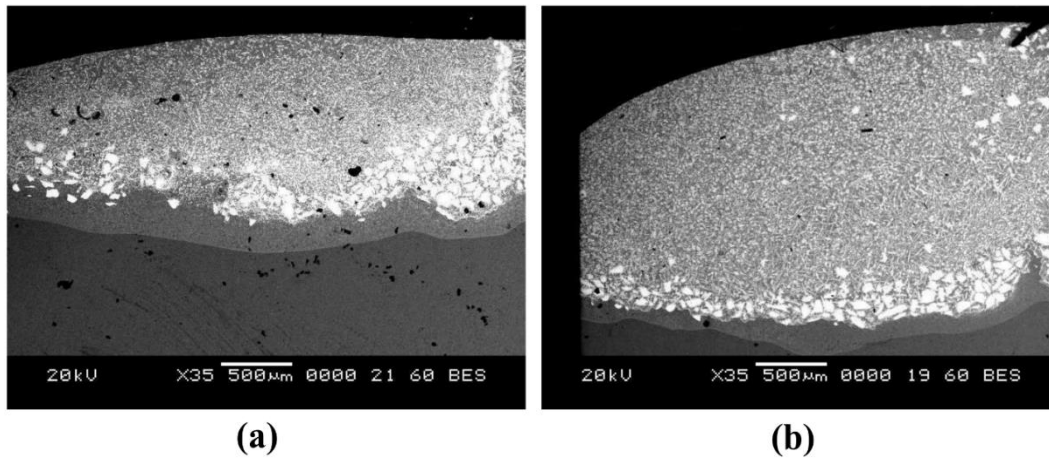


Figure 4. 5 Cross sectional SEM images of the NiCrSiB/WC clad processed at (a) 70 A (b) 95 A.

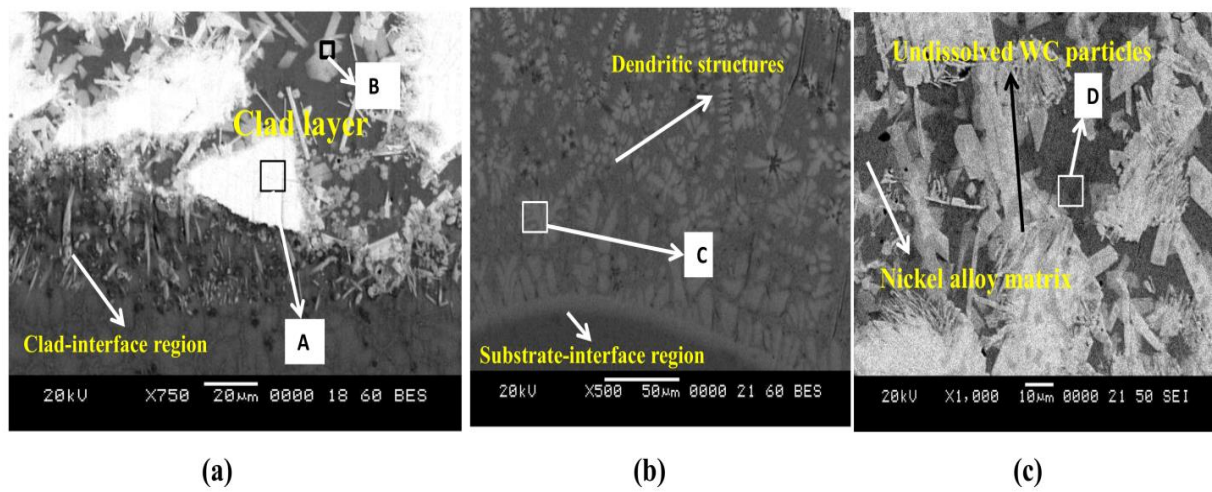


Figure 4. 6 Magnified SEM image of NiCrSiB/WC clad at (a) clad-interface region; (b) substrate-interface region; (c) clad morphology.

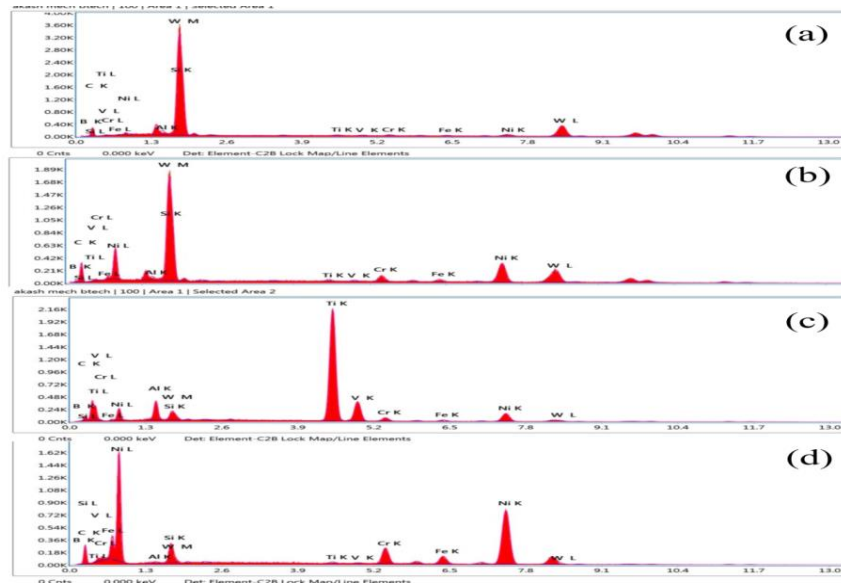


Figure 4. 7 EDX results of elemental distribution of NiCrSiB/WC clad in the selected regions (a) region A; (b) region B; (c) region C; (d) region d.

Table 4. 5 Elemental distribution of the selected regions from the NiCrSiB/WC clad EDX results.

Region	Ni	Cr	Fe	Si	B	W	C	Ti	Al	V
A	2.25	1.09	0.85	4.47	1.54	76.32	10.84	0.79	1.25	0.60
B	19.46	3.62	1.90	2.72	3.21	52.37	14.33	0.96	0.83	0.58
C	12.05	2.62	1.54	0.86	0.17	5.88	3.02	65.14	5.47	3.25
D	61.15	8.74	5.90	3.34	1.63	4.67	13.15	0.68	0.45	0.29

#### 4.5.2 NiCrSiB/WC/Ag/BaF<sub>2</sub> TIG claddings

The cross-sectional SEM images of NiCrSiB/WC/Ag/BaF<sub>2</sub> TIG clad fabricated on titanium 31 substrate are shown in Figure 4.8. The block shaped white WC particles were well embedded with the nickel alloy matrix. As shown in Figure 4.9, NiCrSiB/WC/Ag/BaF<sub>2</sub> clad samples are metallurgically bonded with the substrate. It is clear that the processing current affects the dilution of the coatings (Blau 2010). It

impacts the chemical composition and other mechanical properties. Also, thickness of the clad was increased as welding current increased from 70A to 95A. At 70A, WC particles are not fully dissolved in the nickel matrix. At 95A, WC particles are well dissolved attribute to its high fusion temperature. Due to the insufficient heat input, residual WC particles are collected at the bottom due to the higher density and melting point than nickel alloy. The weld pool convection current was not enough to prevent WC particles from sinking to the bottom (Badisch et al. 2003).

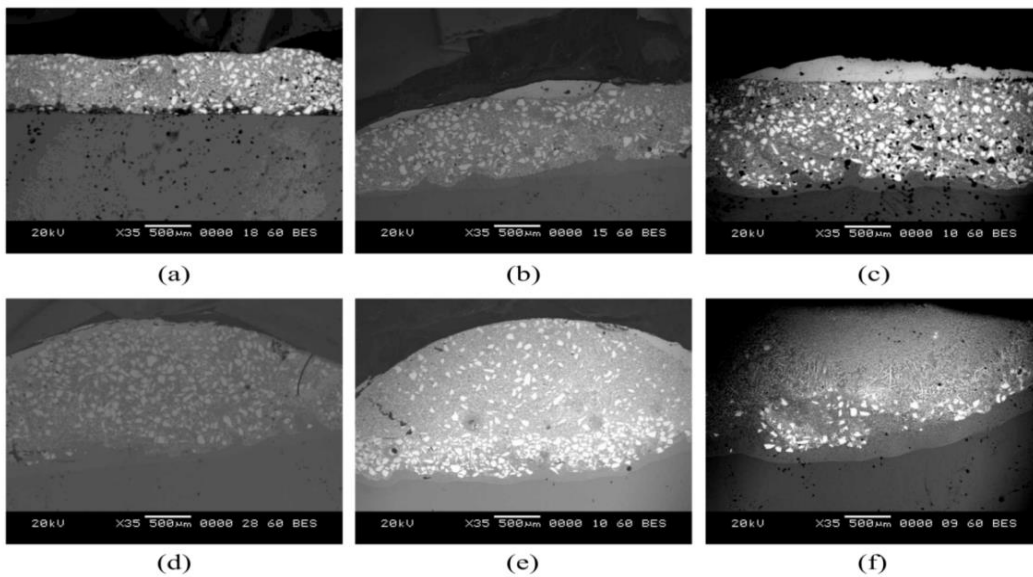


Figure 4. 8 Cross sectional SEM images of the NiCrSiB/WC/Ag/BaF<sub>2</sub> produced at the scanning speed of 2 mm/sec and process current of (a)70A; (b) 75A; (c) 80A; (d) 85A; (e) 90A; (f) 95A.

Meanwhile, it can be observed that micro cracks and few pores are apparently present in the clad. The thermal stresses induced in the clad prone to sensitivity to cracking because of high thermal gradient (Liu et al. 2019). The heat input and cooling rate affects the porosity content in the clad. Fig.4 shows the magnified SEM images of clads at 70A and 95A. (a), (b) represent the bottom of the clad at 70A and 95A respectively. It is worth to note that substrate thermal conductivity and clad process parameters mainly affect the diffusion behaviour (Wang 2004). The processing current changes the degree of dissolution of WC particles. At lower heat input, flower shaped WC particles are observed near the interface. As increasing the current, degree



of dissolution was low and blocky WC particles are concentrated near the interface. The difference in their appearance is due to the change in thermal gradient.

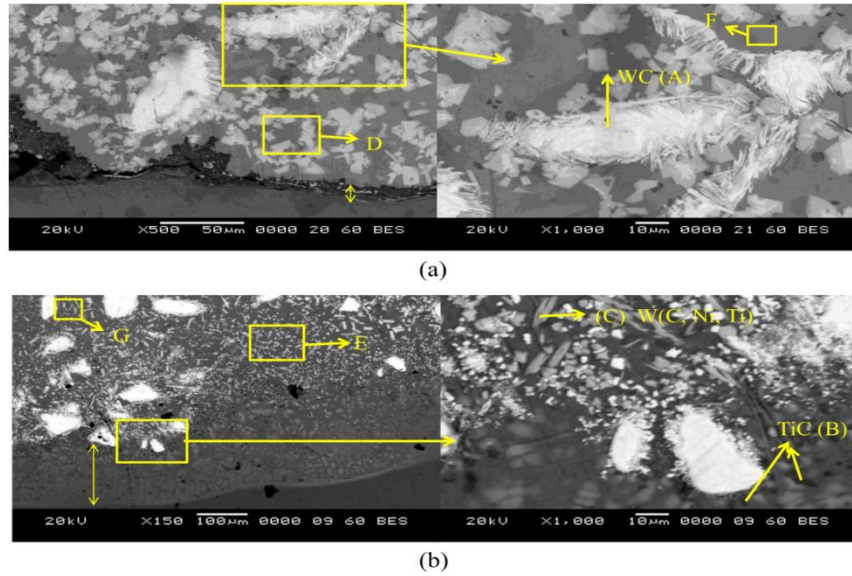


Figure 4. 9 Magnified cross sectional images of the NiCrSiB/WC/Ag/BaF<sub>2</sub> (a) Near to the interface of 70A current clad and clad morphology; (b) Near to the interface of 95A clad and clad morphology.

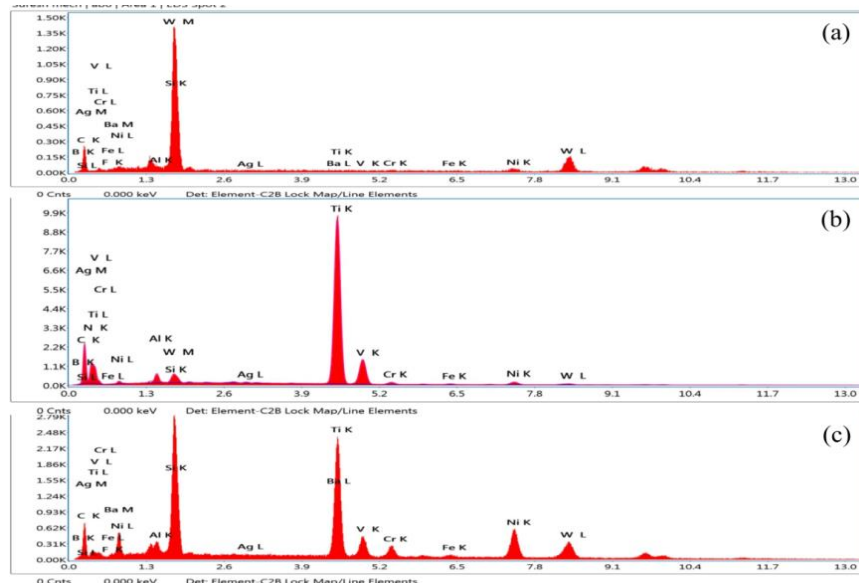


Figure 4. 10 EDX results of distribution of different phases in the NiCrSiB/WC/Ag/BaF<sub>2</sub> clad (a) phase A; (b) phase B; (c) phase C.

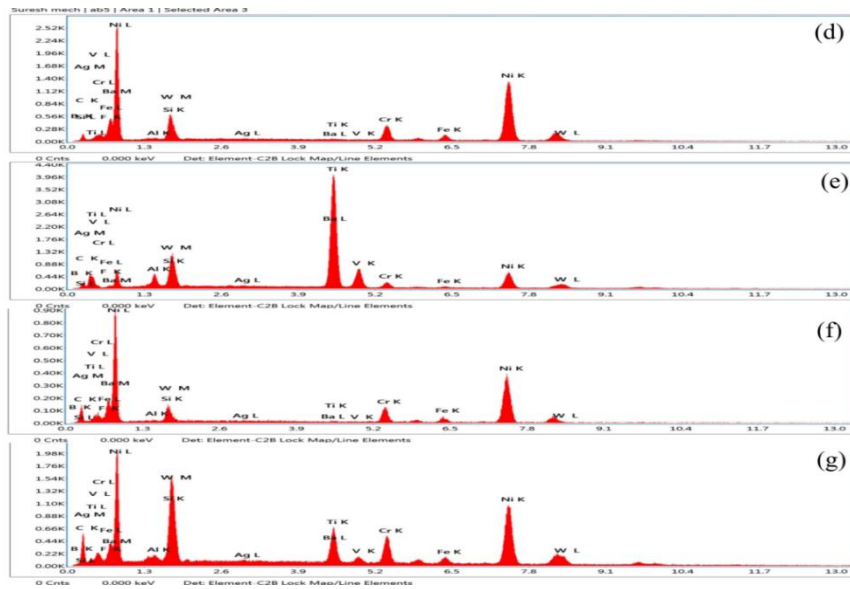


Figure 4. 11 EDX results of elemental distribution of NiCrSiB/WC/Ag/BaF<sub>2</sub> clad in the selected areas (a) Area D; (b) Area E; (c) Area F; (d) Area G.

Table 4. 6 Elemental distribution of the selected phases and areas from the NiCrSiB/WC/Ag/BaF<sub>2</sub> clad EDX results.

Region	Ni	Cr	Fe	Si	B	W	C	Ti	Al	V	Ag	Ba	F
A	3.28	0.82	1.42	3.35	2.05	66.99	18.32	0.08	1.03	0.02	0.84	1.70	0.10
B	3.69	1.10	2.34	0.39	0.26	4.82	17.71	64.65	1.82	1.49	0.47	1.2	0.06
C	13.87	3.28	1.01	2.34	2.53	30.24	13.92	25.16	1.84	1.37	0.43	4.0	0.01
D	55.90	7.30	2.25	2.91	0.81	16.66	5.34	6.19	0.60	0.02	0.52	1.09	0.41
E	16.68	3.00	1.01	1.65	0.28	15.26	3.55	49.28	3.68	2.11	0.55	2.70	0.25
F	59.76	9.47	2.29	3.48	1.06	7.15	13.83	0.18	0.44	0.01	0.74	1.24	0.36
G	37.67	6.95	1.93	3.66	1.46	10.69	15.90	15.50	1.40	0.44	0.78	3.34	0.28

From EDS results, the white granular phase is mainly rich in W and C as shown in Figure 4.10a. As shown in Figure 4.10b and c, the dark dendritic phases are rich in Ti and C and light gray shaped particles are mainly composed of W, Ti, C, Ni respectively. From Figure 4.11, Area D is mainly composed of Ni, W and includes limited percentage of Ag, Ba, F, C, Ti, Cr, Fe, and Si (shown in Table 4.6). Area E (near the interface at 95 A) has higher amount of Ti due to the dilution effect (shown in Table 4.6). Area F is mainly formed with nickel and little percentage of other elements such as C, Ti, W, Ag, Ba and F (shown in Table 4.6). It is regarded as the nickel matrix solid solution. As shown in Figure 4.9a, apparently darker dendritic and grey shaped phases are observed in 95 A clad as compared to 70 A, which is attributed to the formation of TiC, TiNi phases in the clad. Matrix, reinforcement and lubricant phases are well dispersed in the clad as shown in EDS elemental mapping (Figure 4.12).

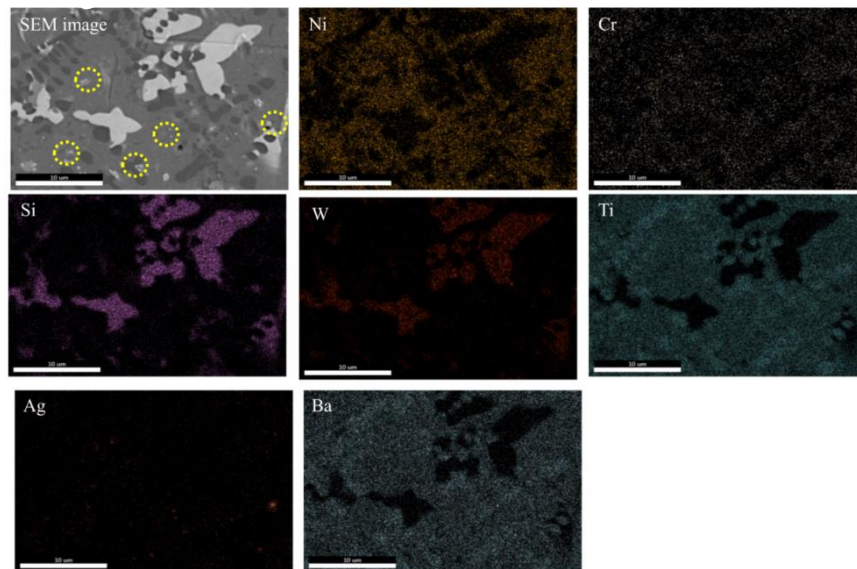


Figure 4. 12 EDX Elemental mapping of NiCrSiB/WC/Ag/BaF<sub>2</sub> clad cross section near to the top at 70A current.

Silver has low mixing enthalpy with the nickel alloy, which leads to the formation of separate precipitates during the clad development (Zhu et al. 2012). Silver (Ag) precipitates can be observed in the SEM image (Figure 4.11). However, high temperature solid lubricant BaF<sub>2</sub> is fully dissolved with the clad, instead of forming separate phase like silver. But F element was not quantified accurately. Light

elements such as B, F, H are difficult to accurately quantify by EDS analysis (Tudela et al. 2019).

#### **4.5.3 NiCrSiB/WC/Ag/hBN and NiCrSiB/WC/MoS<sub>2</sub>/hBN TIG claddings**

The cross-sectional morphologies of the NiCrSiB/WC/Ag/hBN and NiCrSiB/WC/MoS<sub>2</sub>/hBN TIG claddings produced at various currents are shown in Figure 4.14. As a result of the TIG torch melting, the preplaced powders of the clad were melted, making a dense composite clad. Both clads produced at different currents were metallurgically bonded with the substrate. The depth of the interface zone increased with the increasing current. It was seen that white irregular particles correspond to WC particles, and dark continuous matrix belong to nickel alloy as indicated by EDS analysis. The tungsten carbide particles were well embedded in the nickel alloy matrix and distributed uniformly in the molten pool, which matched the study conducted by (Sundaramoorthy et al. 2017). The carbide dissolution was increased with the TIG current. The difference in WC particle size in the clad indicates the change in a thermal gradient. The carbide dissolution formed in the nickel alloy matrix altered the dendritic structure of the nickel matrix. It was apparent that the percentage of Cr in the nickel alloy matrix facilitated the WC dissolution and facilitated the intermetallic precipitates. The higher current and fast cooling rate affected the dilution zone of the clad, which was further changing the mechanical properties of the clad.

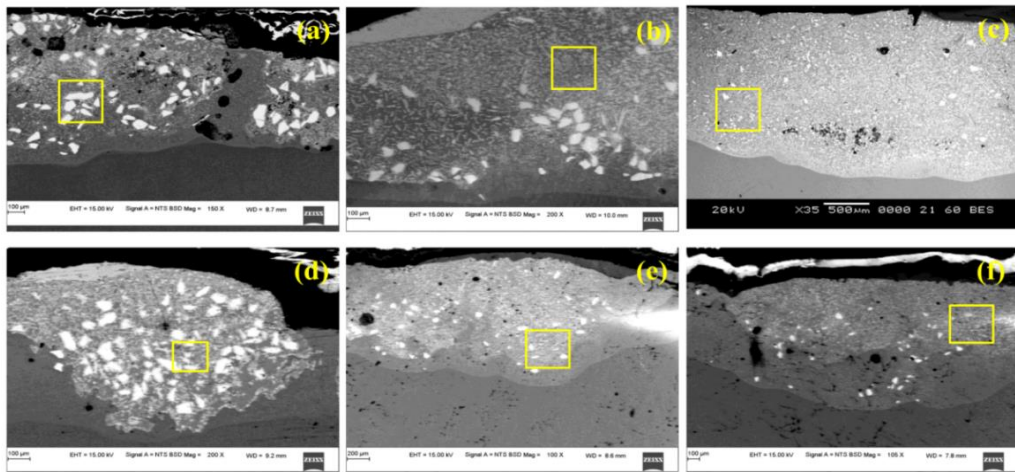


Figure 4. 13 Cross-sectional SEM images of the NiCrSiB/WC/Ag/hBN clad developed at the process current of (a) 90 A (b) 95 A (c) 100 A; NiCrSiB/WC/MoS<sub>2</sub>/hBN process current of (d) 90A (e) 95A (f) 100 A.

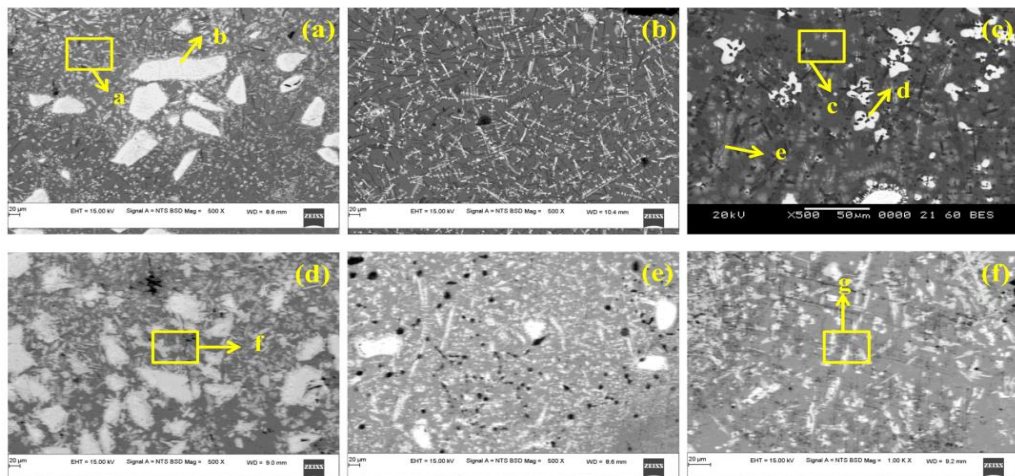


Figure 4. 14 Surface morphology of the NiCrSiB/WC/Ag/hBN clad (at different magnification) produced with a process current of (a) 90 A (b) 95 A (c) 100 A; NiCrSiB/WC/MoS<sub>2</sub>/hBN process current of (d) 90A (e) 95A (f) 100 A.

Table 4. 7 EDS analysis corresponding to SEM images shown in Fig. 3.

<b>Region</b>	<b>Ni</b>	<b>Cr</b>	<b>Si</b>	<b>W</b>	<b>C</b>	<b>Ti</b>	<b>Ag</b>	<b>Mo</b>	<b>S</b>	<b>B</b>	<b>N</b>
<b>A</b>	46.55	3.10	0.75	6.496	12.40	25.95	1.56	-	-	0.15	3.044
<b>B</b>	0.56	0.20	3.85	69.32	25.95	0.12	-	-	-	-	-
<b>C</b>	29.50	5.34	1.97	9.76	8.41	41.14	1.28	-	-	0.02	2.58
<b>D</b>	3.30	1.47	2.90	56.42	15.82	16.61	0.31	-	-	1.82	1.35
<b>E</b>	4.94	2.44	1.56	37.98	8.00	40.69	1.09	-	-	-	3.30
<b>F</b>	37.32	7.20	2.92	16.56	15.51	16.42	-	1.20	-	1.51	1.36
<b>G</b>	20.27	4.43	1.32	10.88	4.76	50.72	-	3.20	-	0.01	4.41

Figure 4.15 demonstrates the magnified SEM images of both clads produced at different processing currents. Although the distribution of particles was uniform in the clads, it can be evident that the embedded particle size varies with the increase of processing current. The EDS analysis was performed on the cross-sectioned samples to know the chemical composition of the composite layer. As revealed in Table 4.7, the white irregular particles were mainly composed of W and C (Region b). The dissolution of WC particles in the clad is reflected in Figure 4.15c, primarily composed of W, C, and a small amount of Ti. Due to the dilution effect, the percentage of titanium was increased with the current. The dissolved quantities of elements present in the clad also changed with the current, which could be due to the change of solidification rate. It was also noted that the increase of dendritic formation observed in the clad was mainly composed of W and Ti (Table 4.7). The EDS analysis was conducted in the coated regions to know the chemical composition of the clads processed at low and high currents. The NiCrSiB/WC/Ag/hBN clad at 90 A mainly comprises Ni, W, Ti, and a few solid lubricants Ag and BN. Similarly, the NiCrSiB/WC/MoS<sub>2</sub>/hBN clad processed at 90 A was primarily composed of Ni, W, Ti, and a few Mo, S, B, and N (Region F). However, with the increase of current to

100 A, the titanium element percentage increases due to the dilution effect, and it further increases the dissolving quantities of composite clad (Region C and D).

#### 4.5.4 NiCrSiB/WC/MoS<sub>2</sub>/BaF<sub>2</sub> TIG claddings

Figure 4.17 shows the cross-sectional morphology of the NiCrSiB/WC/MoS<sub>2</sub>/BaF<sub>2</sub> TIG clad layers fabricated at 90A, 100 A, and 110 A. The chemical composition of the clad layer changed while increasing the current, which leads to the change in clad mechanical properties.

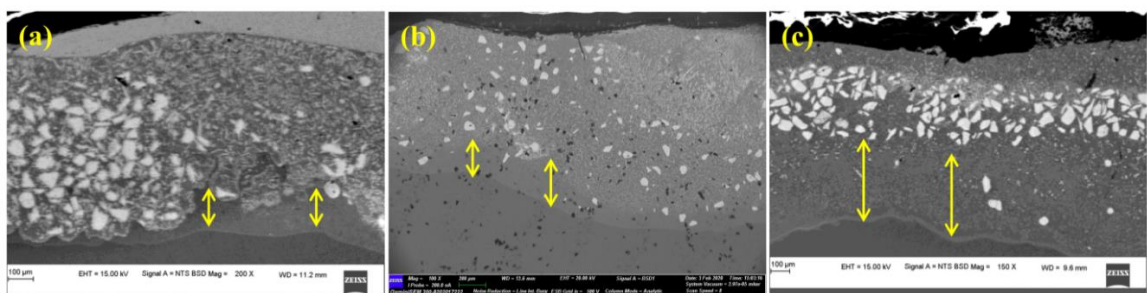


Figure 4. 15 Cross sectional SEM image of TIG clad produced at (a) 90 A (b) 100 A (c) 110 A.

The interface layer was increased as increasing TIG current from 90 A to 110 A, which further reduced the mechanical properties. It could happen due to the influence of energy input, which further changes the solidification rate of the clad. With the increase of molten pool temperature, the liquid phase near the WC particles would enhance the heterogeneous nucleation, leading to refined grains. The cross-sectional micrograph in Figure 4.18 revealed a dense homogenous clad. Most WC particles were partially dissolved in the nickel alloy matrix, with only a small amount of fully dissolved WC particles coexisting. The clad thickness on the flat surface was varied from 0.92-1.0 mm. The top region of the clad cross-section is shown in Figure 4.18a. Comparatively, a more lubricant phase was present on the top region of the clad. The bottom region was more embedded with the reinforcing phase. The white block-shaped particles were mainly rich in W and C. These WC particles were well dispersed in the nickel alloy matrix. The peripheral dissolution of WC particles in the nickel alloy would ensure the internal bonding with the matrix. The collected WC particles near the bottom of the clad, as shown in Figure 4.18b, were beneficial to

reduce the dilution of clad with the substrate. The grain growth in the interface region can be seen in Figure 4.18c.

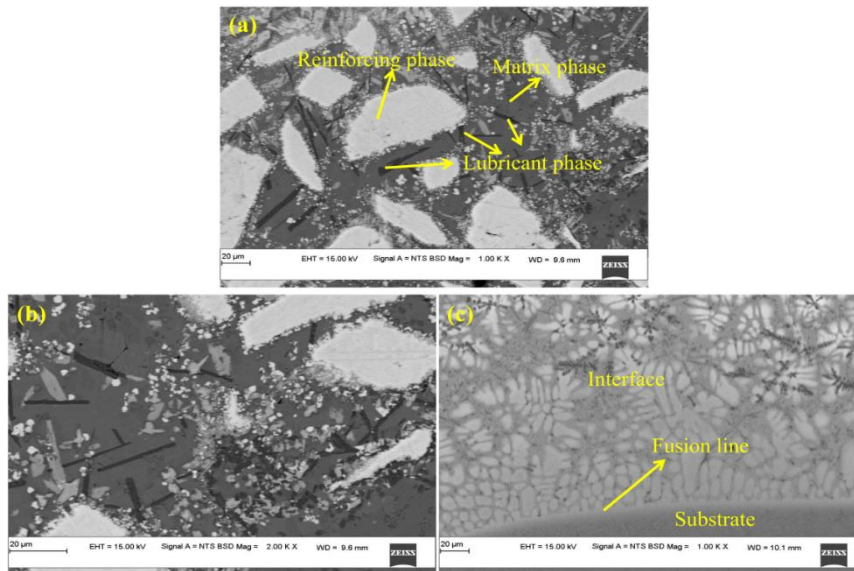


Figure 4. 16 SEM image of TIG clad at 90 A (a) top region of the clad (b) bottom region of the clad (c) clad-substrate interface region.

It might be because of the formation of a new grain nucleation core at the solid-liquid interface region, and grains remain unmelted because of intense convection in the molten pool (Kui et al. 2007). The dark thin particles observed in Fig. 4a and b were regarded as lubricant phases, mainly composed of Mo and S. The nickel alloy matrix, WC reinforcement phase, and lubricating phases MoS<sub>2</sub> BaF<sub>2</sub> were well dissolved in the clad. The difference in the phase density of WC particles and the flow rate of other liquid phases resulted in the clad's uneven distribution of WC hard phases. As the molten pool temperature decreased, the liquid phase around the WC particles adhered to their surface area to form heterogeneous nucleation, which further led to the increase of the nucleation rate of WC.

#### 4.5.5 NiCrSiB/WC MHH clad

Figure 4.19 presents the cross-sectional image of 1mm thick NiCrSiB/WC clad developed by microwave hybrid heating. Due to the complete melting of preplaced powder and its subsequent solidification, no visible cracks and defects are observed in



both clad attributed to the low thermal gradient. The inverse thermal gradient is the common phenomenon observed in microwave radiation, mainly responsible for generating convection currents in the melt pool. The wavy interface indicates the metallurgical bonding of cladding with the substrate material. The presence of Cr in the nickel alloy matrix can enhance the WC dissolution and causes the formation of intermetallic precipitates (Flores et al. 2009; Liyanage et al. 2012). The WC block-shaped particles can be seen in Figure 4.19.

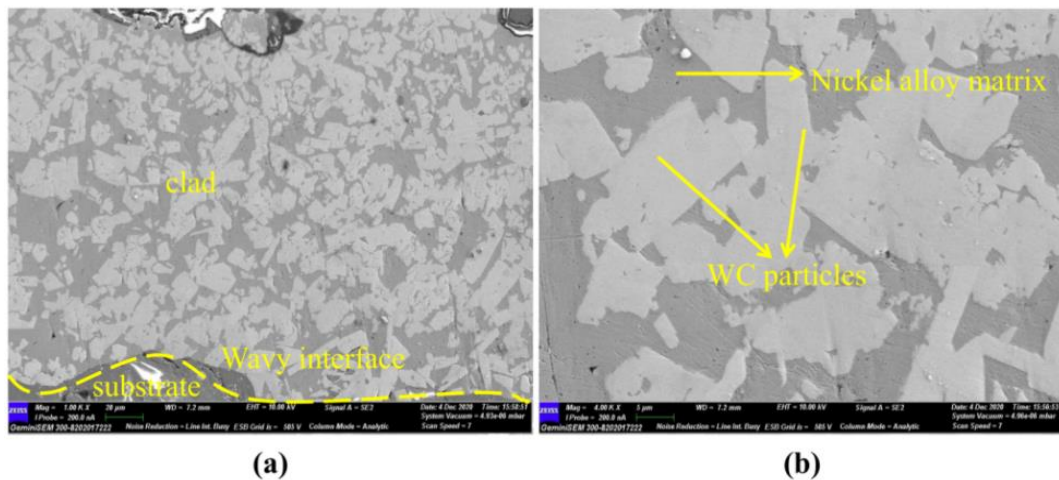


Figure 4. 17 (a) A typical cross-sectional FESEM image of NiCrSiB/WC microwave clad, (b) Top region of the clad at higher magnification.

#### 4.5.6 NiCrSiB/WC/Ag/BaF<sub>2</sub> MHH clad

Similarly, a cross-sectional image of solid lubricant encapsulated NiCrSiB/WC/Ag/BaF<sub>2</sub> clad is shown in Figure 4.20. The WC particles are well bonded with the nickel alloy matrix and uniformly distributed in the clad. In addition, the residual WC particles are responsible for the formation of hardness phases in the clad. Figure 4.20b shows the partial dissolution of WC particles in the NiCrSiB/WC/Ag/BaF<sub>2</sub> clad at the middle portion. This phenomenon could enhance the bonding between the matrix and reinforcement phase. The needle-shaped particles (Figure 4.20b) between WC (block-shaped particles) and nickel alloy matrix indicate intermetallic phases containing W-Ni-Cr. Due to the presence of Cr in the clad decomposition of W<sub>2</sub>C would occur and lead to precipitation of intermetallic carbides/borides (Liu et al. 2014). The deposition of residual WC particles near the

bottom mainly happens because of their higher melting point than the nickel alloy matrix.

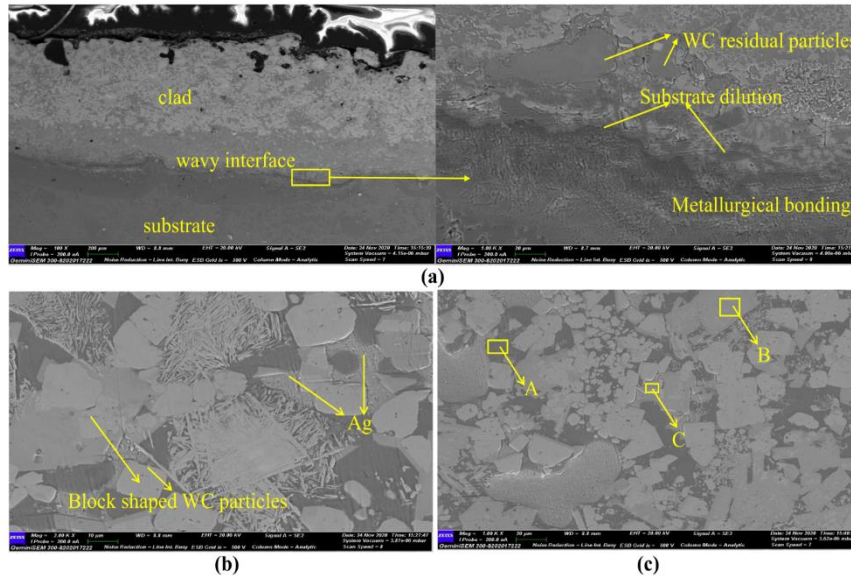


Figure 4. 18 (a) The cross-sectional morphology of NiCrSiB/WC/Ag/BaF<sub>2</sub> clad, (b) Bottom region (c) Top region.

Near to the top region (Figure 4.20c), comparatively smaller sized WC particles were observed. The dissolution of WC particles plays a vital role. The change in their appearance happens mainly because of the variation in a thermal gradient. Usually, the cooling rate and dilution ratio affect the strengthening phases. The EDS analysis is carried out to know the elemental composition of various phases. The matrix phase (Area A) confirmed that the phase mainly rich in Ni, Cr, Si, B (Figure 4.21a), and the block-sized particles (Area B) composed of W and C (Figure 4.21b), and the agglomerated phase in the clad (Area C) mainly composed of Ag (Figure 4.21c).

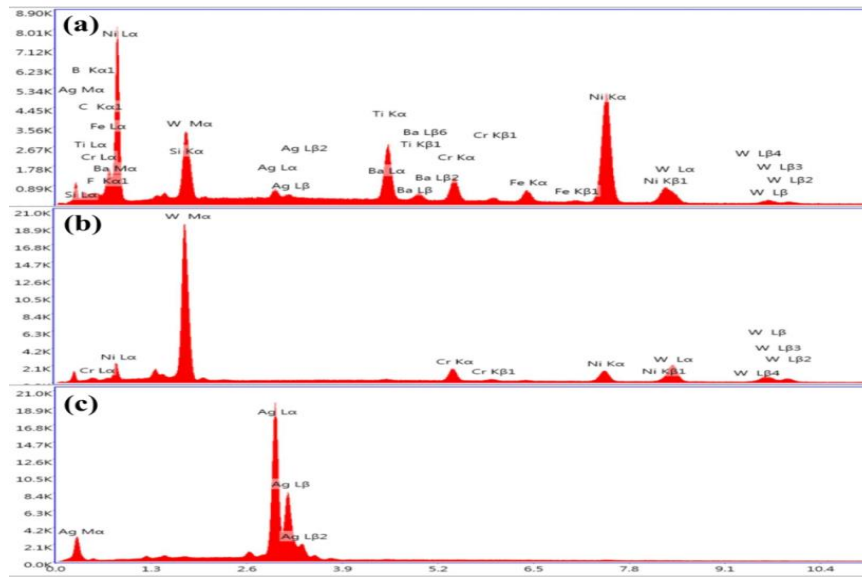


Figure 4. 19 EDS analysis of the NiCrSiB/WC/BaF<sub>2</sub> clad in the regions of Fig 4c. (a) region A, (b) region B, (c) Region C.

As shown in Figure 4.22, the elemental distribution of nickel alloy matrix (NiCrSiB), reinforcement (WC), and lubricating phases (Ag, BaF<sub>2</sub>) are well distributed in the clad.

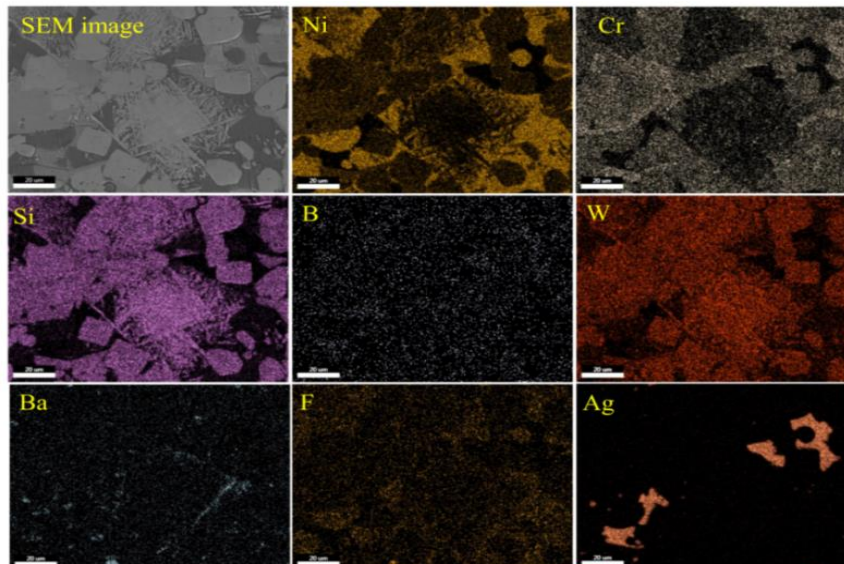


Figure 4. 20 EDS elemental distribution of various elements of NiCrSiB/WC/Ag/BaF<sub>2</sub> clad.

#### 4.5.7 NiCrSiB/WC/Ag/hBN and NiCrSiB/WC/MoS<sub>2</sub>/hBN MHH clads

Figure 4.24a shows the morphology of microwave heated NiCrSiB/WC/Ag/hBN clad. Due to the low thermal gradient, clads were obtained with uniform microstructure with no solidification-related defects. Figure 4.24b shows the magnified SEM image of the clad substrate interface. The microstructure of the clad has a dense matrix and was embedded with partially melted WC particles (Figure 4.24c). It was observed that the irregular WC particles were partially melted and induced the formation of intermetallic compounds (Figure 4.24d). Conventional heating techniques require prolonged heating time for processing of tungsten included clads. It has a detrimental effect on microstructure and leads to the reduction of mechanical properties. Due to the rapid processing technology, microwave cladding leads to minimal microstructural coarsening, thermal distortion and shows very good microstructural homogeneity. It can be seen that the clad was diluted with the titanium substrate and metallurgical bonded. Also, high convective currents in the melt pool indicate metallurgical bonding with the substrate. The thermal conductivity of the substrate also plays a vital role in dilution.

In order to study the distribution of solid lubricants and reinforcement in the clad, EDS elemental mapping was conducted. The elemental distribution of the NiCrSiB/WC/Ag/hBN clad is shown in Figure 4.25. Elemental maps of Ni, Cr, Si, W, Ag, B, N, Ti, and C were presented. It was inferred that the white blocky particles in the clad were mainly enriched with W and C. These tungsten carbide particles were well bonded with the nickel alloy matrix. The influence of volumetric heating leads to the formation of intermetallic phases. Cr element can be seen around the WC particles. Due to the melt immiscibility of WC and nickel alloy, separate phases and few intermetallic phases were formed during the solidification. The higher concentrations of Cr and C in the alloys are always beneficial for the better dissolution of hard phases.

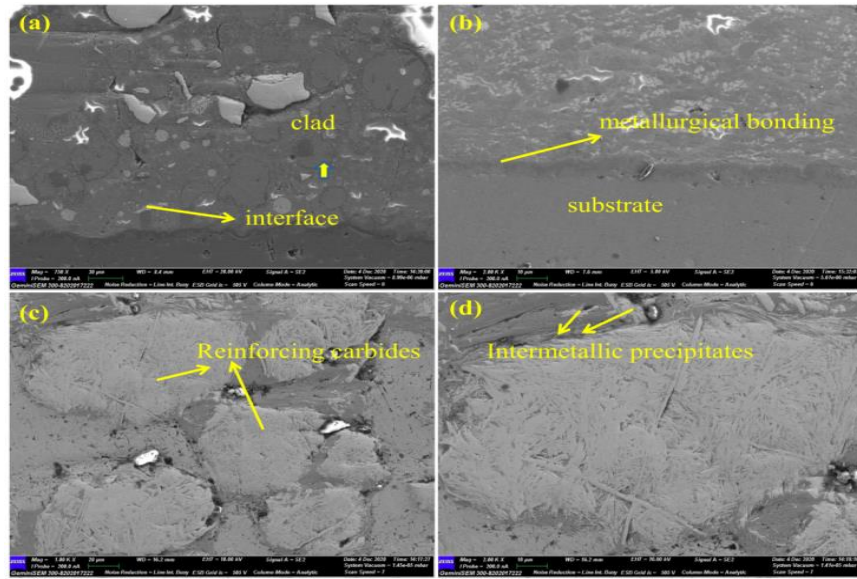


Figure 4. 21 Microstructure of the NiCrSiB/WC/Ag/hBN clad across the cross-section  
 (a) clad area, (b) interface area, (c) dispersion of WC particles in the nickel alloy matrix, and (d) WC dissolution.

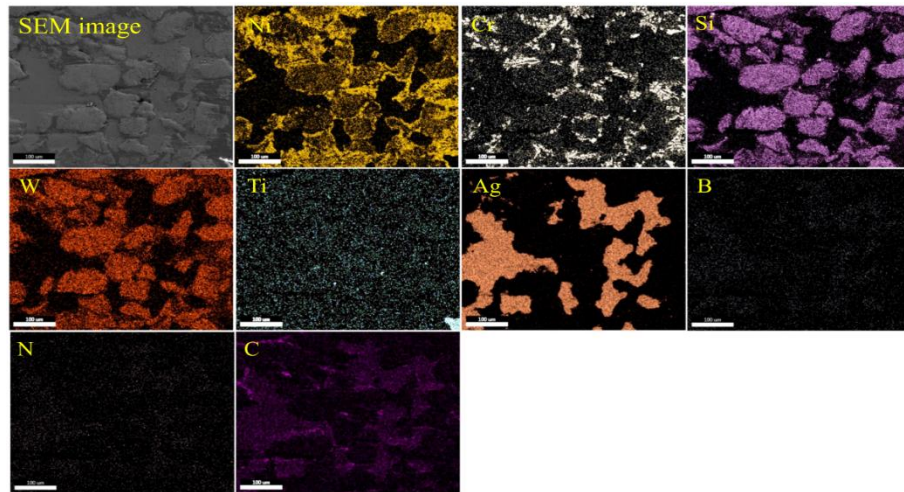


Figure 4. 22 EDS elemental mapping of NiCrSiB/WC/Ag/hBN clad across the cross-section.

Similarly, NiCrSiB/WC/MoS<sub>2</sub>/hBN (Figure 4.26a) showed a very good microstructure without any pores and defects. Generally, existing pores in the material expand with the temperature rise, and pores reduce with the subsequent cooling. However, in microwave hybrid heating, the existing pores will be filled with molten

material due to the volumetric heating leads to excellent microstructure. The dilution of the clad can be seen in Figure 4.26b. The irregular WC particles dissolution can be seen in Figure 4.26c, d. The EDS elemental maps of the clad can be seen in Figure 4.27. Matrix, reinforcement, and lubricant phases were well distributed in the cladding. The presence of titanium in the clad indicates the diffusion bonding.

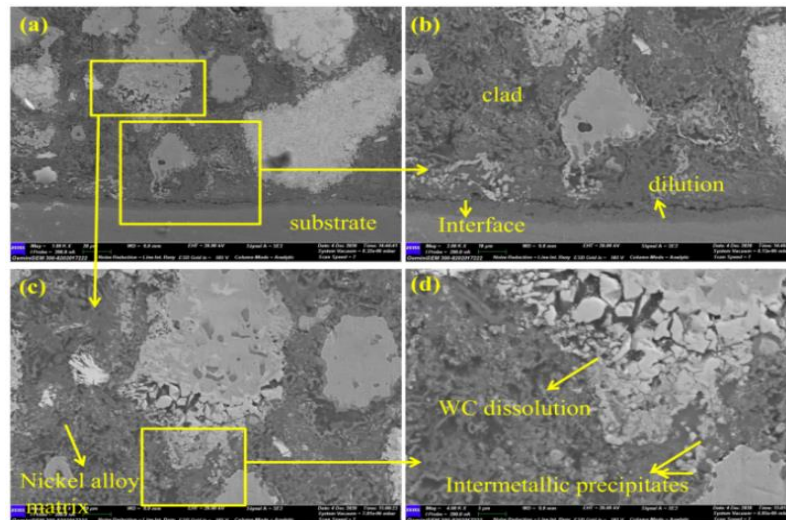


Figure 4. 23 Microstructure of the NiCrSiB/WC/MoS<sub>2</sub>/hBN clad across the cross-section (a) clad area, (b) interface area, (c) dispersion of WC particles in the nickel alloy matrix, and (d) WC dissolution.

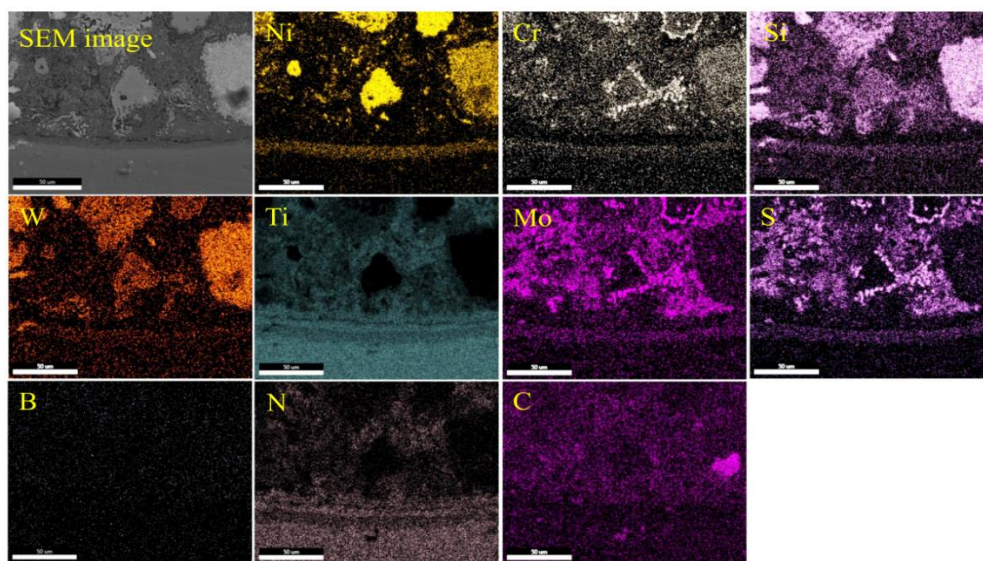


Figure 4. 24 EDS elemental mapping of NiCrSiB/WC/MoS<sub>2</sub>/hBN clad across the cross-section.

The distribution of solid lubricants was consistent with the nickel alloy matrix. Li et al. reported that silver can be formed as a solid solution and disperses at the nickel boundary in the matrix (Li et al. 2009). However, other solid lubricants like hBN and MoS<sub>2</sub> were fully dissolved in the cladding. The interaction of microwaves with the material depends mainly on their skin depth. Also, no micro and macro cracking were observed in the clad cross-section because of the volumetric heating. The dendritic phases, which sometimes lead to cracking, were not formed in the clad. The non-uniform dissolution of hard phases in the clad is always detrimental to the clad. Here, microwave cladding enhances the uniform embedment of hard phases. Also, the addition of solid lubricant phases in the clad alters the microstructure.

#### 4.5.8 NiCrSiB/WC/MoS<sub>2</sub>/BaF<sub>2</sub> MHH clad

Figure 4.29 shows the cross-sectional morphology of the NiCrSiB/WC/MoS<sub>2</sub>/BaF<sub>2</sub> MHH deposited clad layer. The thickness of the clad was noted as approximately 1±50mm. There were no cracks present in the clad. The metal-ceramic clad material can be easily melted through the microwave hybrid heating technique. The WC particles directly interact with the microwaves due to their higher skin depth. The heat conduction from WC particles further raises the temperature of surrounding nickel alloy particles. After reaching critical temperature, powder particles interact with the microwaves, leading to the clad's uniform melting.

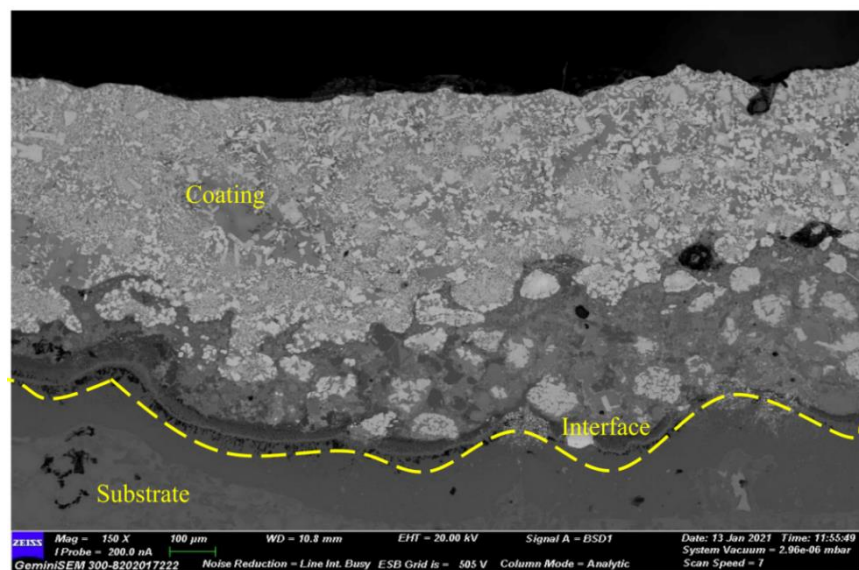


Figure 4. 25 The cross-sectional SEM image of MHH clad.

The observations were noted in a step of 5 minutes microwave exposure time. At 25 minutes, the microwave radiation was enough to melt the preplaced power layer, which further dissolves the thin layer of the substrate material. Thus, the clad layer was partially diffused with the titanium substrate (Figure 4.30a). The dilution of the substrate with the clad can be seen in Figure 4.30b. The inverse thermal gradient was a significant phenomenon in microwave heating. The wavy line in the interface was mainly due to localized convective currents in the clad layer. It was observed that partially dissolved WC particles in the nickel alloy matrix were well distributed. Comparatively, few micropores can be observed in TIG clad than MHH clad.

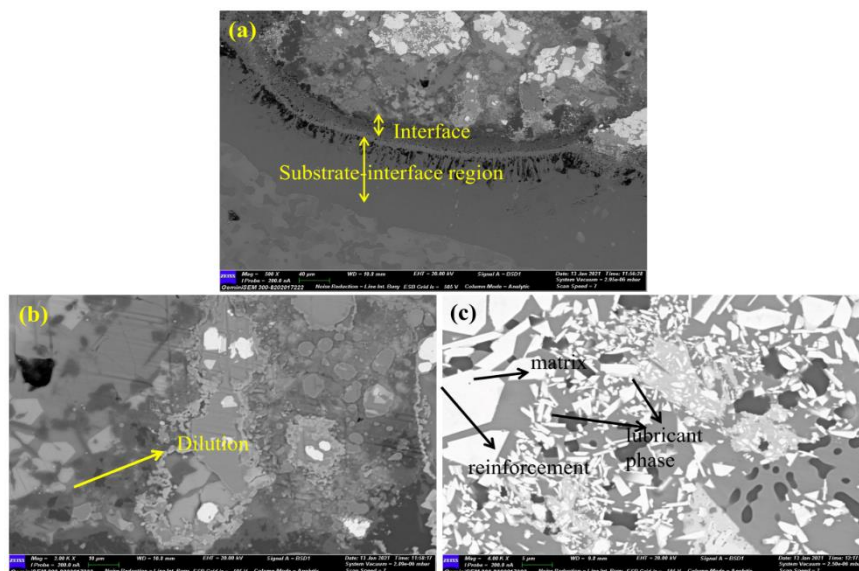


Figure 4. 26 SEM image of MHH clad (a) clad-interface region (b) just above the interface region (c) top region of the clad.

The lubricant phase was well distributed on the top region of the clad (Figure 4.30c). The EDS analysis shows the possible intermetallic phases in the clad layer (Figure 4.31). The EDS study confirmed that mark A in Figure 4.31a has been identified as nickel alloy matrix (Figure 4.31b). The white blocky particles (mark B) were rich in W and C (Figure 4.31c).



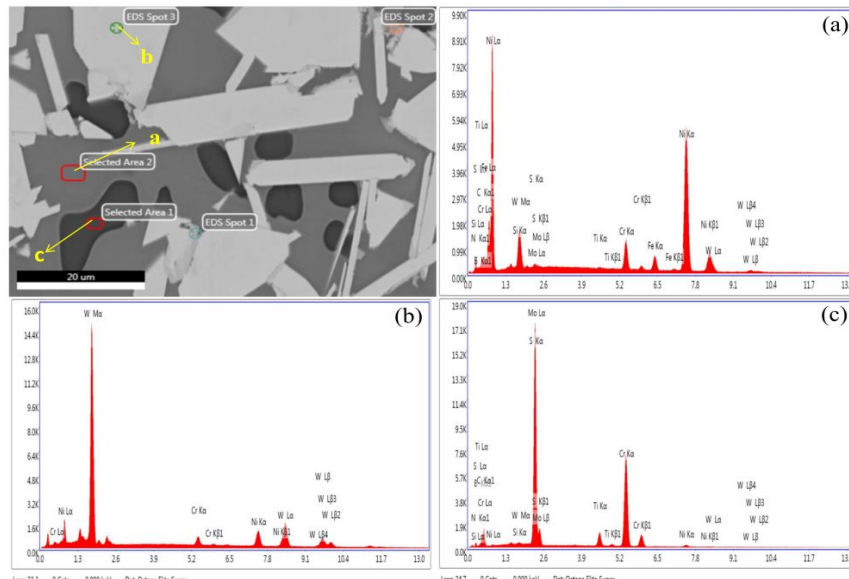


Figure 4. 27 EDS analysis of MHH clad across the cross section (a) region A (b) region B (c) region C.

The dark-shaded particles (mark C) were mainly composed of Mo and S (Figure 4.31d). EDS mapping is conducted to identify the elemental distribution in the clad layer (Figure 4.32). It can be evident that nickel alloy matrix, WC reinforcement phase, and lubricant phase containing Ba, F, Mo, and S were very well dispersed in the clad. Due to the substrate dilution effect, Ti element can be observed in the EDS mapping.

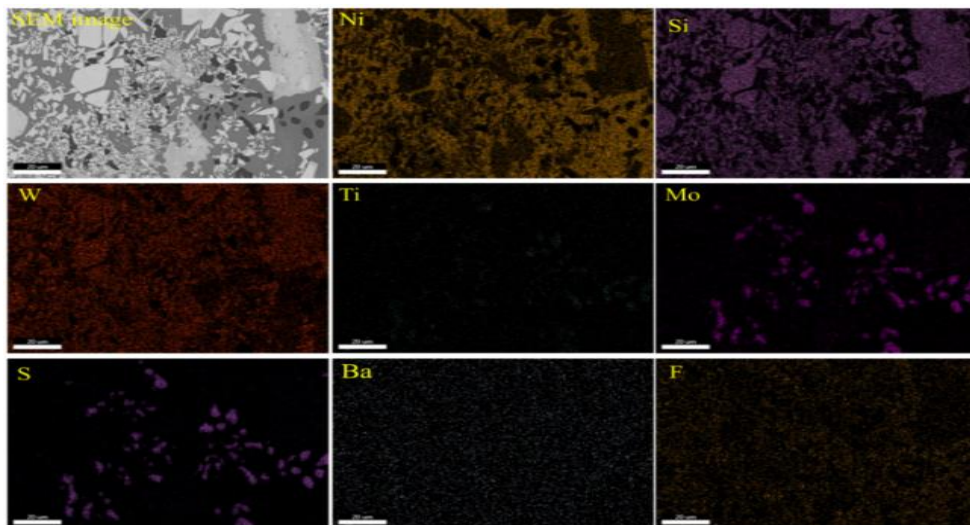


Figure 4. 28 EDS mapping of MHH clad across the cross section.

## 4.6 Phase analysis of the clads

### 4.6.1 XRD analysis of the NiCrSiB/WC and NiCrSiB/WC/Ag/BaF<sub>2</sub> TIG clads

Figure 4.33 shows the XRD patterns of the TIG claddings NiCrSiB/WC and NiCrSiB/WC/Ag/BaF<sub>2</sub> processed at 70 A. It was evident that the coatings primarily consisted of Ni, Cr<sub>23</sub>C<sub>6</sub>, Cr<sub>7</sub>Ni<sub>3</sub>, WC, W<sub>2</sub>C, and NiTi. Oxides were absent in the coatings because of the primary and secondary shielding argon protection achieved during the process of fabrication. WC dissolution was observed in the coating due to the higher heat input, resulting in the formation of W<sub>2</sub>C. The coating was mixed with titanium due to the higher energy input, which caused the formation of the intermetallic NiTi compound. The presence of Ag indicates the synergistic lubrication effect in the coating.

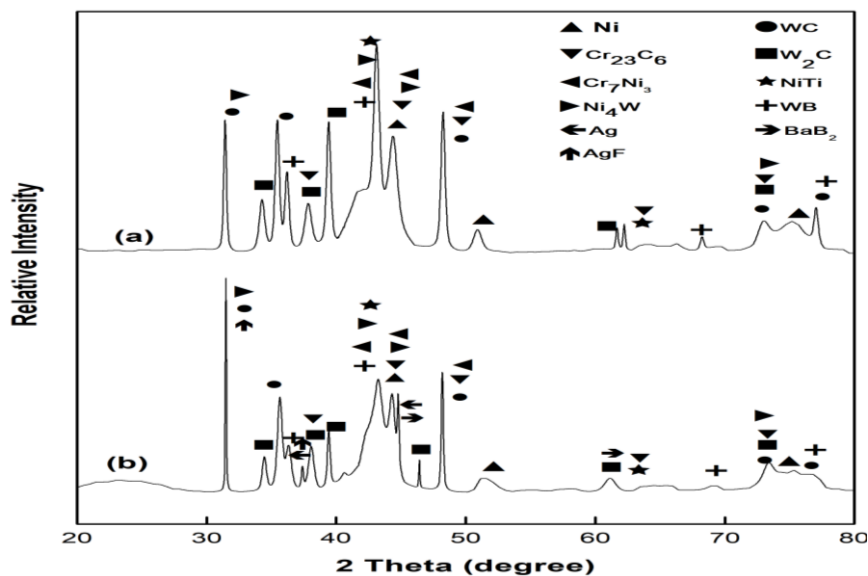


Figure 4. 29 XRD patterns of the coatings at processing current 70A (a) NiCrSiB/WC clad (b) NiCrSiB/WC/Ag/BaF<sub>2</sub> clad.

### 4.6.2 XRD analysis of the NiCrSiB/WC/Ag/hBN and NiCrSiB/WC/MoS<sub>2</sub>/hBN TIG clads

Figure 4.34 shows the XRD patterns of NiCrSiB/WC/Ag/hBN and NiCrSiB/WC/MoS<sub>2</sub>/hBN TIG composite clads. It can be evident from the results that both composite coatings mainly consist of Ni, W<sub>2</sub>C, Cr<sub>23</sub>C<sub>6</sub>, NiTi. The formation of

intermetallic phase NiTi in the analysis indicates the dilution of titanium substrate. The presence of  $W_2C$  in the present study indicates the decomposition of WC because of high input in the TIG process. As  $MoS_2$  is very sensitive to the operating temperature, it was decomposed and formed as  $Mo_2S_3$ .

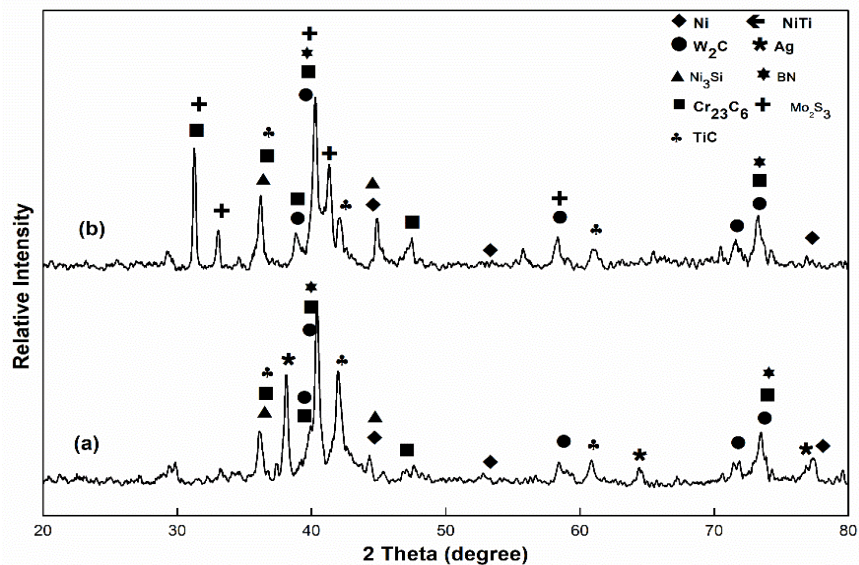


Figure 4.30 XRD patterns of the clads developed at 90 A (a) NiCrSiB/WC/Ag/hBN clad (b) NiCrSiB/WC/ $MoS_2$ /hBN clad.

#### 4.6.3 XRD analysis of the NiCrSiB/WC/ and NiCrSiB/WC/ Ag/BaF<sub>2</sub> MHH clads

Figure 4.35 shows the XRD pattern of NiCrSiB/WC, and NiCrSiB/WC/Ag/BaF<sub>2</sub> MHH clads. The typical phases of Ni, WC,  $Cr_{23}C_6$ , and  $Cr_3Si$  are dominant in the clad. The dissolution of WC in the clad leads to the formation of hard phases  $W_2C$  and  $Cr_{23}C_6$ . The lubricant phases such as Ag and  $Ag_2F$  are observed on the NiCrSiB/WC/Ag/BaF<sub>2</sub> clad. Due to the diffusion bonding of titanium with the clad, the intermetallic phase NiTi was observed in both clads.

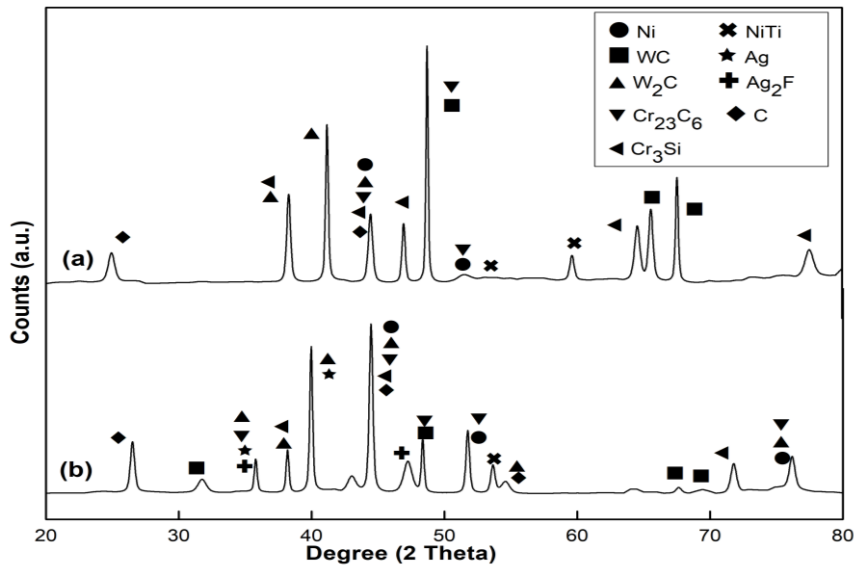


Figure 4. 31 X-ray diffraction patterns of MHH clad (a) NiCrSiB/WC (b) NiCrSiB/WC/Ag/BaF<sub>2</sub>.

#### 4.6.4 XRD analysis of the NiCrSiB/WC/Ag/hBN and NiCrSiB/WC/MoS<sub>2</sub>/hBN MHH clads

The XRD patterns of the NiCrSiB/WC/Ag/hBN and NiCrSiB/WC/MoS<sub>2</sub>/hBN MHH clads are shown in Figure 4.36. The results manifest that both clad were mainly composed of Ni, Cr<sub>23</sub>C<sub>6</sub>, WC, W<sub>2</sub>C, Ni<sub>3</sub>Ti. In addition, the lubricant phases Ag, BN in NiCrSiB/WC/Ag/hBN clad, Mo<sub>2</sub>S<sub>3</sub> in NiCrSiB/WC/MoS<sub>2</sub>/hBN clad were identified. The formation of the Ni<sub>3</sub>Ti intermetallic phase in the clad could be attributed to the strong metallurgical bonding with the substrate. The peaks corresponding to the W<sub>2</sub>C phase in both clads indicate the decarburization of WC.

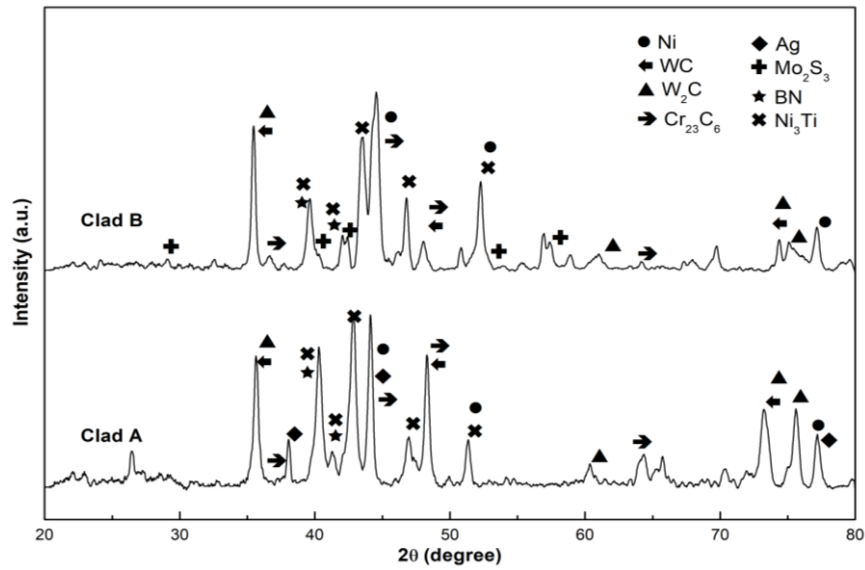


Figure 4. 32 XRD patterns of NiCrSiB/WC/Ag/hBN (clad A) and NiCrSiB/WC/MoS<sub>2</sub>/hBN (clad B) clads.

#### 4.6.5 XRD analysis of the NiCrSiB/WC/MoS<sub>2</sub>/BaF<sub>2</sub> clads processed by TIG and MHH techniques

Figure 4.37 shows the XRD analysis of NiCrSiB/WC/MoS<sub>2</sub>/BaF<sub>2</sub> clads deposited by TIG and MHH technique. The XRD patterns of both TIG and MHH treated clad show a similar sequence of peak formation. The phases TiC and Ti<sub>2</sub>Ni formed in the TIG cladding might be because of the dilution of the substrate material in the clad. Due to the higher energy input in the clad, WC particles were dissolved and formed as W<sub>2</sub>C. The TIG and MHH treated clads have typical Ni, W<sub>2</sub>C, Cr<sub>23</sub>C<sub>6</sub>, TiC, Ti<sub>2</sub>Ni, Mo, BaF<sub>2</sub>. The Ti<sub>2</sub>Ni phase in the MHH clad indicates the diffusion of substrate material in the clad.

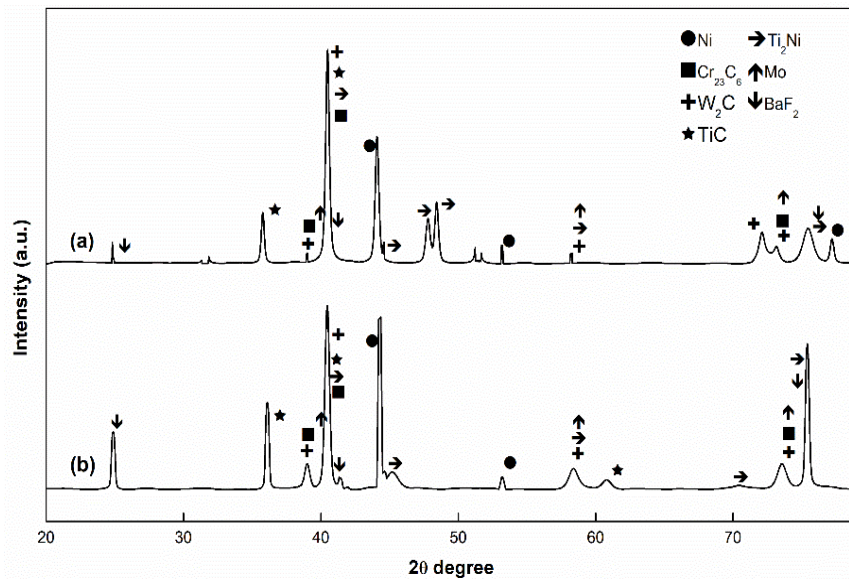


Figure 4. 33 X-ray diffraction pattern of NiCrSiB/WC/MoS<sub>2</sub>/BaF<sub>2</sub> clads deposited by (a) TIG cladding (90A) (b) MHH cladding.

## 4.7 High temperature tribological performance of coatings

### 4.7.1 NiCrSiB/WC and NiCrSiB/WC/Ag/BaF<sub>2</sub> TIG claddings

The tribological performance of the coatings was evaluated by pin on disc tribometer under dry sliding conditions. The properties related to tribological performance are not intrinsic but are reliant on many factors such as load, temperature, atmospheric conditions, and sliding speed etc. The TIG clad samples performed at 70A processing current are taken into consideration to investigate the effect of temperature and load on the tribological performance. Figure 4.38 exhibits the weight loss of NiCrSiB/WC clad and NiCrSiB/WC/Ag/BaF<sub>2</sub> samples tested under the load of 20N and 40N at temperatures 200°C, 400°C and 600°C. In the sliding wear operation, tribo-chemical interactions of coating with the counter body, operating environment occur. These induce local temperatures and shear stresses along the contact zones. As shown in bar chart, weight loss of the NiCrSiB/WC clad samples raises from 17mg to 25mg at 200°C by varying loads from 20N to 40N. The increment of load to 40N leads to more material removal against counter body. Whereas, weight loss increases from 6 mg to 11 mg for NiCrSiB/WC/Ag/BaF<sub>2</sub> clad with increase of load from 20N to 40N at 200°C testing temperatures. The weight loss of the NiCrSiB/WC/Ag/BaF<sub>2</sub> clad

samples was decreased with the increase of temperature from 200°C to 600°C. This is attributed to the formation of tribo layer formation on the coating surface. It is observed that more weight loss occurred at 400°C, 40N for NiCrSiB/WC clad. Whereas, NiCrSiB/WC/Ag/BaF<sub>2</sub> clad showed more weight loss at 200°C, 40N load. However, NiCrSiB/WC/Ag/BaF<sub>2</sub> clad performed very well at both lower (200°C) and higher (600°C) testing temperatures. At 600°C, both solid lubricants Ag and BaF<sub>2</sub> are remain active and further reduced the weight loss to 4mg at 20N load.

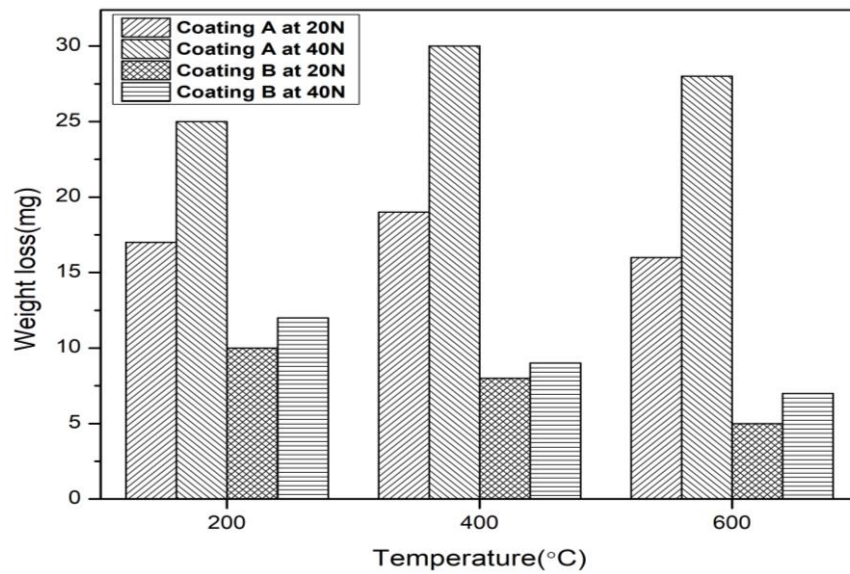


Figure 4. 34 Variation of weight loss of the NiCrSiB/WC clad and NiCrSiB/WC/Ag/BaF<sub>2</sub> clad at different test temperatures and loads.

Several factors create uncertainty in wear properties such as 20 porosity, partially melted particles, wear debris and polished sample surface etc. No significant change was observed in weight loss and friction coefficient at 20N loads. Figure 4.39 shows the friction coefficients of Titanium 31 substrate, NiCrSiB/WC clad, and NiCrSiB/WC/Ag/BaF<sub>2</sub> clad at 200°C, and 600°C. The reduction of relative humidity due to the temperature rise on the contact areas causes low friction coefficient at the starting of test. It can be seen from that the average friction coefficient of NiCrSiB/WC clad is more compared to titanium 31 substrate and NiCrSiB/WC/Ag/BaF<sub>2</sub> clad. The high ceramic inclusion is detrimental to friction coefficient. The solid lubricants addition was beneficial to reduce the material loss and friction coefficient. The NiCrSiB/WC/Ag/BaF<sub>2</sub> clad friction coefficient is found in

the range of 0.439-0.291. It is observed that the friction coefficient reduced significantly as increasing the temperature, which might be due to the tribo layer formation. The use of Ag solid lubricant in the coating led to low friction at starting stages of the test. The high temperature solid lubricant BaF<sub>2</sub> was reduced friction as well as weight loss at 600°C. The friction coefficient of NiCrSiB/WC clad decreases (0.462 to 0.531) with the rising temperature from 200°C to 600°C. The wear rate variation of the coatings has high uncertainty, which depends on several factors such as defects, wear debris on the track and surface roughness etc. These can usually affect the wear rate calculation. The minimum wear rate was occurred for NiCrSiB/WC/Ag/BaF<sub>2</sub> clad is  $2.27 \times 10^{-3}$  mm<sup>3</sup>/N-m 20N, 600°C. The maximum wear rate observed for NiCrSiB/WC clad is  $6.92 \times 10^{-3}$  mm<sup>3</sup>/N-m at 40N, 600°C. Moreover, when compared with the weight loss and wear rate for NiCrSiB/WC clad, NiCrSiB/WC/Ag/BaF<sub>2</sub> clad shows superior wear performance, indicating its higher effective lubricant film formation.

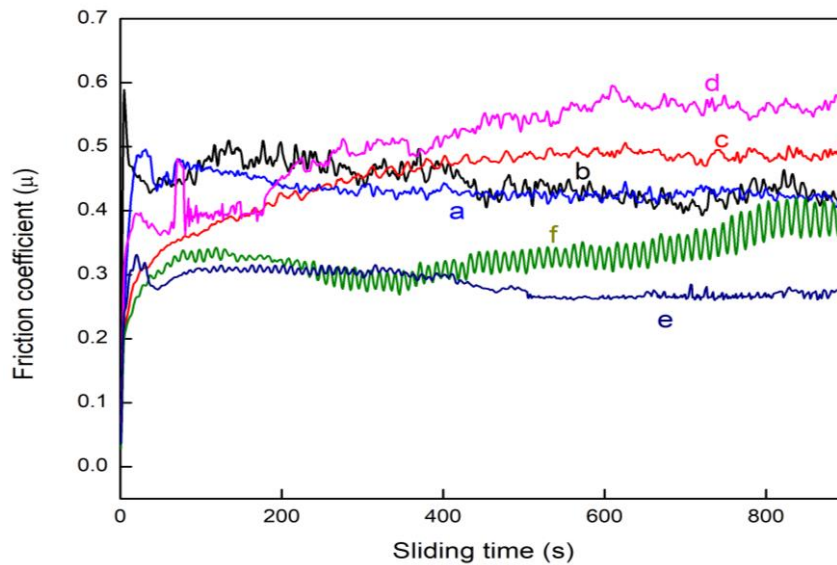


Figure 4.35 Friction coefficient of the coatings with respect to sliding time (a) Titanium 31 substrate at 200 °C (b) Titanium 31 substrate at 600 °C (c) NiCrSiB/WC clad at 200 °C (d) NiCrSiB/WC clad at 600 °C (e) NiCrSiB/WC/Ag/BaF<sub>2</sub> clad at 200°C (f) NiCrSiB/WC/Ag/BaF<sub>2</sub> clad at 600 °C.

Figure 4.40 depicts the worn surfaces of NiCrSiB/WC clad and NiCrSiB/WC/Ag/BaF<sub>2</sub> clad under the load of 20N at different test temperatures.



There is more delamination was observed for NiCrSiB/WC clad at 600°C. In the sliding wear operation, normal and shear stresses stimulate micro bulges on the surface to fracture. The removal of material takes place after the crack reaches critical length. In Figure 4.40 a, b and c the WC particles were pulled out due to abrasion against the alumina disc. This wear regime mainly happened due to the surface fatigue causing plastic shearing against the counter body. The oxide formation on the NiCrSiB/WC clad was useful to reduce the delamination at 600°C. In the NiCrSiB/WC/Ag/BaF<sub>2</sub> clad, deformation of the layer was observed at lower temperatures. The solid lubricant Ag can be effective and forms lubricity up to 400°C. BaF<sub>2</sub> can be able to provide lubricity above 450°C.

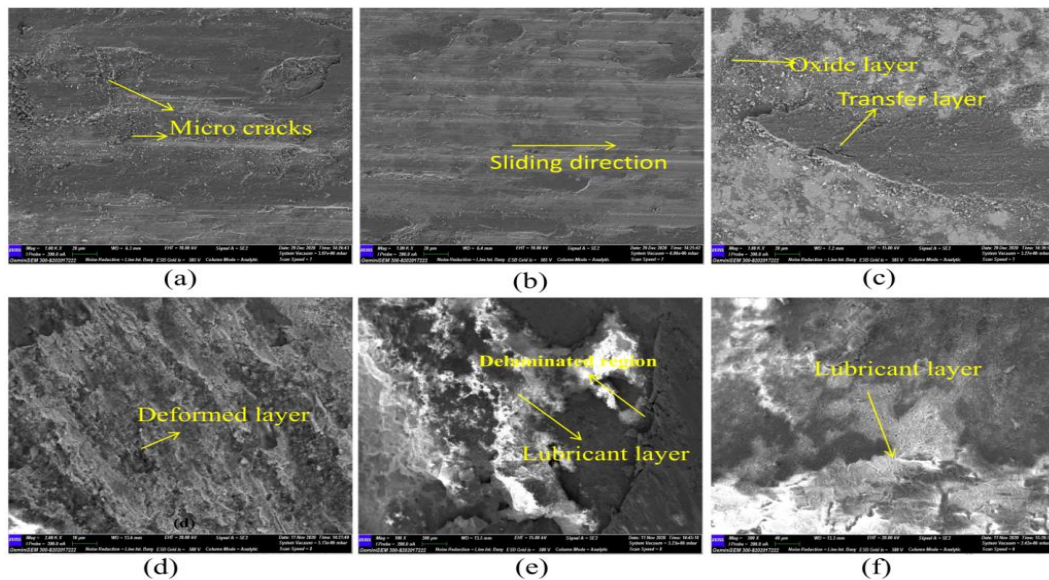


Figure 4. 36 SEM images of wear scars under 20N load (a) NiCrSiB/WC clad at 200°C; (b) 400°C; (c) 600°C; (d) NiCrSiB/WC/Ag/BaF<sub>2</sub> clad at 200°C; (e) 400°C; (f) 600°C.

From Figure 4.41a, b and c, it can be observed that deeper grooves and deformation of the coating occurred. At higher loads, the pull-out debris particles from the counter body may be acted as third bodies and causing deeper grooves and scratches. There was apparent damage was observed at 40N load. The Ag forms lubricant layer at these test temperatures but the lubricity was not protective enough to control coating delamination against higher loading conditions (40 N). As test temperature increases, delamination of the coating reduced as shown in Figure 4.41d, e, and f. At 200 °C, the

elements Ag, O few amounts of F are observed on the surface by EDX elemental mapping (shown in Figure 4.42). It reveals Ba element is ineffective in this temperature range. The formation of Ag lubricant layer, intermetallic phases Ni<sub>4</sub>W, NiTi and other oxide phases were beneficial against deep scratches and grooving. The EDX elemental mapping of NiCrSiB/WC/Ag/BaF<sub>2</sub> clad worn surface at 600°C is shown Figure 4.43. It can be seen that high amount of Ba, F are observed on the worn surface. At 400°C-600°C temperature range, BaF<sub>2</sub> is effective and provided lubricity and few amount of Ag phase remained as effective. Overall, the incorporation of this solid lubricant combination in the coating was beneficial to reduce wear at both low and high temperatures. The solid lubricants Ag, and eutectic BaF<sub>2</sub>/CaF<sub>2</sub> can be easily distributed on the worn surface at higher temperatures (600°C-800°C). The main lubricant factors in the wear mechanism are plastic deformability of Ag and brittle-ductile transition of BaF<sub>2</sub>. It is evident that the wear mechanism was due to adhesive wear and transfer layer break down. At lower temperatures, wear mechanism of NiCrSiB/WC clad was mainly occurred due to combined adhesive-abrasive wear action and spalling. It has been observed that the lubricity obtained from NiCrSiB/WC/Ag/BaF<sub>2</sub> clad at 600°C is more protective against the breakdown of the transfer layer.

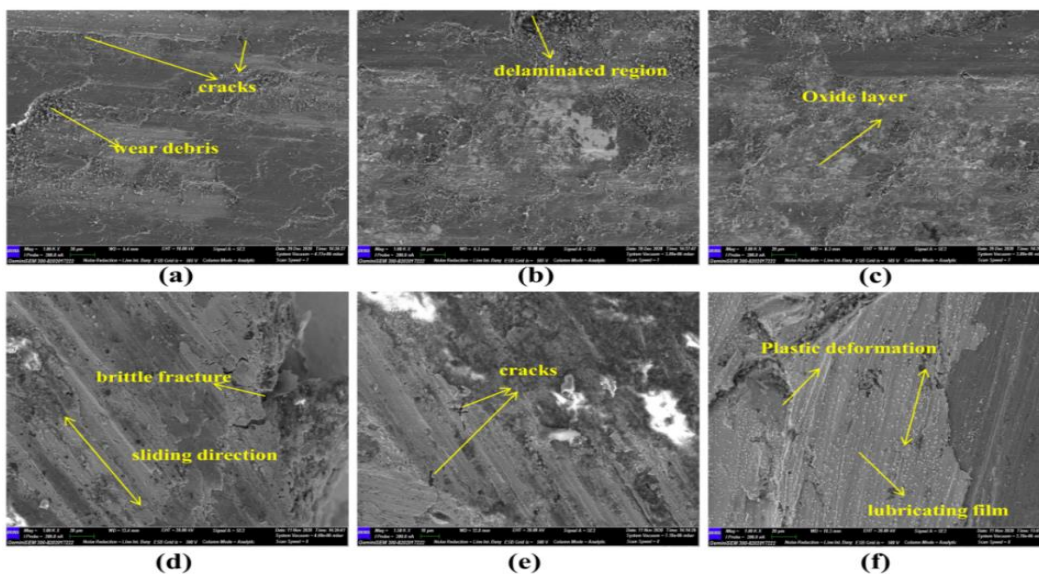


Figure 4. 37 SEM images of wear scars under 40N load (a) NiCrSiB/WC clad at 200°C; (b) 400°C; (c) 600°C; (d) NiCrSiB/WC/Ag/BaF<sub>2</sub> clad at 200°C; (e) 400°C; (f) 600°C.

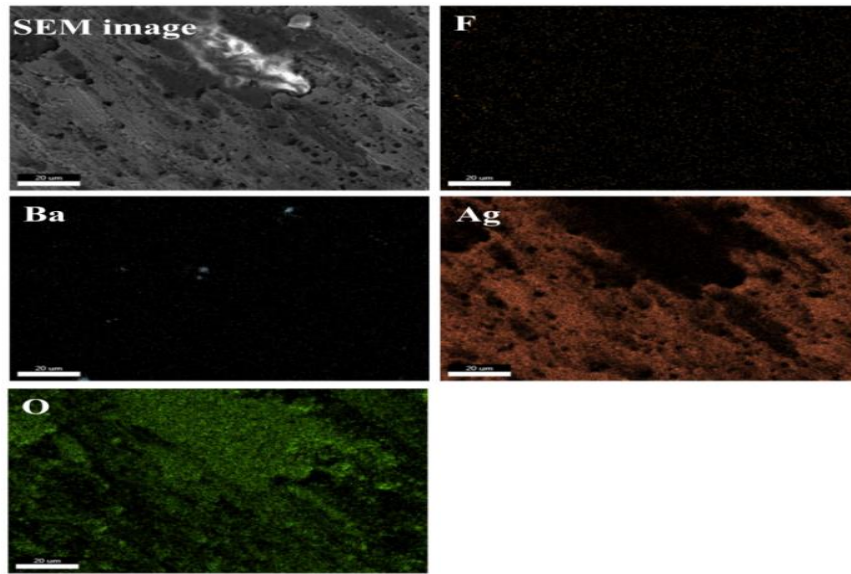


Figure 4. 38 EDX Elemental mapping of worn surface of NiCrSiB/WC/Ag/BaF<sub>2</sub> clad at 200°C, 20N loading condition.

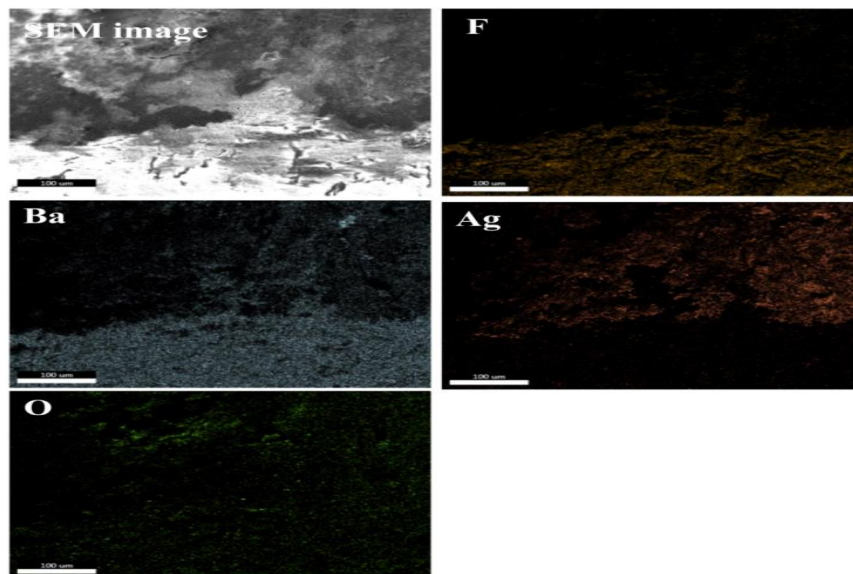


Figure 4. 39 EDX Elemental mapping of worn surface of NiCrSiB/WC/Ag/BaF<sub>2</sub> clad at 600°C, 20N loading condition.

Figure 4.44 exhibits the phase analysis of the worn surface of NiCrSiB/WC clad at 200 °C and 600 °C. The XRD technique was used to analyze the samples. The intensity of the peaks was higher for the worn surface of the coating, which can be

attributed to frictional heating and high temperature (Aristizabal et al. 2012). The oxides formed on the worn surface were NiO, TiO, Ni<sub>3</sub>Ti<sub>3</sub>O, and W<sub>3</sub>O. Their peak intensity increased with increasing temperature. These oxides can reduce the metal-to-metal contact, which reduces the shear strength of the contact surface. The phase analysis of NiCrSiB/WC/Ag/BaF<sub>2</sub> clad is shown in Figure 4.45. The diffraction peaks corresponding to Ag<sub>2</sub>F and Ba (TiO<sub>3</sub>) were observed on the worn surface of NiCrSiB/WC/Ag/BaF<sub>2</sub> clad. The sintering reactions and other oxidation properties were stronger at 600 °C. It led to the formation of a favorable glaze layer on the worn surface. The silver phases formed as a continuous lubricating film on the worn surface and mitigated the wear rate and coefficient of friction at both low and high temperatures. Barium titanium oxide (Ba (TiO<sub>3</sub>)) acted as an effective lubricant at high temperatures (600 °C). It could protect the coating from wearing out and helped in attaining a significantly low coefficient of friction (Mao et al. 2018). To sum up, the tribo chemical reactions involving the solid lubricants and oxides on the worn surface of NiCrSiB/WC/Ag/BaF<sub>2</sub> clad were more efficient in resisting wear than the reactions occurring on the surface of NiCrSiB/WC clad at elevated temperatures.

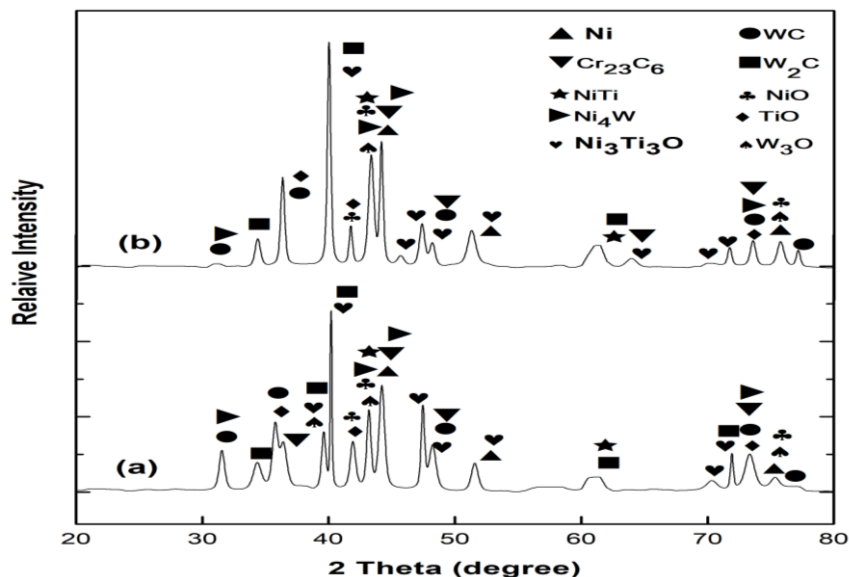


Figure 4. 40 XRD Patterns of worn surfaces of the NiCrSiB/WC clad at (a) 600°C (b) 200°C.

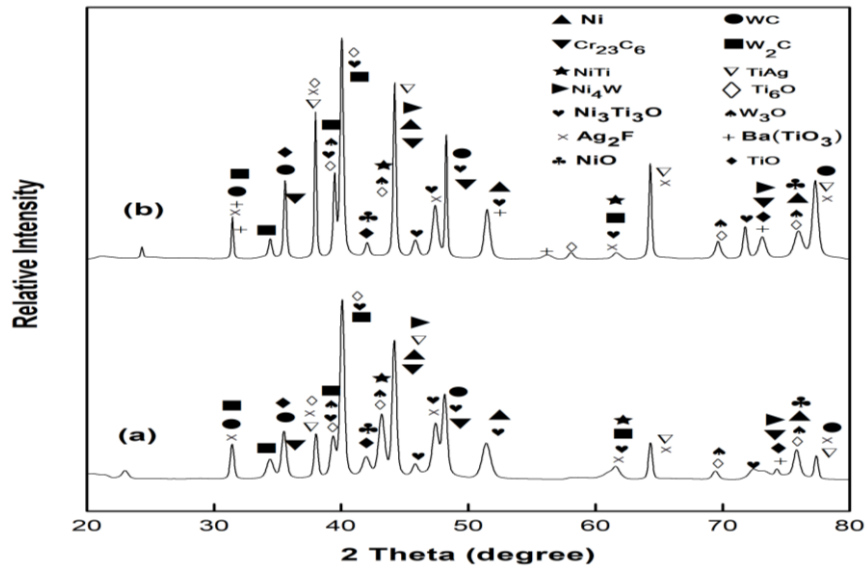


Figure 4. 41 XRD Patterns of worn surfaces of the NiCrSiB/WC/Ag/BaF<sub>2</sub> clad at (a) 200°C (b) 600°C.

#### 4.7.2 NiCrSiB/WC and NiCrSiB/WC/Ag/BaF<sub>2</sub> MHH claddings

The wear loss of the clad samples varied with the change in load and their operating temperatures. The bar chart (Figure 4.46) shows the wear rate of both clads performed at different test temperatures. It can be observed that the wear rate of NiCrSiB/WC clad is higher compared to NiCrSiB/WC/Ag/BaF<sub>2</sub> clad at both lower and higher test temperatures. The variation of friction coefficient of both clad at different temperatures is shown in Figure 4.47. The test temperature plays a vital role in friction properties. At higher temperatures, the friction coefficient turned smoother and decreased to some extent. At starting stages of the test, NiCrSiB/WC clad showed a higher friction coefficient. The higher WC content in the clad has a detrimental effect on the friction coefficient. The higher frictional forces generated at 20N load are mainly influenced by the debonded WC particles. The steady-state friction coefficient of NiCrSiB/WC clad at 200°C and 600°C under 10N load are 0.42 and 0.38.

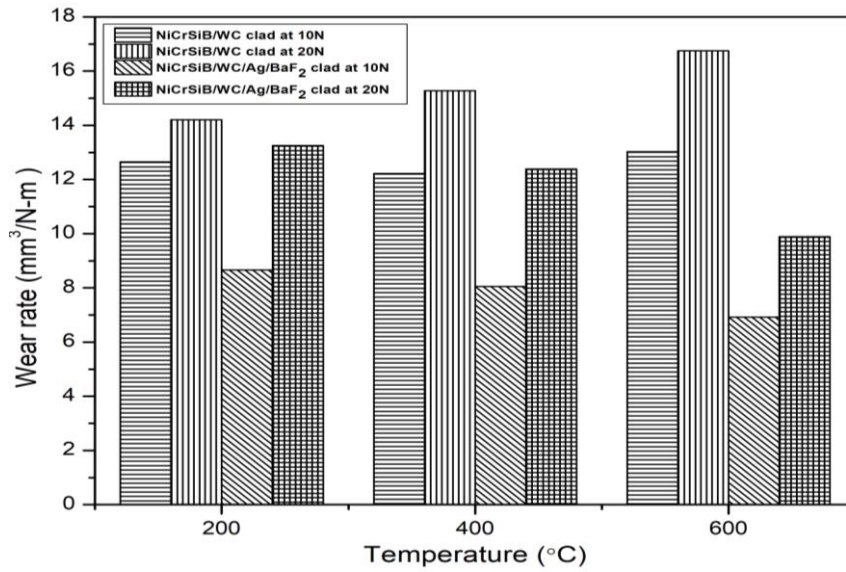


Figure 4. 42 Variation of wear rate of both clads at various temperatures and loads.

Similarly, the steady state friction coefficient of NiCrSiB/WC/Ag/BaF<sub>2</sub> clad at 200°C and 600°C under 10N load are 0.28 and 0.21. Ag and BaF<sub>2</sub> lubricants can be easily distributed on the clad surface at higher temperatures and reduce friction coefficient. The reduction of friction coefficient indicates the smooth glaze layer on the surface. It is clear from the results that the material debonding was prevented due to the smooth lubricant layer formation. This glaze layer further reduces the deep grooving and delamination against the counterbody. Also, the wear rate of NiCrSiB/WC clad reached higher compared to the NiCrSiB/WC/Ag/BaF<sub>2</sub> clad. At 200°C, NiCrSiB/WC clad showed a higher wear rate of  $14.20 \times 10^{-3} \text{ mm}^3/\text{N-m}$  under 20N load. As increasing temperature from 200°C to 600°C, the wear rate reduced to  $13.02 \times 10^{-3} \text{ mm}^3/\text{N-m}$  because of the oxide layer formation. Similarly, solid lubricant encapsulated clad (NiCrSiB/WC/Ag/BaF<sub>2</sub>) showed a higher wear rate ( $13.25 \times 10^{-3} \text{ mm}^3/\text{N-m}$ ) at 200°C, 20N load. The lubricant phase formed on the clad surface is not protective enough to reduce delamination. However, the wear rate of NiCrSiB/WC/Ag/BaF<sub>2</sub> clad is substantially decreased to  $6.92 \times 10^{-3} \text{ mm}^3/\text{N-m}$  at 600°C under 10N load.

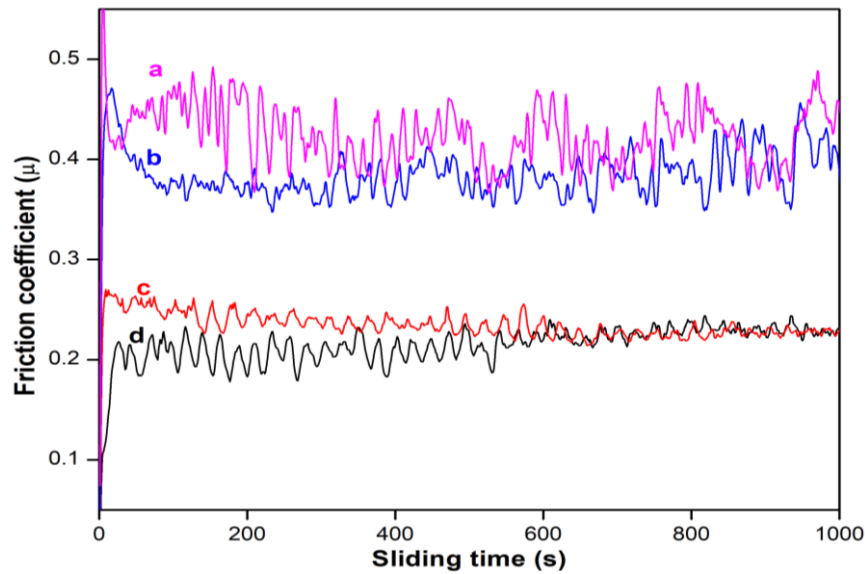


Figure 4. 43 Variation in friction coefficient with respect to sliding time for NiCrSiB/WC clad **(a)** 200°C **(b)** 600°C **(c)** NiCrSiB/WC/Ag/BaF<sub>2</sub> clad at 200°C **(d)** 600°C.

The worn surface morphology of the NiCrSiB/WC/Ag/BaF<sub>2</sub> clad at various temperature and loads are shown in Figure 4.48. There are groves, and cracks observed on the surface. The plastic deformability of silver is the main lubricant factor in the clad at 200 °C. It is beneficial to protect the clad surface against delamination. However, the lubricity of the silver is not sufficient at higher loads (20 N). With the increase in temperature, smooth glaze layer formed on the surface due to the combined effect of Ag and BaF<sub>2</sub> lubricant phases. As increasing temperature from 200 °C to 600 °C, the formed BaF<sub>2</sub> lubricant phase causes the brittle-ductile transition on the clad surface. This lubricant layer is favourable enough against deep grooves, fracture, and delamination of the surface (Figure 4.48 d-e).

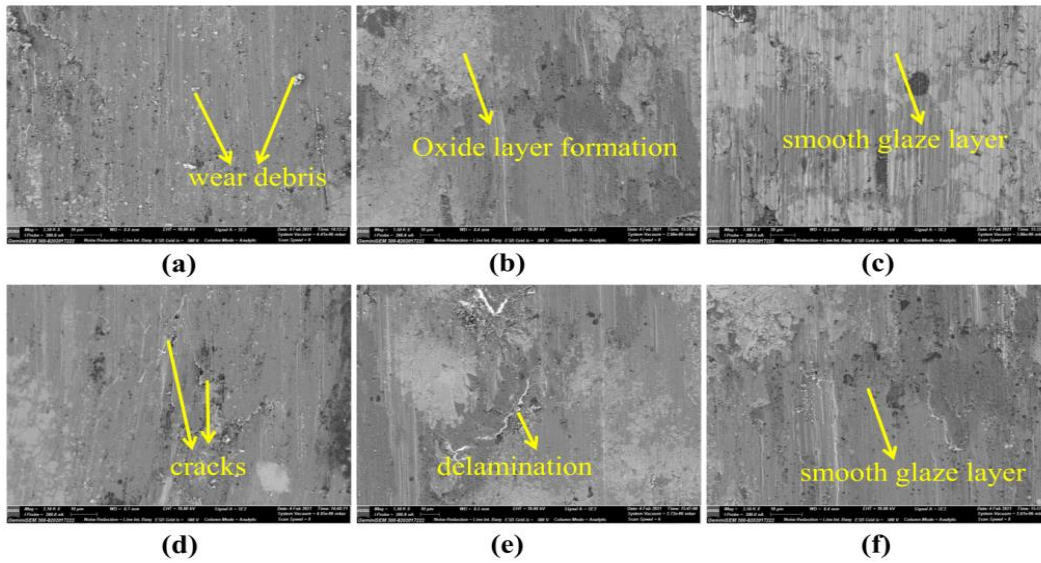


Figure 4. 44 The SEM images of NiCrSiB/WC/Ag/BaF<sub>2</sub> worn surfaces under 10N load: (a) 200°C, (b) 400°C, (c) 600°C; Under 20N load: (d) 200°C, (e) 400°C, (f) 600°C.

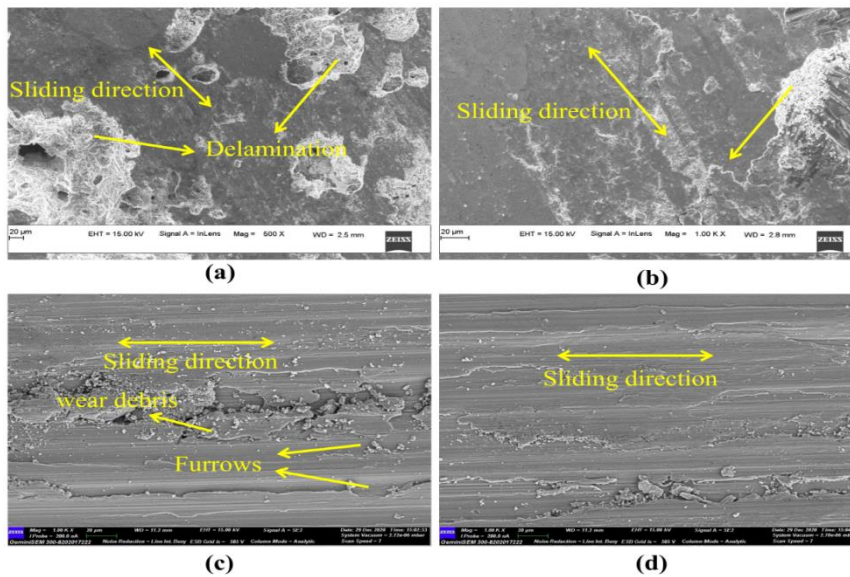


Figure 4. 45 The SEM images of the worn surface at 20N load: NiCrSiB/WC at (a) 200°C, (b) 600°C; Titanium 31 substrate at (c) 200°C, (d) 600°C.

Similarly, the worn surface morphology of the NiCrSiB/WC clad is shown in Figure 4.49. As shown in Figure 4.49a, more material removal is observed and can be seen as pits and delamination on the surface at 200°C. Due to the frictional heating



and higher operating temperatures, tribo layer formation can be observed in Figure 4.49b. Titanium 31 alloy worn surface can be seen in Figure 4.49c-d. With increase in temperature, more material removal is observed. The deep furrows can be observed in Figure 4.49c. The wear resistance of the NiCrSiB/WC/Ag/BaF<sub>2</sub> and NiCrSiB/WC clad is increased to 9 times and 2 times than the titanium 31 alloy substrate.

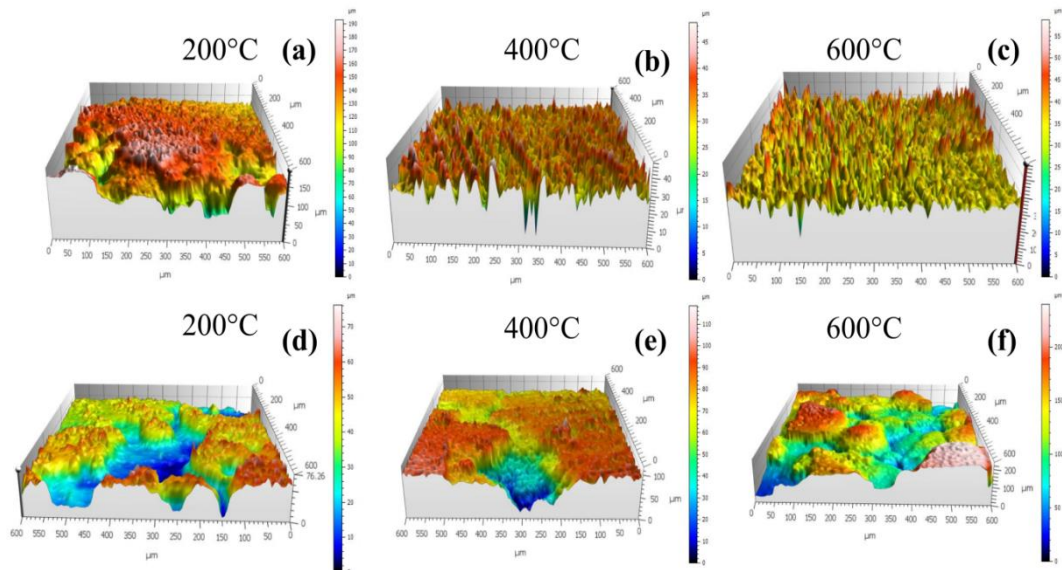


Figure 4. 46 3d surface profiles of the worn surfaces. **(a-c)** NiCrSiB/WC/Ag/BaF<sub>2</sub> clad **(d-f)** NiCrSiB/WC clad.

In order to analyze the wear mechanisms of the clads, a few 3d surface profiles of worn-out samples are shown in Figure 4.50. Comparatively, larger wear depth is observed in NiCrSiB/WC clads. The difference in wear depths indicates the glaze layer formation. The formed oxide and lubricant layer remained adhered to the surface throughout the sliding wear test. The pull-out WC particles in the clad again acted as three-body abrasion and caused more delamination. The grain pull out pits can be observed in Figure 4.50d-f.

Table 4.  $8R_a$  values of the clads at various temperatures at 20N load

$R_a$ ( $\mu\text{m}$ ) of Clad	200°C	400°C	600°C
NiCrSiB/WC/Ag/BaF <sub>2</sub>	5.543	4.112	3.445
NiCrSiB/WC	15.88	13.568	16.086

A smoother and uniform surface profile can be seen in Figure 4.50a-c than Figure 4.50d-f.  $R_a$  values of both clad at different temperatures are presented in Table 4.8. The  $R_a$  value of NiCrSiB/WC/Ag/BaF<sub>2</sub> clad at 200°C is observed to be 3.60 times lower than the NiCrSiB/WC clad. As temperature increased to 600°C,  $R_a$  value of NiCrSiB/WC/Ag/BaF<sub>2</sub> clad is reduced to 4.112, which is 4.66 lower than the NiCrSiB/WC clad.

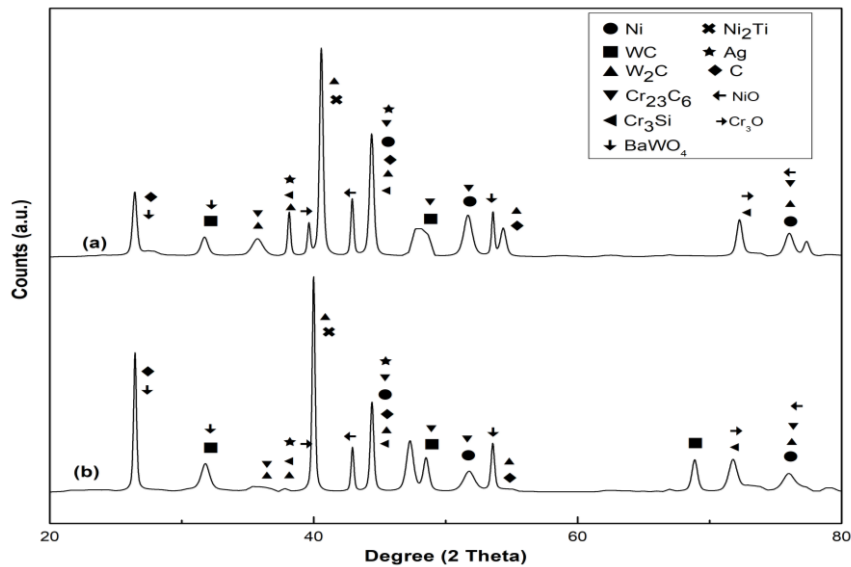


Figure 4. 47 XRD analysis of NiCrSiB/WC/Ag/BaF<sub>2</sub> clad worn surface after sliding wear test at 20N load (a) 200°C, (b) 600°C.

The phase analysis of NiCrSiB/WC/Ag/BaF<sub>2</sub> clad worn surfaces at 200°C and 600°C are shown in Figure 4.51. The factors such as friction heating and chamber temperature can alter the peak intensity. There is a formation of Ag phase at 200°C. At 600°C, Ag is not effective to provide adequate lubrication. However, the phase BaWO<sub>4</sub> is beneficial to provide lubrication at 600°C. The oxide phases such as NiO

and  $\text{Cr}_3\text{O}$  are observed on the clad. The formed lubricant and oxide layer formation is adequate to reduce direct material contact with the counter body. The formation of the intermetallic phase  $\text{Ni}_2\text{Ti}$  indicates the strong metallurgical bonding. Other hard phases like  $\text{W}_2\text{C}$ ,  $\text{Cr}_{23}\text{C}_6$  are beneficial to reduce material loss. For example, zhu et al. developed the  $\text{Ni}_3\text{Al}$  matrix composites with the addition of Ag, ( $\text{BaCrO}_4$ ,  $\text{BaMoO}_4$ ) to improve wear resistance. The glaze layer formed with barium salt at higher temperatures is showed a favorable lubrication effect compared to Ag lubricant. The combined effect of Ag and barium salt on the clad surface is increased with the temperature range (Zhu et al. 2015). Similar studies focused on adding lower and high temperature resistant solid lubricants in the composites to enhance tribological properties (Kong et al. 2013). In the present study, lubricity formed due to the combined effect of Ag and  $\text{BaF}_2$  is sufficient to achieve good tribological properties for a broad temperature range.

#### **4.7.3 NiCrSiB/WC/Ag/hBN and NiCrSiB/WC/MoS<sub>2</sub>/hBN TIG claddings**

The dry sliding wear studies were conducted on the pin on disc tribometer for the coating samples developed at 90 A. Figure 4.52 shows the representation of weight loss at various loads and temperatures. It was clearly demonstrated that the weight loss of both coatings was increased with the load. The weight loss of the coating samples at higher loads was mainly experienced due to the micro-cutting and microcracking, which further leads to detachment of WC particles. The rise of temperature leads to the formation of tribo layer containing oxides and solid lubricants. The formed tribo layer was further beneficial to reduce the weight loss of the samples. A maximum weight loss of 16 mg has occurred at 200 °C under 40 N load for coating-A. The minimum weight loss (9.5 mg) for coating-A occurred at 600 °C under 20 N load. Similarly, the maximum weight loss (18 mg) of coating-B at 200 °C was noted under 40 N load. At 600 °C, minimum weight loss (10.5 mg) was reported under 20 N load.

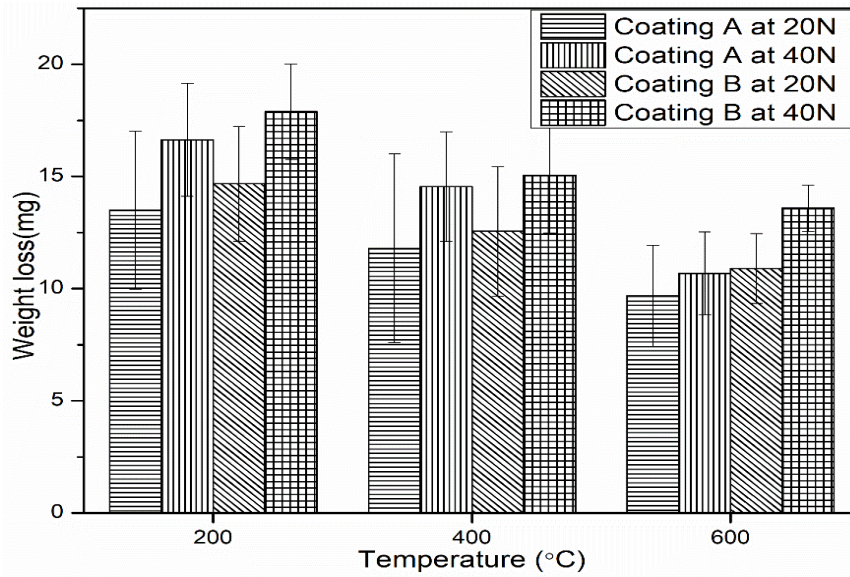


Figure 4. 48 weight loss of NiCrSiB/WC/Ag/hBN clad and NiCrSiB/WC/MoS<sub>2</sub>/hBN clad at different temperatures and loads.

The variation of coefficient of friction with time is shown in Figure 4.53. More fluctuations can be observed at higher loads, which could be more likely due to the debonding of WC particles. It can be observed from Figure 4.53 that the average coefficient of friction of NiCrSiB/WC/Ag/hBN clad was reduced from 0.42 to 0.34 under 20N load as increasing temperature from 200 °C to 600 °C. Similarly, the coefficient of friction of NiCrSiB/WC/MoS<sub>2</sub>/hBN clad was reduced from 0.47 to 0.37 with the increasing temperature from 200 °C to 600 °C. The homogenous phase distribution in the coating seems to influence the wear rate of the coating. The WC dispersed particles in the coating would strengthen the matrix phase and enhance the wear resistance of the coating.

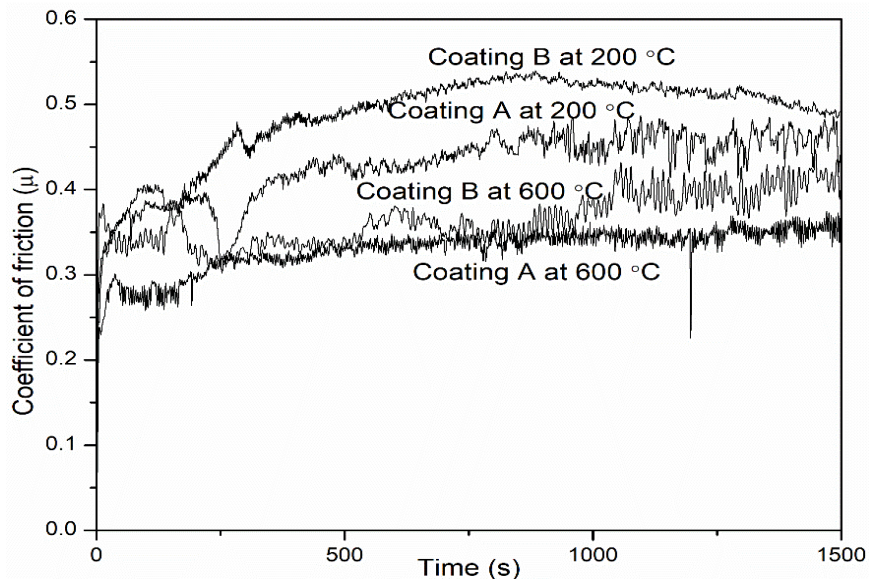


Figure 4. 49 Variation in coefficient of friction with respect to sliding time.

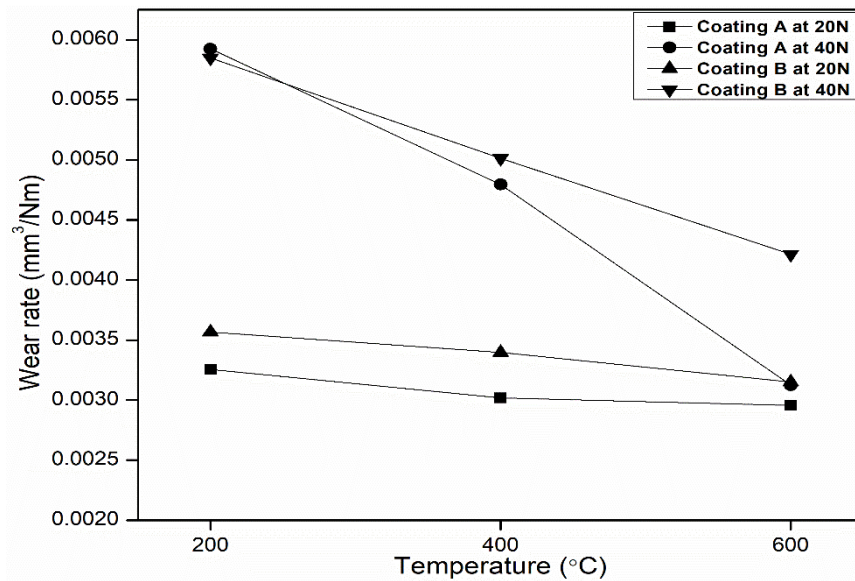


Figure 4. 50 Wear rate of the coated samples at different temperatures under various loads.

Figure 4.54 represents the wear rate of the coatings at temperatures 200 °C, 400 °C, 600 °C under loads of 20 N, 40 N. The coating-A showed the lowest wear rate around  $2.96 \times 10^{-3} \text{ mm}^3/\text{N-m}$  between both coatings at different process parameters. The formed lubricant layer containing Ag and hBN was reduced the wear rate

effectively at 600 °C under 20 N load. The oxide layers developed in the wear track enhance the resistance to localized plastic shearing and improve wear resistance. Between both coatings, coating-A showed the highest wear rate of  $5.92 \times 10^{-3} \text{ mm}^3/\text{N}\cdot\text{m}$ . Similarly, titanium 31 substrate showed lower wear rate of  $89 \times 10^{-3} \text{ mm}^3/\text{N}\cdot\text{m}$  at 200 °C under 20 N load. As increasing temperature to 600 °C under 40 N, titanium31 substrate showed highest wear rate of  $132 \times 10^{-3} \text{ mm}^3/\text{N}\cdot\text{m}$ . During sliding wear operation, tribo chemical interactions with the operating environment near the contact surface resulted in a thin lubricant layer on the surface. Such lubricant layer remained on the worn-out surface, thus preventing material loss during operation. The reduction in wear rate at higher temperatures can be correlated with the precipitation of carbides. It would increase the hardness of the coating and restrict the pull out of the WC particles. From the results, it can be summarized that the wear rate of the clad samples obtained at 90 A was comparatively lower for NiCrSiB/WC/Ag/hBN clad than NiCrSiB/WC/MoS<sub>2</sub>/hBN clad.

The wear mechanism of the clad samples was studied by analyzing the surface characteristics and their chemical composition. The worn surface appearances of the clad samples tested under different processing conditions are presented in Figure 4.55, 4.56. In both clads evaluated at lower temperatures, friction scratches were noticed created by plastic flow of the asperities in the surface because of sliding contact of the counter body. At 400 °C, particle detachments were happened by the propagation of micro-cracks on the surface. At 400 °C and up to 600°C, an effective continuous lubricant layer formed on the surface consisting of small particles observed a plastic flow. While in the case of lower mechanical strength materials, the wear produces due to the brittle formation. In the worn surfaces of NiCrSiB/WC/Ag/hBN, wear ploughs were observed at both lower and higher loads. But comparatively, larger depth ploughs were observed at higher loads. At higher temperatures, wear debris accumulated and attached to the surface due to the continuous lubricant layer forming parallel to the sliding direction. Also, thermal softening of the coating at higher temperatures would decrease the brittleness of the coating and induces the bonding between nickel alloy matrix and WC ceramic reinforcement. It was observed that a more positive effect of Ag can be observed on the worn surfaces (Figure 4.55a, d) at lower temperatures.

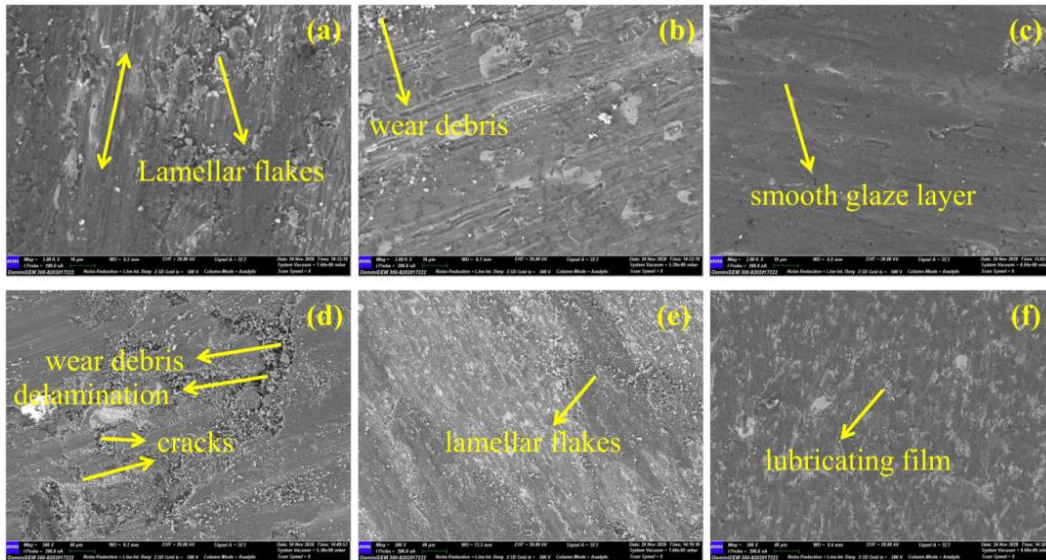


Figure 4. 51 SEM images of the wear scars of NiCrSiB/WC/Ag/hBN (a) 200 °C, 20N (b) 400 °C, 20 N (c) 600°C, 20 N (d) 200 °C, 40 N (e) 200 °C, 40N (c) 600 °C, 40 N.

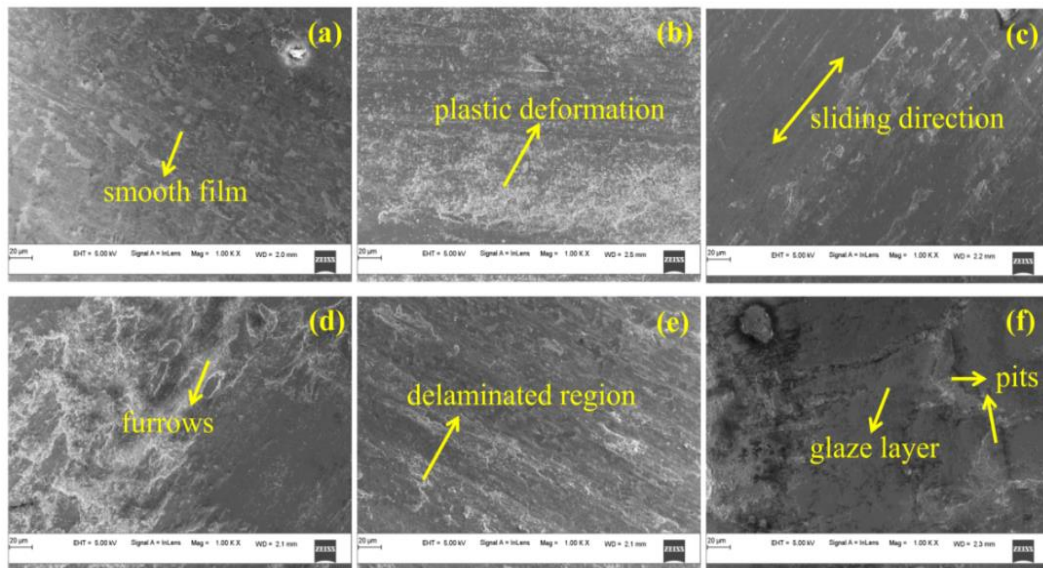


Figure 4. 52 SEM images of the wear scars of NiCrSiB/WC/MoS2/hBN clad (a) 200 °C, 20N (b) 400 °C, 20 N (c) 600°C, 20 N (d) 200 °C, 40 N (e) 200 °C, 40N (c) 600 °C, 40 N.

In some areas, severe wear was formed due to the delamination process. In the present study, severe wear mainly occurred under higher loading conditions at all

operating temperatures. Under 20N load, material removal occurred mainly due to the adhesive wear regime. However, as the load increased from 20 N to 40 N, material removal occurred because of combined adhesive and abrasive wear action. The coefficient of friction values also was unstable at the starting stages of the test due to the non-uniform surface contact. The wear that occurred at the starting of the test mainly occurred due to abrasive wear. At higher loads, material removal taken place from the surface could be caused due to micro-cutting as well as ploughing. The primary eutectic WC/W<sub>2</sub>C has higher fracture toughness in both coatings because of their feathery structure. The worn surfaces of both coatings suggest that they experienced thermal softening due to the accumulated frictional heat between pin and counter disc. The debris formed due to the plastic deformation further helps to reduce the effective area of contact.

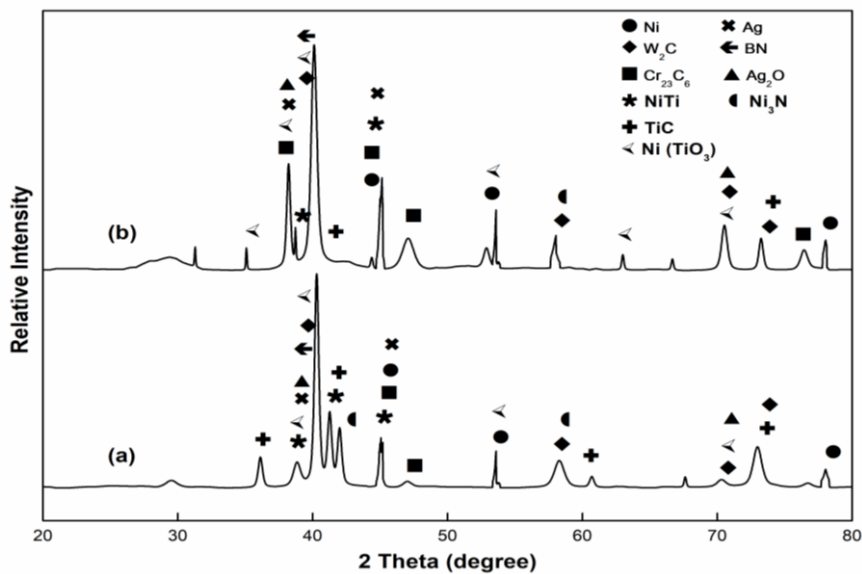


Figure 4. 53 XRD patterns of the worn surfaces of NiCrSiB/WC/Ag/hBN clad at operating temperature of (a) 200 °C (b) 600 °C.



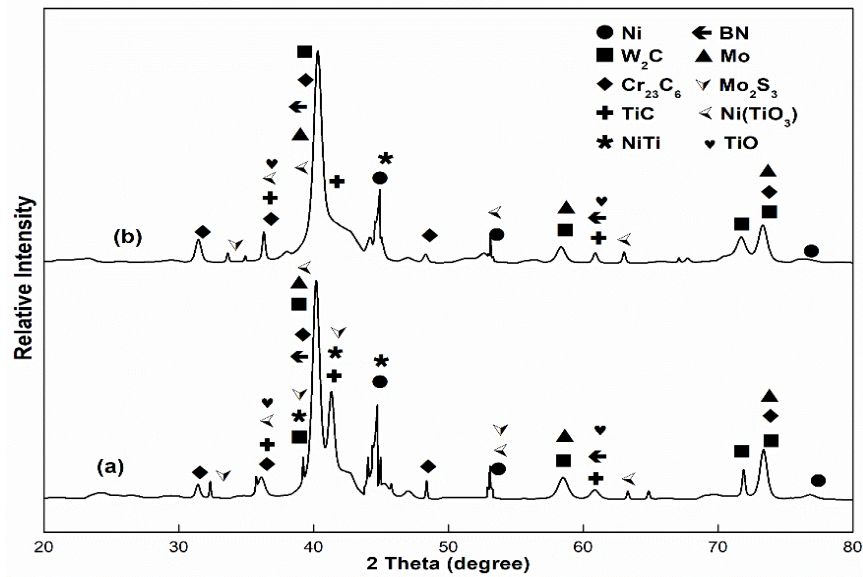


Figure 4. 54 XRD patterns of the worn surfaces of NiCrSiB/WC/MoS<sub>2</sub>/hBN clad at operating temperature of (a) 200 °C (b) 600 °C.

Figure 4.57 shows the XRD results of NiCrSiB/WC/Ag/hBN clad worn surfaces obtained at low (200 °C) and high (600 °C) temperatures. The phases Ni,  $W_2C$ ,  $Cr_{23}C_6$ , and NiTi were the predominant phases in the coating. The lubricant phases Ag, hBN, and oxide phases  $Ag_2O$  and Ni ( $TiO_3$ ) were also present in the coating indicate the effective lubricant layer formation. The oxide peaks of the phases NiO, ( $TiO_3$ ), and  $Ag_2O$  were more intense in Figure 4.57b than Figure 4.57a, which could be attributed to increased temperature. Similarly, Figure 4.58 shows the XRD analysis of the worn surface of NiCrSiB/WC/MoS<sub>2</sub>/hBN clad. The main phases obtained in the coating were Ni,  $W_2C$ ,  $Cr_{23}C_6$ , NiTi, TiC. The lubricant phases  $Mo_2S_3$ , BN, and oxide phases TiO, Ni ( $TiO_3$ ) formed in the coating were adequate to increase the wear resistance of the coating.

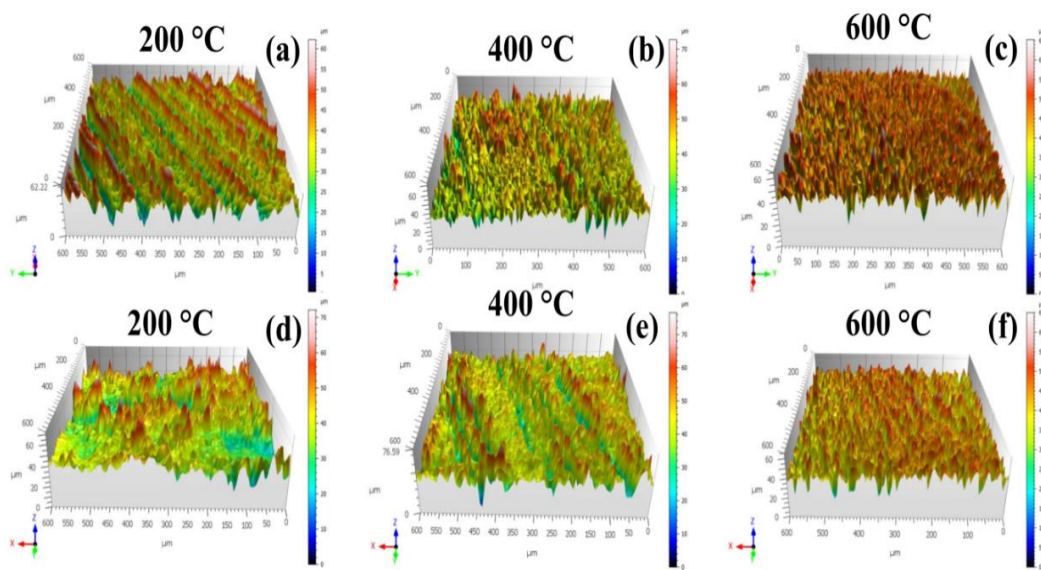


Figure 4.55 3D surface profiles of the worn surfaces (a-c) NiCrSiB/WC/Ag/hBN clad (d-e) NiCrSiB/WC/MoS<sub>2</sub>/hBN clad.

The wear tracks formed on the surfaces of coatings under dry sliding wear conditions were represented as surface profiles using a 3D surface profilometer. It was evident from Figure 4.59 that the width and depth of the wear tracks of NiCrSiB/WC/MoS<sub>2</sub>/hBN clad were comparatively larger than NiCrSiB/WC/Ag/hBN clad, indicating lower wear resistance at elevated temperatures. In addition, the grooves observed on the surface were irregular, which was likely due to the embedded WC particles. While at higher loads, pits were formed on the worn surface because of carbide pull out.

#### 4.7.4 NiCrSiB/WC/Ag/hBN and NiCrSiB/WC/MoS<sub>2</sub>/hBN MHH claddings

The tribological experiments were conducted to evaluate the effect of lubricants at elevated temperatures under various loads. Before the wear test, the surface roughness (Ra) of NiCrSiB/WC/Ag/hBN clad and NiCrSiB/WC/Mo<sub>2</sub>/hBN clad samples were noted as 5.95 µm and 6.12µm, respectively. The composite clad containing lubricant phases such as Ag/hBN and MoS<sub>2</sub>/hBN affected the tribological behaviour. As depicted in Figure 4.60, the coefficient of friction was comparatively large at lower temperatures for both clad. Also, more deviation in the coefficient of friction was observed at lower temperatures. The higher fluctuation of coefficient of friction at

starting stages of the test indicates the non-uniform surface contact. With the increasing temperatures from 200 °C to 600 °C, a reduction of coefficient of friction was observed. NiCrSiB/WC/Mo2/hBN clad showed the lowest coefficient of friction (0.25) at 600 °C, 10 N load. It can be noted that temperature and load both affect the formation of lubricity. Both clad revealed a similar value of coefficient of friction at higher loads coefficient. As the temperature increased, the ductility of metallic silver increased and accelerated the Ag diffusion to the surface. Similarly, hBN enhanced the lubrication effect while performing at higher temperatures (> 400 °C). The solid lubricants Ag and MoS<sub>2</sub> can be effective at low temperatures ( $\leq 400$  °C) due to the soft characteristics of Ag and lamellar structure of MoS<sub>2</sub>. Upon heating, silver migrates by solid-state diffusion to the contact surface and reduces the friction at moderate temperatures ( $\leq 500$  °C). The wear rate of NiCrSiB/WC clad, and the substrate is shown in Figure 4.61. The wear rates of both NiCrSiB/WC clad and titanium31 alloy increased rapidly with the temperature. The wear rates of NiCrSiB/WC clad were noted as  $13.56 \times 10^{-3} \text{ mm}^3/\text{N-m}$ ,  $13.02 \times 10^{-3} \text{ mm}^3/\text{N-m}$ ,  $12.56 \times 10^{-3} \text{ mm}^3/\text{N-m}$  at 200 °C, 400 °C, and 600 °C under 10 N respectively. Similarly, the wear rates of titanium 31 alloy were noted as  $78.405 \times 10^{-3} \text{ mm}^3/\text{N-m}$ ,  $96.45 \times 10^{-3} \text{ mm}^3/\text{N-m}$ , and  $109.56 \times 10^{-3} \text{ mm}^3/\text{N-m}$  under 10 N, respectively.

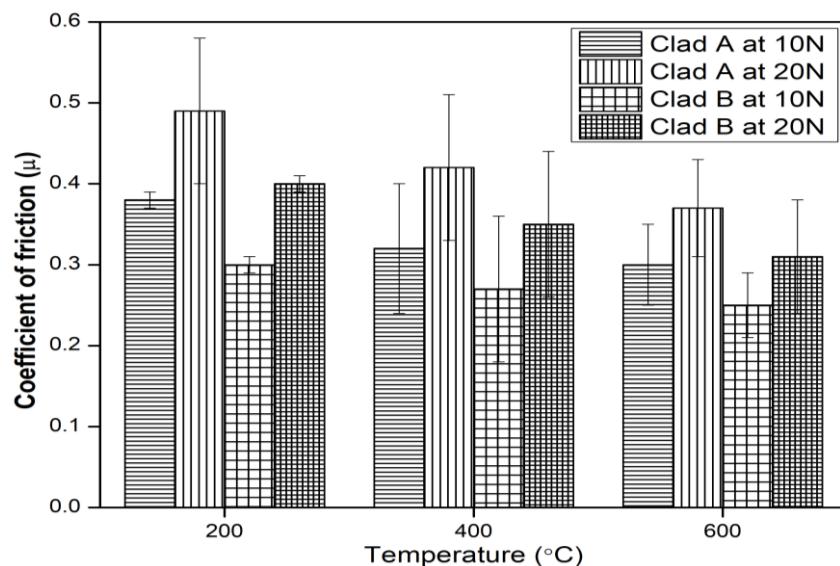


Figure 4. 56 Variation of coefficient of friction of NiCrSiB/WC/Ag/hBN clad (clad A) and NiCrSiB/WC/Mo2/hBN clad (clad B) at different temperatures and loads.

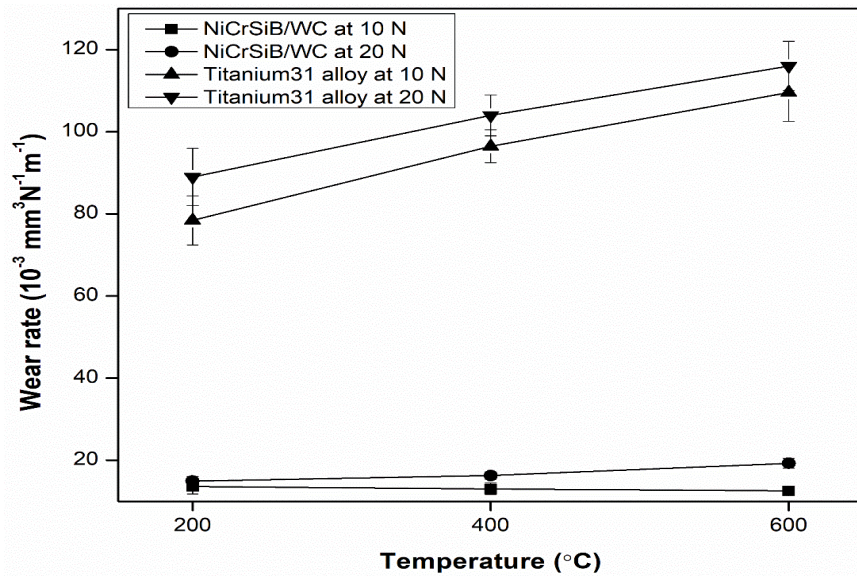


Figure 4. 57 Wear rate of the NiCrSiB/WC clad and titanium alloy at different temperatures and loads.

Figure 4.62 shows the wear rate of both clad at different temperatures and loads. The wear rate of both claddings showed the same trend as that of the coefficient of friction. The wear rates of the clads at higher temperatures were lower than clads at lower temperatures. At 200 °C, NiCrSiB/WC/Ag/hBN clad exhibited a lower wear rate ( $12.61 \times 10^{-3} \text{ mm}^3/\text{N}\cdot\text{m}$ ) than NiCrSiB/WC/MoS<sub>2</sub>/hBN clad ( $13.01 \times 10^{-3} \text{ mm}^3/\text{N}\cdot\text{m}$ ). Due to the soft characteristics and plastic deformability of Ag, it spreads on the clad surface and easily mitigates the wear rate at lower temperatures than MoS<sub>2</sub>. From Figure 4.62, the NiCrSiB/WC/MoS<sub>2</sub>/hBN clad containing MoS<sub>2</sub>/hBN lubricants combination was more effective and reduced the wear rate to  $6.65 \times 10^{-3} \text{ mm}^3/\text{N}\cdot\text{m}$  at higher temperatures (600 °C). The NiCrSiB/WC/MoS<sub>2</sub>/hBN clad has lower wear rates consistently at all temperatures and loads than NiCrSiB/WC/Ag/hBN clad.

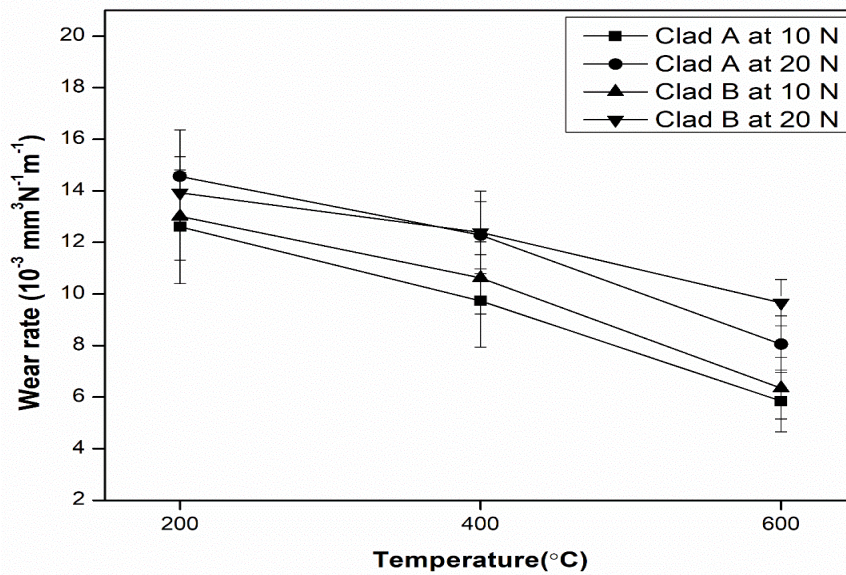


Figure 4. 58 Wear rate of NiCrSiB/WC/Ag/hBN clad (clad A) and NiCrSiB/WC/Mo<sub>2</sub>/hBN clad (clad B) at different temperatures and loads.

The SEM images of NiCrSiB/WC clad and titanium 31 alloy substrate worn surfaces are shown in Figure 4.63. It was evident from the results that more delamination was observed in the NiCrSiB/WC clad than both NiCrSiB/WC/Ag/hBN clad and NiCrSiB/WC/Mo<sub>2</sub>/hBN clad. The embedded hard particles in NiCrSiB/WC clad increased the contact stress between clad and counter body. With increasing temperature, many generated debris particles fragmented and transformed into smaller debris. These particles further compacted under normal stress, leading to the formation of scales. The wear mechanism was mainly abrasive wear at both loads, irrespective of the temperature. The SEM images of worn surfaces of NiCrSiB/WC/Ag/hBN clad is shown in Figure 4.64. At lower loads (10 N), the interfacial bond between WC particles and nickel alloy matrix was enough to reduce the pull-out force on WC particles (Figure 4.64a, c, and e). However, as the load increased from 10 N to 20 N, deep grooves and pits can be observed irrespective of the temperature because of particle spallation (Figure 4.64b, d, and f). With increasing temperature, surfaces were found to be smoother. The primary mechanism at higher loads was combined adhesive and abrasive wear.

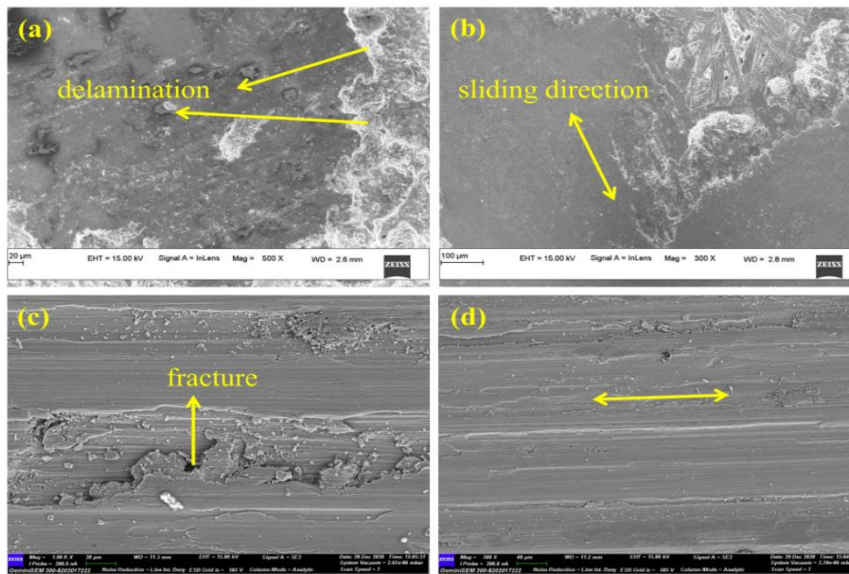


Figure 4.59 FESEM images of the wear scars under 10 N (a) NiCrSiB/WC clad at 200 °C, (b) NiCrSiB/WC clad at 600 °C, (c) Titanium 31 alloy at 200 °C, and (d) Titanium 31 alloy at 600 °C.

At lower loads, the wear mechanism was mainly adhesive wear. The formed lubrication at lower and higher temperatures was adequate at lower loads. The micro-cracks, deep grooves, and particle spallation were found in both clad, especially at higher loads. Compared to the NiCrSiB/WC/Ag/hBN clad, grooves on the NiCrSiB/WC/MoS<sub>2</sub>/hBN clad (Figure 4.65) worn surface were shallower, suggesting effective lubricant layer formation. The lubricant layer formation reduced the direct material contact with the counter body. The tribolayer formation because of the solid lubricants and oxide layer affected the tribological properties, especially at higher temperatures. At higher loads, more micro cracks and delamination were formed on the cladding. It was mainly because of the sliding and subsequent pressing of removed debris particles. Here, the wear mechanism was mainly due to the abrasive wear mechanism. The wear rates of both clad were observed lower at 600 °C, 10 N. The transfer layer has adhered to the contact surface during sliding wear operation. This phenomenon mainly attributes to the existence of lubricant film.

The XRD analysis of the NiCrSiB/WC clad is shown in Figure 4.66. The oxide phases such as Cr<sub>3</sub>O, NiO, and TiO were formed on the surface at elevated

temperatures. Similarly, The XRD analysis (Figure 4.67) confirms the presence of oxide phases  $\text{Ag}_2\text{O}$ ,  $\text{Ni}_3\text{Ti}_3\text{O}$ , and  $\text{TiO}$  and lubricant phases  $\text{Ag}$  and  $\text{BN}$  on the worn surfaces of  $\text{NiCrSiB/WC/Ag/hBN}$  clad. Similarly, oxides such as  $\text{Ni}_3\text{Ti}_3\text{O}$ ,  $\text{NiO}$ ,  $\text{TiO}$ , and lubricant phases  $\text{Mo}_2\text{S}_3$  and  $\text{BN}$  were observed on  $\text{NiCrSiB/WC/MoS}_2/\text{hBN}$  clad worn surfaces (Figure 4.68). The relative intensity of the oxide phases was increased with rising temperatures mainly due to tribo chemical interactions and frictional heating. The formed phases such as  $\text{Cr}_{23}\text{C}_6$  and  $\text{W}_2\text{C}$  on the clad surface were primarily responsible for increasing wear resistance.

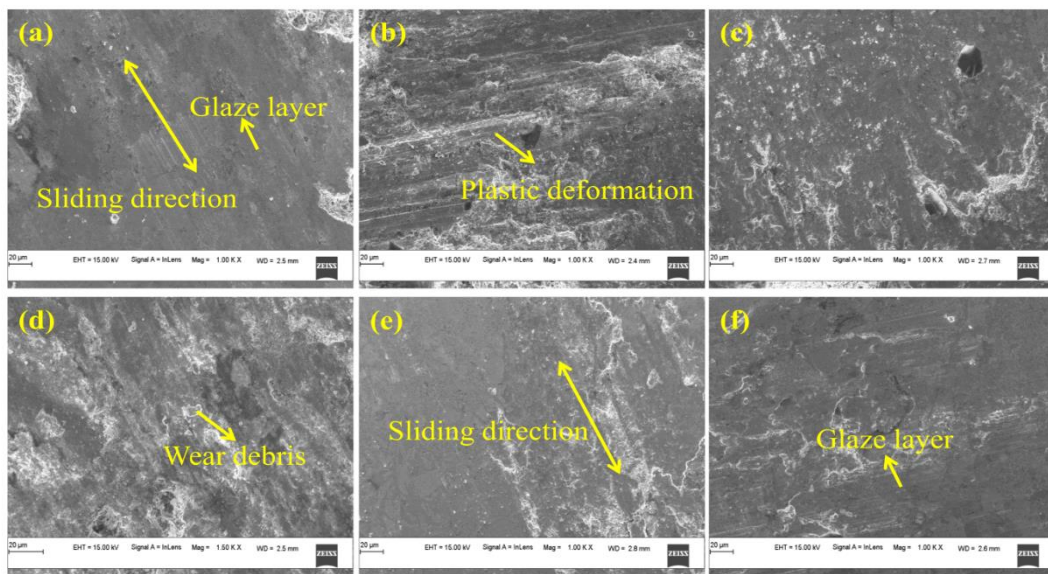


Figure 4. 60 FESEM images of the wear surfaces of  $\text{NiCrSiB/WC/Ag/hBN}$  clad at (a) 200 °C:10 N, (b) 200 °C:20 N, (c) 400 °C:10 N, (d) 400 °C:20 N, (e) 600 °C:10 N, and (f) 600 °C:20 N.

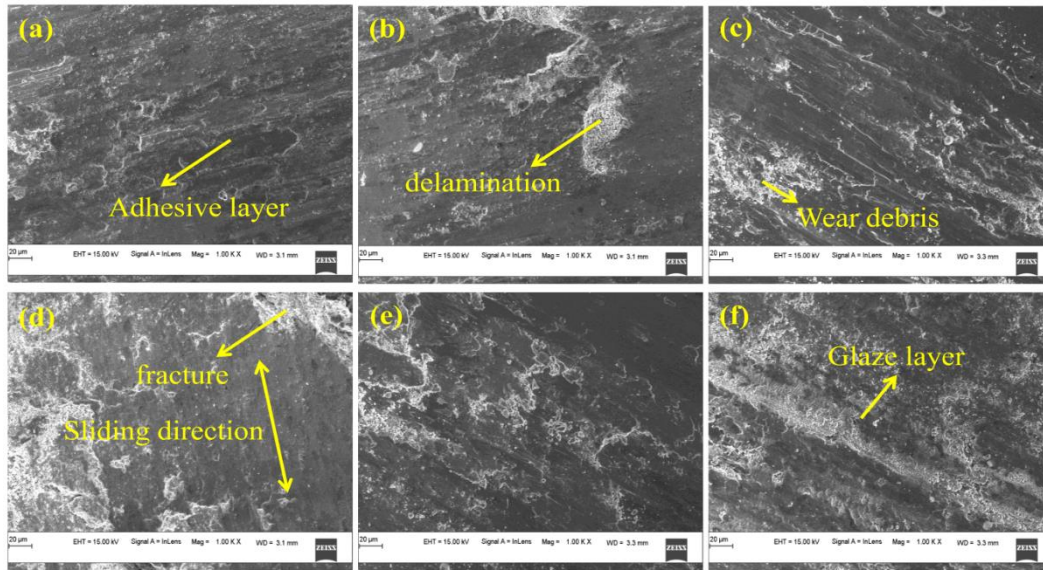


Figure 4. 61 FESEM images of the worn surfaces of NiCrSiB/WC/Mo<sub>2</sub>/hBN clad at (a) 200°C:10 N, (b) 200°C:20 N, (c) 400°C:10 N, (d) 400°C:20 N, (e) 600°C:10 N, and (f) 600°C:20 N.

The surface topography of the worn surfaces was analyzed using a non-contact 3D surface Profilometer (Figure 4.69). It was evident from the results that worn surfaces obtained at 200 °C were rougher than worn surfaces obtained at 600 °C. The deep grooves obtained at lower temperatures might be due to the lack of an adequate lubricant phase. As increasing temperatures to 600 °C, the transfer layer formed on the clad surface adhered to the worn surface at lower temperatures. However, the tribo layer formation obtained at 600 °C was not sufficient enough and caused delamination. The maximum wear depth of the NiCrSiB/WC/Ag/hBN clad at 200 °C was 130.5 μm under a 10 N load. With the increase in temperature to 600 °C, maximum wear depth was drastically reduced to 46 μm. Similarly, the maximum wear depth of NiCrSiB/WC/Mo<sub>2</sub>/hBN clad was noted as 105.35 μm at 200 °C and reduced to 30 μm with the increase of temperature to 600 °C.



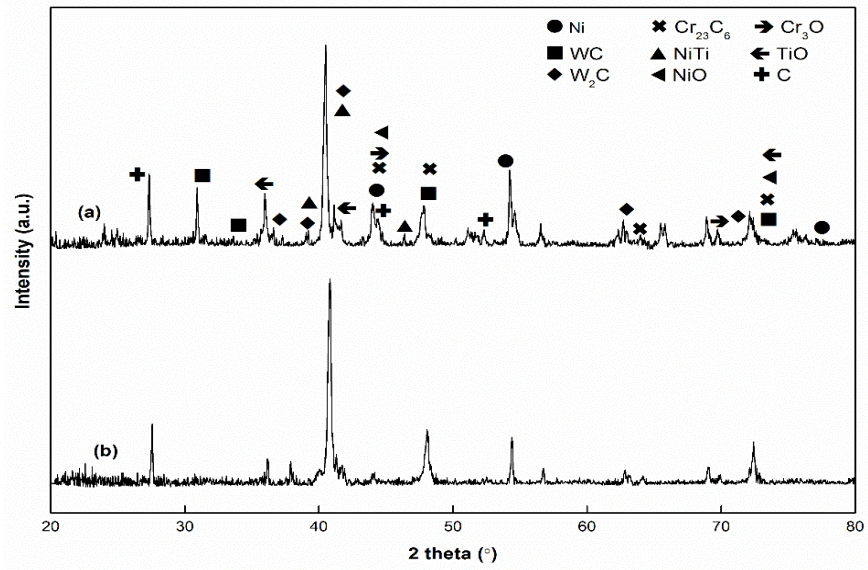


Figure 4. 62 XRD patterns of the NiCrSiB/WC clad after wear tests under 10 N load at (a) 200 °C, and (b) 600 °C.

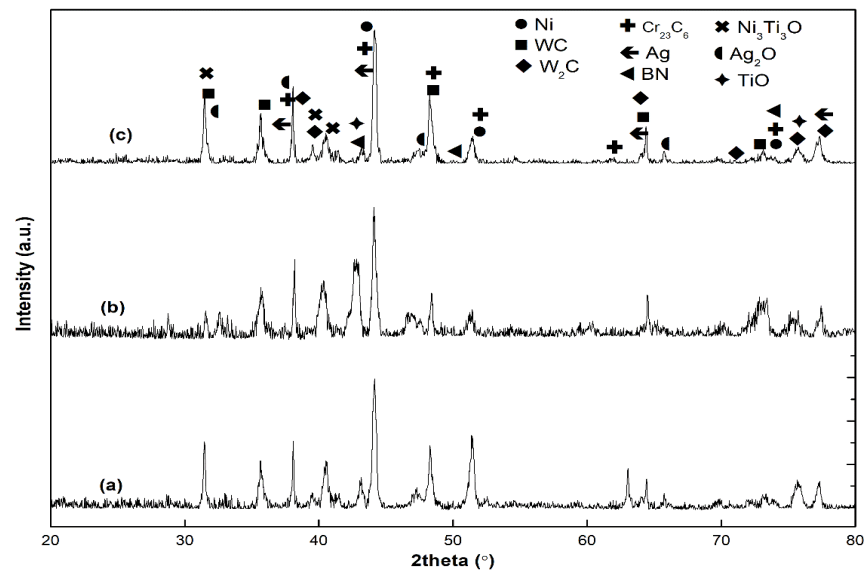


Figure 4. 63 XRD patterns of the NiCrSiB/WC/Ag/hBN clad after wear tests under 10 N load at (a) 200 °C, (b) 400 °C, and (c) 600 °C.

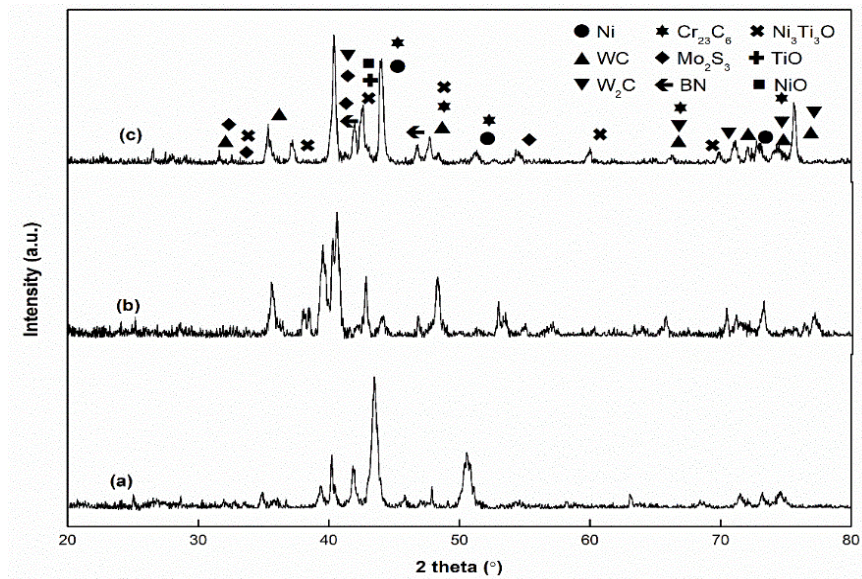


Figure 4. 64 XRD patterns of the NiCrSiB/WC/Mo<sub>2</sub>/hBN clad after wear tests under 10 N load at (a) 200 °C, (b) 400 °C, and (c) 600 °C.

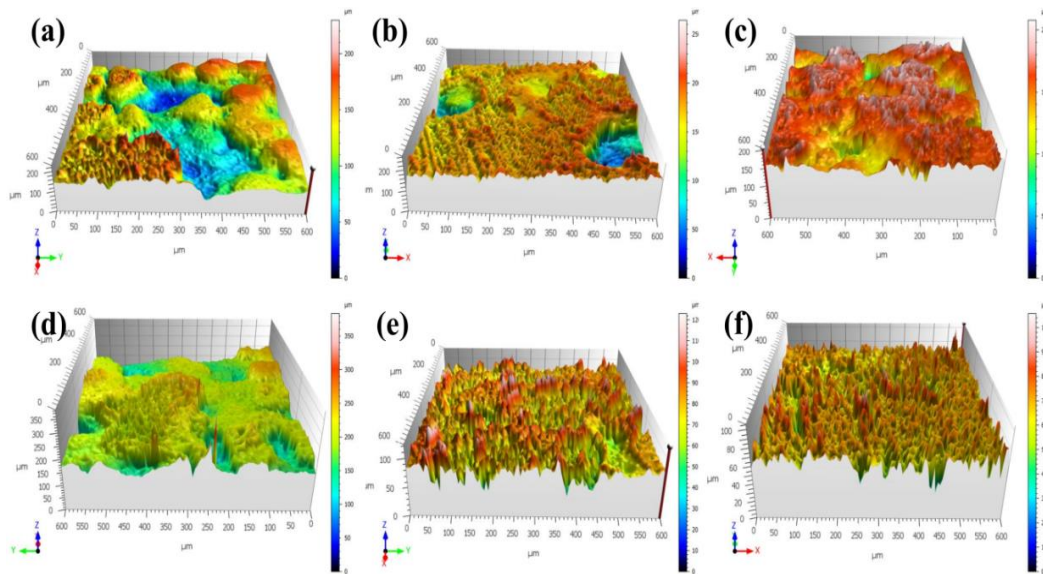


Figure 4. 65 3D optical profile of the worn surfaces under 10 N load: NiCrSiB/WC/Ag/hBN clad at (a) 200 °C, (b) 400 °C, (c) 600 °C, and NiCrSiB/WC/Mo<sub>2</sub>/hBN clad at (d) 200 °C, (e) 400 °C, (f) 600 °C.

#### 4.7.5 TIG and MHH claddings of NiCrSiB/WC/Mo<sub>2</sub>/BaF<sub>2</sub>

Figure 4.70 presented the variation of weight loss of NiCrSiB/WC/Mo<sub>2</sub>/BaF<sub>2</sub> TIG and MHH clad samples at various temperatures. It is identified that wear losses during

the sliding wear test primarily depend on various parameters such as load, temperature, sliding velocity, and surface hardness of the material and counter body. It could be seen that the weight loss of both clads was followed decreasing tendency with the temperature. The TIG and microwave clad samples showed a similar trend of weight loss throughout the temperature range. The WC reinforcement particles were beneficial to prevent straining failure at all operating temperatures. At test temperature of 600 °C, MHH clad has a weight loss of 36 mg while performing under 40 N. Comparatively, and TIG clad showed a lower weight loss of 11 mg significantly at 600 °C under 40 N.

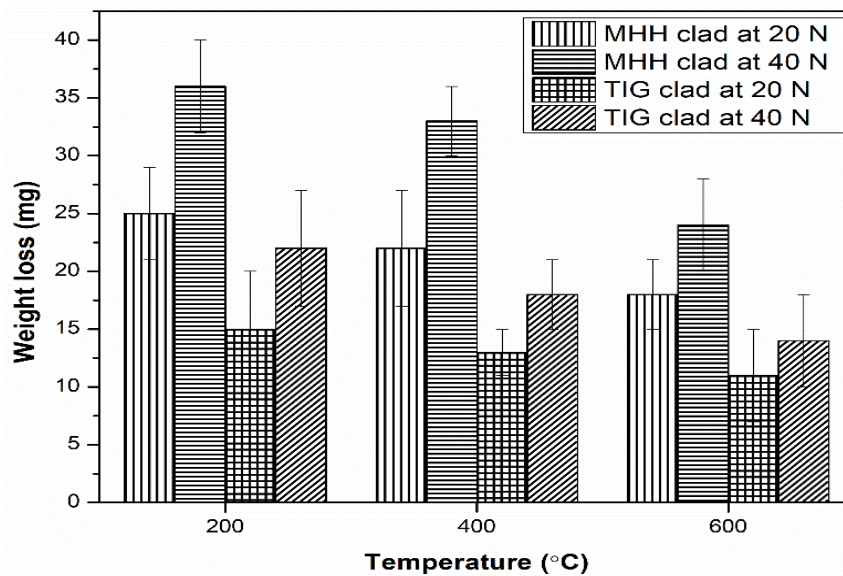


Figure 4. 66 Variation of weight loss of NiCrSiB/WC/MoS<sub>2</sub>/BaF<sub>2</sub> TIG and MHH clads at various temperatures and loads.

Due to the refined microstructure and superior hardness compared to MHH clad, TIG clad was expected to show lower weight loss. The weight loss of clads can be explained according to Archard's linear law, in which weight loss is inversely proportional to the hardness of the material. The weight loss of both clad samples increased gradually as the load increased from 20 N to 40 N. Figure 4.71 shows the variation of friction coefficient of TIG and MHH clads at various temperatures. There were two stages of friction coefficients observed. There was a gradual increase in friction coefficient with time at the beginning stage of the test. The contact area of the

sample surface against the counter body was mainly point contact at the starting stages of the test. The friction coefficient increases because of the very fine particles attached to the worn surface, which results in an increment in contact stress. The contact area of the surface increases with time, resulting in a stable friction coefficient was observed at the later stage. The degree of fluctuation of friction coefficient at 200 °C was more compared to 600 °C.

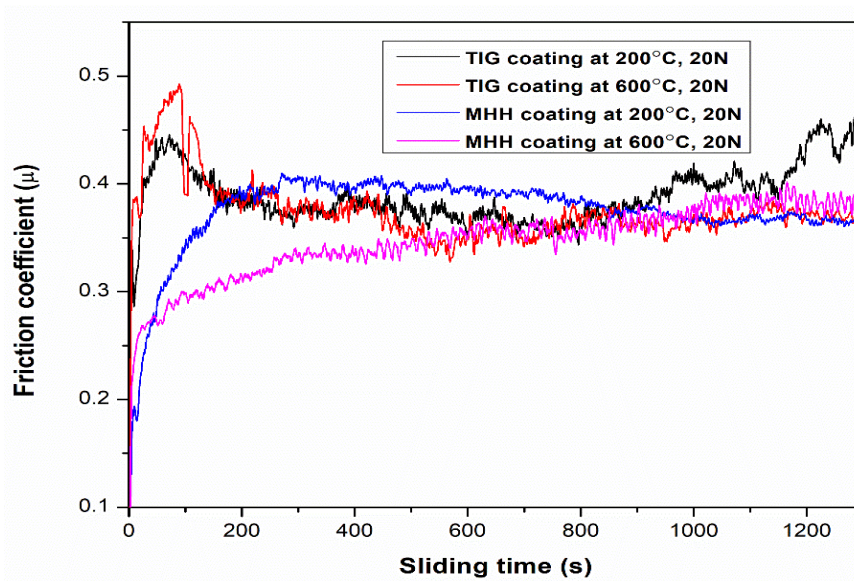


Figure 4. 67 Variation of friction coefficient with respect to sliding time for NiCrSiB/WC/MoS<sub>2</sub>/BaF<sub>2</sub> TIG clad at various temperatures and loads.

The debonded WC particles could further cut the nickel alloy matrix during the wear and friction process, increasing the friction coefficient. As increasing temperature from 200 °C to 600 °C, there was a reduction in friction coefficient. The friction coefficient of TIG clad was found lower (0.33) at 600 °C. Similarly, a lower friction coefficient (0.30) was observed for MHH clad at 600 °C. The coefficient of friction of clads at higher operating temperatures was comparatively lower, which is attributed to the easier oxidation of many elements at elevated temperatures. The lubrication formed on the clad surface reduced the degree of fluctuation of the friction coefficient. The minimum wear rate ( $3.33 \times 10^{-3} \text{ mm}^3/\text{N-m}$ ) of the TIG clad was observed at 600 °C, 20 N. The maximum wear rate ( $4.58 \times 10^{-3} \text{ mm}^3/\text{N-m}$ ) of TIG clad was observed at 200 °C, 40 N. In MHH clad, a minimum wear rate ( $3.91 \times 10^{-3}$

mm<sup>3</sup>/N-m) was observed at 600 °C, 20 N. The maximum wear rate ( $6.2 \times 10^{-3}$  mm<sup>3</sup>/N-m) noted at 200 °C, 40 N. The change in wear rate can be correlated with the friction coefficient. The reduction in wear rate with temperature indicates the synergistic lubrication effect on the clad surface. Usually, COF curves achieve steady state after attaining the uniform contact. In both clads, a decline in the amplitude of serration was observed with rising temperature, which might be due to the formation of the glaze layer. It was inferred that the asperities interaction of both contact surfaces was substantially reduced with the rising temperature. The coefficient of friction of TIG clad at 200 °C under 20 N load was changed in the range of 0.35-0.5, suggesting that rapid fluctuations occurred in the process.

SEM morphology of wear tracks of TIG and MHH calds from wear tests at different temperatures and loads are shown in Figure 4.72 and 4.73. At 200 °C, the deformation resistance of the clad under the force of friction pair was too low, induced severe material loss. At 20 N, Smooth and lamellar transfer layers were observed at lower temperatures (200 °C). Apparent traces of deformation appeared on the clad surfaces, with a certain degree of material, indicating that adhesive and abrasive wear occurred. As increasing the temperature from 200 °C to 600 °C, the delamination of the clad reduced gradually. It can be evident from Figure 4.72 that the wear mechanism was mainly adhesive wear. As shown in Figure 4.72b and e, the detachment of wear debris on the process again added to the worn surface, which leads to the wear hardening because of the mechanical and thermal cycles. The lubrication film formed on the surface at a higher temperature (>350 °C) was further hindered friction and wear rates.

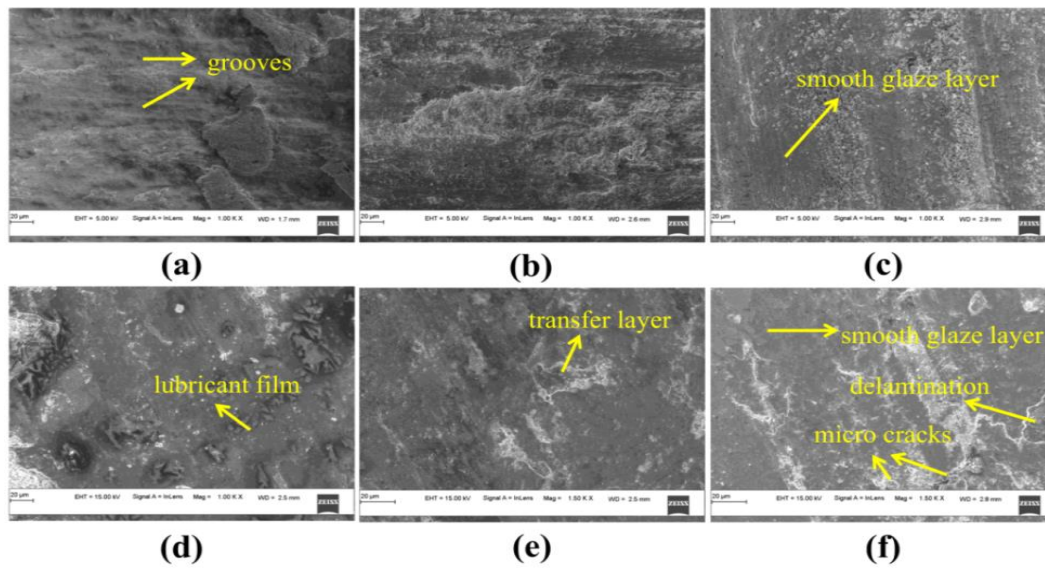


Figure 4.68 SEM results of worn surfaces of NiCrSiB/WC/MoS<sub>2</sub>/BaF<sub>2</sub> TIG clads under 20 N load at (a) 200 °C (b) 400 °C (c) 600 °C, MHH clad under 20 N load at (d) 200 °C (e) 400 °C (f) 600 °C.

As shown in Figure 4.73, comparatively more delamination was observed at 40 N. The increment of load also intensifies the friction heating and leads to the formation of the oxide layer. The grains in the wear tracks were plastically deformed along the sliding direction at temperatures above 400 °C. The MHH clad was experienced with mild adhesion at lower loads, abrasive wear and deep grooves were observed on the worn surface as raising the load from 20 N to 40 N. A smooth lubricant layer can be observed on the worn surface of both clads at high temperatures (600 °C) (Figure 4.73c and f). The elevated temperature in the wear operation intensifies the formation of lubricant layer formation on the surface. The three-body abrasion was observed on all operating conditions, especially at lower temperatures (200 °C) because of the detachment of WC particles (Figure 4.73a and d). The WC particles pull out can be identified as pits on the worn surface. The material loss was observed in TIG clad clearly due to the plastic deformation and fatigue of repeated sliding action. In the MHH clad, WC particles pull out due to the material debonding with crater formation. It can be seen that the formation of a glaze layer on the clad surface reduced the depth of furrows. Due to the push of tribo-pair, primarily micro-shear happened to the clad at higher loading conditions. When the asperities of the mating surface are harder than

the other, plastic deformation takes place and leaves grooves on the softer surface. Also, some debris particles entrap in the mating surfaces during operation. In this case, the total frictional force can be expressed as

$$F = F_a + F_d$$

F denotes the total frictional force,  $F_a$  indicates the force required to overcome the adhesive junctions, and  $F_d$  denotes the force required for deformation. There were some fatigue elated cracks on the worn surfaces that start as a result of repeated loads. At elevated temperatures, oxide layers create a lubricating effect and cause an increase in wear resistance. The oxide scale and lubricant layer were thickened with the temperature.

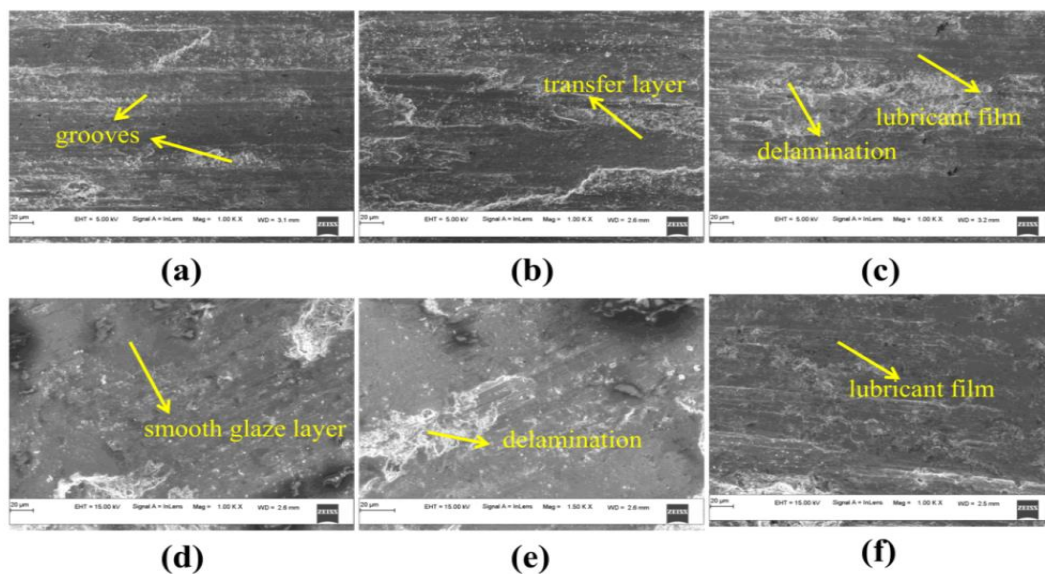


Figure 4.69 SEM results of worn surfaces of NiCrSiB/WC/MoS<sub>2</sub>/BaF<sub>2</sub> TIG clads under 40 N load at (a) 200 °C (b) 400 °C (c) 600 °C, MHH clad under 40 N load at (d) 200 °C (e) 400 °C (f) 600 °C.

Figure 4.74 shows the XRD analysis of worn surfaces of TIG and MHH clads at 200 °C and 600 °C under 20 N load. It can be seen that the intensity of worn surface peaks was increased, which might be due to the friction heating and other sintering reactions at higher temperatures. For TIG and MHH clad, the detected phases after the wear test at 200 °C and 600 °C were Ni<sub>3</sub>Ti<sub>3</sub>O, Mo, BaF<sub>2</sub>, Ba (TiO<sub>3</sub>). It indicates the

synergistic lubrication effect on the clad surface throughout the temperature range. The hard phases like  $\text{Cr}_{23}\text{C}_6$  and  $\text{W}_2\text{C}$  and intermetallic phases  $\text{NiTi}_2$  and  $\text{Ni}_3\text{Ti}$  efficiently reduced material loss. On the other hand, the formation of phase Mo on the clad surface at lower temperatures (200 °C) was acted as an effective lubricant, and phases  $\text{BaF}_2$  and  $\text{Ba}(\text{TiO}_3)$  could reduce wear rate and friction coefficient at higher temperatures (600 °C). These findings suggest solid lubricant encapsulated TIG and MHH clad are suitable for applications where high-temperature tribological play a vital role. The XRD analysis peak intensities of the oxides and lubricant phases indicate the increase of substantial increment of tribo layer formation. The percentage of hard phases in the clad at higher temperatures may have helped reduce the material softness.

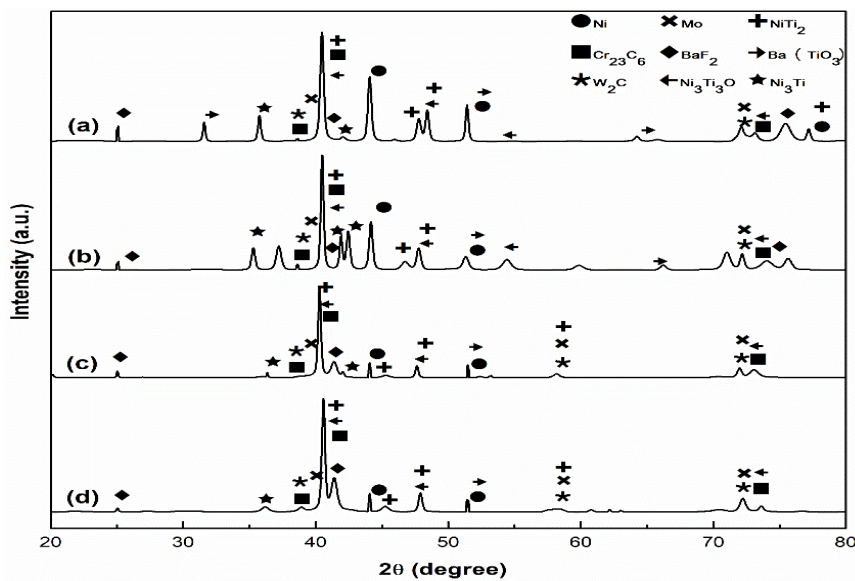


Figure 4.70 X-ray diffraction pattern of worn surface of NiCrSiB/WC/MoS<sub>2</sub>/BaF<sub>2</sub> MHH clad (90A) at (a) 200 °C (b) 600 °C, TIG clad at (c) 200 °C (d) 600 °C.

Figure 4.75 portrays the 3d surface topography and profiles of the worn surfaces of TIG clad at 200 °C and 600 °C under 20 N load. The difference between maximum peak height and the valley depth can be identified as the material removal due to sliding wear operation, which is reported to be 45 μm at 200 °C Figure 4.75c.



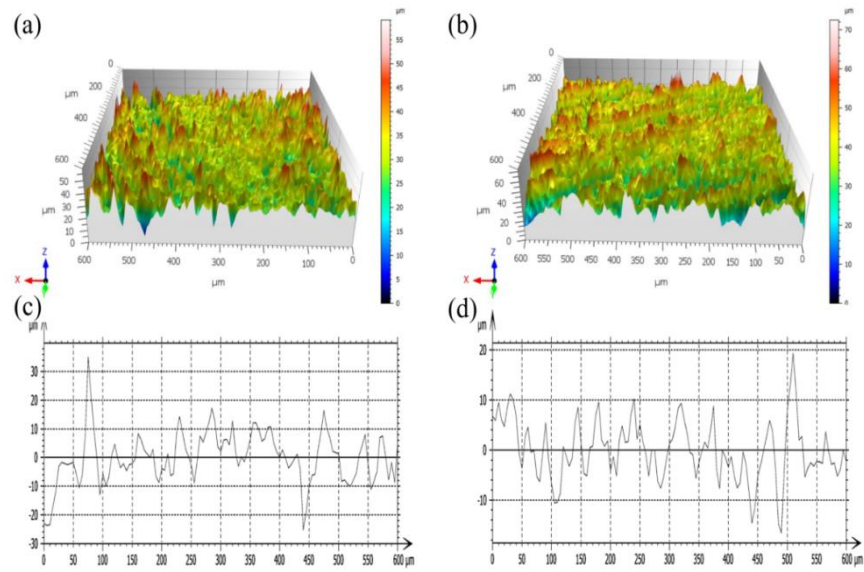


Figure 4. 71 3d surface profiles of the worn surfaces of NiCrSiB/WC/MoS<sub>2</sub>/BaF<sub>2</sub> TIG clad under 20 N load (a) 200 °C (b) 600 °C; texture profiles of TIG clad under 20 N (c) 200 °C (d) 600 °C.

As the operating temperature increased to 600 °C, the damage to the surface reduced, indicating the lubricant layer formation. In this case, the difference between maximum peak height to the depth value was noted as 32 μm Figure 4.75d. Similarly, 3d surface topography and profiles of the worn surfaces of MHH clad are shown in Figure 4.76. At 200 °C, the maximum peak to valley depth was reported to be 106 μm Figure 4.76c. With the increase of operating temperature to 600 °C, the value of their difference was decreased to 36 μm Figure 4.76d, indicating less wear loss. From Figure 4.76a and d, it can also be understood that the depth of grooves or waviness at 200 °C were comparatively deeper than the worn surfaces obtained at 600 °C. It can be inferred from these 3d surface profiles and topography images that TIG clad samples offered better wear resistance to sliding wear at higher operating temperatures than MHH clad samples.

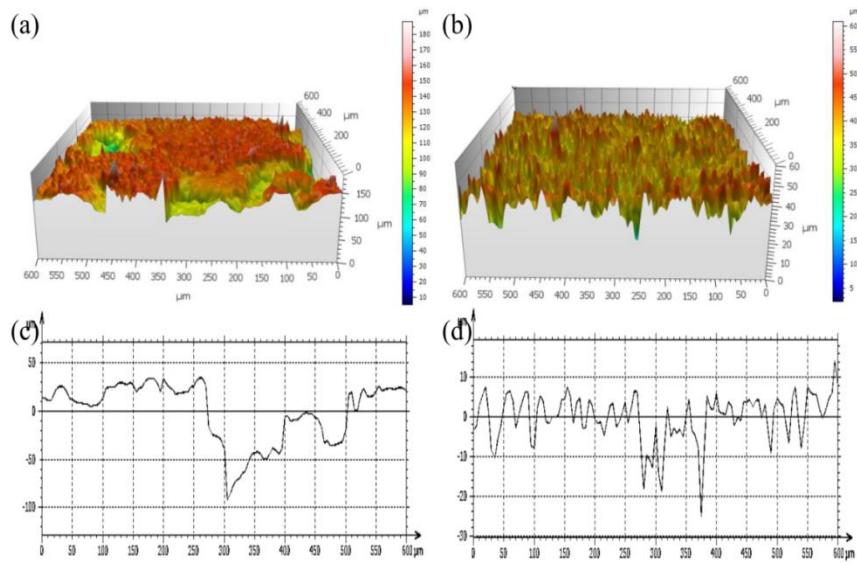


Figure 4. 72 3d surface profiles of the worn surfaces of NiCrSiB/WC/MoS<sub>2</sub>/BaF<sub>2</sub> MHH clad under 20 N load (a) 200 °C (b) 600 °C; texture profiles of MHH clad under 20 N (c) 200 °C (d) 600 °C.

#### 4.7.6 Comparative Discussion

All the developed claddings produced by TIG and MHH techniques exhibited lower friction coefficient and wear rate as compared to titanium 31 alloy substrate. The lower friction coefficient of clads is attributed to the lubricating property of the solid lubricants incorporated in the coatings. Solid lubricants possess lower shear strength and easily get sheared on the rubbing surfaces, reducing the friction coefficient. Ag, MoS<sub>2</sub> provides lubrication below 400 °C while at elevated temperatures (> 600 °C), BaF<sub>2</sub> and hBN provide lubrication. The relative wear resistance of the TIG and MHH clads followed a similar sequence.

NiCrSiB/WC/Ag/BaF<sub>2</sub> > NiCrSiB/WC/Ag/hBN > NiCrSiB/WC/MoS<sub>2</sub>/hBN > NiCrSiB/WC/MoS<sub>2</sub>/BaF<sub>2</sub> > Titanium 31 alloy substrate.

Comparatively, TIG clads processed at lower currents showed better mechanical properties. The wear resistance of TIG processed clads showed better wear resistance than the MHH processed clads, which might be attributed to the induced heat input in the process leading to the formation of hard intermetallic phases.

## CHAPTER 5

### CONCLUSIONS

In the present study, nickel-based composite clads composed of a matrix, reinforcement, and lubricant phase are successfully deposited using TIG and microwave hybrid heating techniques. As a result of this study, the following insights and findings concerning the microstructural and tribological performance of the solid lubricant encapsulated nickel alloy is found.

- The NiCrSiB/WC, NiCrSiB/WC/Ag/BaF<sub>2</sub>, NiCrSiB/WC/Ag/hBN, NiCrSiB/WC/MoS<sub>2</sub>/hBN, and NiCrSiB/WC/MoS<sub>2</sub>/BaF<sub>2</sub> clads deposited by TIG cladding showed average porosity of 2 %. Whereas all microwave deposited clads showed less than 1 % porosity.
- As the TIG current increased, the microhardness of the TIG deposited clads decreased. The higher amount of heat input in the process causes the dissolution of hard phases, which further reduces hardness.
- As increasing the TIG current, the reinforcing WC particles were significantly refined and homogeneously distributed in the clad due to the change of thermal gradient. Due to the solute redistribution in the solidification process, more equiaxed grains were observed at higher TIG current processed clads. Also, a higher current increases the solidification time for coating and leads to coarse and dendritic structures.
- In lower TIG current processed clads, fracture toughness was found to be higher due to the higher content of the ceramic phase. The high ceramic phase negatively affected clad and induced brittle cracking under conditions of 2000 gf. In higher current processed clads, the dissolution of hard phases happened, which further reduced fracture toughness.
- No cracks are obtained on the interface during the assessment of interfacial strength, which indicates the strong metallurgical bonding between clads and substrate material.

- All MHH clads consist of a dense uniform morphological structure with negligible thermal defects and less porosity as compared with TIG clads due to the volumetric heating.
- At 200 °C, Ag and MoS<sub>2</sub> provided the lubrication by easily getting sheared on the sliding surfaces, while at 600 °C, high-temperature solid lubricants like BaF<sub>2</sub> and hBN offered adequate lubrication.
- The friction coefficient and wear rate of the titanium 31 alloy substrate were found to be increased with an increase of normal load and temperature.
- Based on the wear rate data, the relative wear resistance of both TIG and MHH claddings under dry sliding conditions followed the same sequence:

NiCrSiB/WC/Ag/BaF<sub>2</sub> > NiCrSiB/WC/Ag/hBN > NiCrSiB/WC/MoS<sub>2</sub>/hBN > NiCrSiB/WC/MoS<sub>2</sub>/BaF<sub>2</sub> > NiCrSiB/WC.

- The dominant wear mechanism of the claddings was mainly adhesive wear at lower loading conditions and showed the combined adhesive and abrasive wear action at higher loads. The higher wear resistance of solid lubricant encapsulated claddings is attributed to their synergistic lubrication effect at all operating temperatures.

## References

- Abboud, J., Rawlings, R., and West, D. (1995). "Functionally graded nickel-aluminide and iron-aluminide coatings produced via laser cladding." *J. Mater. Sci.*, 30, 5931–5938.
- Allam, I. M. (1991). "Solid lubricants for applications at elevated temperatures." *J. Mater. Sci.*, 26(15), 3977–3984.
- Aouadi, S. M., Luster, B., Kohli, P., Muratore, C., and Voevodin, A. A. (2009). "Surface & Coatings Technology Progress in the development of adaptive nitride-based coatings for high temperature tribological applications." *Surf. Coat. Technol.*, 204(6–7), 962–968.
- Aouadi, S. M., Paudel, Y., Luster, B., Stadler, S., Kohli, P., Muratore, C., Hager, C., and Voevodin, A. A. (2008). "Adaptive Mo 2N/MoS 2/Ag tribological nanocomposite coatings for aerospace applications." *Tribol. Lett.*, 29(2), 95–103.
- Aristizabal, M., Ardila, L. C., Veiga, F., Arizmendi, M., Fernandez, J., and Sánchez, J. M. (2012). "Comparison of the friction and wear behaviour of WC-Ni-Co-Cr and WC-Co hardmetals in contact with steel at high temperatures." *Wear*, 280–281, 15–21.
- Aytekin, H., and Akçin, Y. (2013). "Characterization of borided Incoloy 825 alloy." *Mater. Des.*, 50, 515–521.
- Babu, A., Arora, H. S., Singh, H., and Grewal, H. (2019). "Microwave Synthesized Composite Claddings with Enhanced Cavitation Erosion Resistance." *Wear*, 422–423.
- Babuska, T. F., Pitenis, A., Jones, M., Nation, B. L., Sawyer, W. G., and Argibay, N. (n.d.). "Temperature dependent friction behavior of PTFE and MoS 2." 1–12.
- Badisch, E., Fontalvo, G. A., Stoiber, M., and Miterrer, C. (2003). "Tribological behavior of PACVD TiN coatings in the temperature range up to 500 °C." *Surf. Coatings Technol.*, 163–164, 585–590.
- Bandyopadhyay, A., Zhang, Y., and Bose, S. (2020). "Recent developments in metal additive manufacturing." *Curr. Opin. Chem. Eng.*, 28, 96–104.
- BAO, R., YU, H., CHEN, C., QI, B., and ZHANG, L. (2006). "DEVELOPMENT OF LASER CLADDING WEAR-RESISTANT COATING ON TITANIUM ALLOYS." *Surf. Rev. Lett.*, 13(05), 645–654.

- Bayata, F., and Alpas, A. T. (2021). “The high temperature wear mechanisms of iron-nickel steel (NCF 3015) and nickel based superalloy (inconel 751) engine valves.” *Wear*, 480–481(March).
- Bello, K. A., Maleque, M. A., Adebisi, A. A., and Dube, A. (2016). “Preparation and characterisation of TIG-alloyed hybrid composite coatings for high-temperature tribological applications.” *Trans. Inst. Met. Finish.*, 94(4), 211–221.
- Berns, H. (2003). “Comparison of wear resistant MMC and white cast iron.” *Wear*, 254(1–2), 47–54.
- Bhosale, D. G., Rathod, W. S., Ghorpade, U. S., and Rukhande, S. W. (2020). “Nickel alloy C-263 protection by WC[ $\text{Cr}_3\text{C}_2$ ]Ni coatings against high-temperature wear in nuclear applications.” *Surfaces and Interfaces*, 21(July), 100689.
- Blanchet, T., Kim, J.-H., Calabrese, S., and Dellacorte, C. (2002). “Thrust-Washer Evaluation of Self-Lubricating PS304 Composite Coatings in High Temperature Sliding Contact.” *Tribol. Trans. - TRIBOL TRANS*, 45, 491–498.
- Blau, P. J. (2010). “Elevated-temperature tribology of metallic materials.” *Tribol. Int.*, 43(7), 1203–1208.
- Budzynski, P., Youssef, A. A., and Sielanko, J. (2006). “Surface modification of Ti-6Al-4V alloy by nitrogen ion implantation.” *Wear*, 261(11–12), 1271–1276.
- Buytoz, S., Ulutan, M., and Yildirim, M. M. (2005). “Dry sliding wear behavior of TIG welding clad WC composite coatings.” *Appl. Surf. Sci.*, 252(5), 1313–1323.
- Chandrasekaran, S., Basak, T., and Ramanathan, S. (2011). “Experimental and theoretical investigation on microwave melting of metals.” *J. Mater. Process. Technol.*, 211(3), 482–487.
- Chen, Y., Lu, F., Zhang, K., Nie, P., Elmi Hosseini, S. R., Feng, K., Li, Z., and Chu, P. K. (2016). “Investigation of dendritic growth and liquation cracking in laser melting deposited Inconel 718 at different laser input angles.” *Mater. Des.*, 105, 133–141.
- Chhillar, P., Agrawal, D., and Adair, J. H. (2008). “Sintering of molybdenum metal powder using microwave energy.” *Powder Metall.*, 51(2), 182–187.
- Cho, S., and Lee, J. (2008). “Metal recovery from stainless steel mill scale by microwave heating.” *Met. Mater. Int.*, 14(2), 193–196.
- Cockeram, B. V. (2002). “The fracture toughness and toughening mechanisms of

- nickel-base wear materials.” *Metall. Mater. Trans. A*, 33(1), 33–56.
- Conde, A., Zubiri, F., and Damborenea, J. de. (2002). “Cladding of Ni–Cr–B–Si coatings with a high power diode laser.” *Mater. Sci. Eng. A*, 334, 233–238.
- Cotell, C. M., Sprague, J. A., and Smidt F.A., J. (1994). *Surface Engineering*. ASM International.
- Cura, M. E., Liu, X. W., Kanerva, U., Varjus, S., Kivioja, A., Söderberg, O., and Hannula, S. P. (2015). “Friction behavior of alumina/molybdenum composites and formation of MoO<sub>3-x</sub> phase at 400 °c.” *Tribol. Int.*, 87, 23–31.
- Das, C. R., Albert, S. K., Bhaduri, A. K., and Nithya, R. (2007). “Effects of dilution on microstructure and wear behaviour of NiCr hardface deposits.” *Mater. Sci. Technol.*, 23(7), 771–779.
- Dearnley, P. A. (2017). “Introduction to Surface Engineering.” *Introd. to Surf. Eng.*, 1–510.
- Dehm, G. (2002). “Laser cladding of Co-based hardfacing on Cu substrate.” *J. Mater. Sci. v.37*, 5345-5353, 37.
- Dellacorte, C., and Fellenstein, J. A. (1997). “The Effect of Compositional Tailoring on the Thermal Expansion and Tribological Properties of PS300: A Solid Lubricant Composite Coating.” *Tribol. Trans.*, 40, 639–642.
- Ding, C. H., Li, P. L., Ran, G., and Zhou, J. N. (2008). “PM304 coating on a Ni-based superalloy rod for high temperature lubrication.” *Ceram. Int.*, 34(2), 279–284.
- Doddamani, M., Mathapati, M., and Ramesh, M. R. (2018). “Microstructure and tribological behavior of plasma sprayed NiCrAlY/WC-Co/cenosphere/solid lubricants composite coatings.” *Surf. Coatings Technol.*, 354(September), 92–100.
- Eghlimi, A., Shamanian, M., and Raeissi, K. (2014). “Effect of current type on microstructure and corrosion resistance of super duplex stainless steel claddings produced by the gas tungsten arc welding process.” *Surf. Coatings Technol.*, 244, 45–51.
- Evans, A. G., and Wilshaw, T. R. (1976). “Quasi-static solid particle damage in brittle solids—I. Observations analysis and implications.” *Acta Metall.*, 24(10), 939–956.
- Fallah, V., Alimardani, M., Corbin, S. F., and Khajepour, A. (2010). “Impact of localized surface preheating on the microstructure and crack formation in laser direct deposition of Stellite 1 on AISI 4340 steel.” *Appl. Surf. Sci.*, 257(5), 1716–1723.

- Farahmand, P., Liu, S., Zhang, Z., and Kovacevic, R. (2014). "Laser cladding assisted by induction heating of Ni–WC composite enhanced by nano-WC and La<sub>2</sub>O<sub>3</sub>." *Ceram. Int.*, 40(10, Part A), 15421–15438.
- Farayibi, P. K., Folkes, J., Clare, A., and Oyelola, O. (2011). "Cladding of pre-blended Ti–6Al–4V and WC powder for wear resistant applications." *Surf. Coatings Technol.*, 206(2), 372–377.
- Fashu, S., Lototsky, M., Davids, M. W., Pickering, L., Linkov, V., Tai, S., Renheng, T., Fangming, X., Fursikov, P. V., and Tarasov, B. P. (2020). "A review on crucibles for induction melting of titanium alloys." *Mater. Des.*, 186, 108295.
- Flores, J. F., Neville, A., Kapur, N., and Gnanavelu, A. (2009). "An experimental study of the erosion-corrosion behavior of plasma transferred arc MMCs." *Wear*, 267(1–4), 213–222.
- Franco, D., Ageorges, H., López, E., and Vargas, F. (2021). "Wear behavior at high temperatures of ZrO<sub>2</sub> - Al<sub>2</sub>O<sub>3</sub> plasma sprayed coatings and an electro-melted AZS refractory." *Surf. Coatings Technol.*, 425(August).
- Gao, Q., Yan, H., Qin, Y., Zhang, P., Guo, J., Chen, Z., and Yu, Z. (2019). "Laser cladding Ti-Ni/TiN/TiW+TiS/WS<sub>2</sub> self-lubricating wear resistant composite coating on Ti-6Al-4V alloy." *Opt. Laser Technol.*, 113(October 2018), 182–191.
- Gogia, A. K. (2005). "High-temperature Titanium Alloys." *Def. Sci. J.*, 55(2 SE-Materials Science & Metallurgy).
- Gulbiński, W., and Suszko, T. (2006). "Thin films of Mo<sub>2</sub>N/Ag nanocomposite-the structure, mechanical and tribological properties." *Surf. Coatings Technol.*, 201(3–4), 1469–1476.
- Gupta, D., Bhovi, P. M., Sharma, A. K., and Dutta, S. (2012). "Development and characterization of microwave composite cladding." *J. Manuf. Process.*, 14(3), 243–249.
- Gupta, D., and Sharma, A. K. (2011a). "Development and microstructural characterization of microwave cladding on austenitic stainless steel." *Surf. Coatings Technol.*, 205(21), 5147–5155.
- Gupta, D., and Sharma, A. K. (2011b). "Investigation on sliding wear performance of WC<sub>10</sub>Co<sub>2</sub>Ni cladding developed through microwave irradiation." *Wear*, 271(9–10), 1642–1650.



- Gustavsson, F., and Jacobson, S. (2016). "Diverse mechanisms of friction induced self-organisation into a low-friction material - An overview of WS<sub>2</sub> tribofilm formation." *Tribol. Int.*, 101, 340–347.
- Huang, C., Du, L., and Zhang, W. (2009). "Effects of solid lubricant content on the microstructure and properties of NiCr/Cr<sub>3</sub>C<sub>2</sub>-BaF<sub>2</sub>·CaF<sub>2</sub> composite coatings." *J. Alloys Compd.*, 479(1–2), 777–784.
- Ion, J. C. (2005). "Preface." J. C. B. T.-L. P. of E. M. Ion, ed., Oxford: Butterworth-Heinemann, xiii–xv.
- Jiao, X., Wang, J., Wang, C., Gong, Z., Pang, X., and Xiong, S. M. (2018). "Effect of laser scanning speed on microstructure and wear properties of T15M cladding coating fabricated by laser cladding technology." *Opt. Lasers Eng.*, 110(May), 163–171.
- Jin, K., Qiao, Z., Zhu, S., Cheng, J., Yin, B., and Yang, J. (2016). "Friction and wear properties and mechanism of bronze-Cr-Ag composites under dry-sliding conditions." *Tribol. Int.*, 96, 132–140.
- Karmakar, R., Maji, P., and Ghosh, S. K. (2021). "A Review on the Nickel Based Metal Matrix Composite Coating." *Met. Mater. Int.*, 27(7), 2134–2145.
- Kaushal, S., Gupta, D., and Bhowmick, H. (2018). "On Development and Wear Behavior of Microwave-Processed Functionally Graded Ni-SiC Clads on SS-304 Substrate." *J. Mater. Eng. Perform.*, 27(2), 777–786.
- Khairuzzaman, M. Q. (2016). *Wear problems and testing in industry*.
- Kimura, Y., Wakabayashi, T., Okada, K., Wada, T., and Nishikawa, H. (1999). "Boron nitride as a lubricant additive." *Wear*, 232(2), 199–206.
- Kong, L., Bi, Q., Niu, M., Zhu, S., Yang, J., and Liu, W. (2013). "High-temperature tribological behavior of ZrO<sub>2</sub>-MoS<sub>2</sub>-CaF<sub>2</sub> self-lubricating composites." *J. Eur. Ceram. Soc.*, 33(1), 51–59.
- Kui, X. Y., Wang, J. Z., Liu, Y. P., Xu, J. Y., Gao, Y., and Xu, Z. (2007). "Study on wear resistance of TiN multi-permeation layer using glow plasma surface alloying." *Surf. Coatings Technol.*, 201(9), 5302–5305.
- Kumar, K. P., Mohanty, A., Lingappa, M. S., Srinath, M. S., and Panigrahi, K. (2020). "Enhancement of surface properties of austenitic stainless steel by nickel based alloy cladding developed using microwave energy technique." *Mater. Chem. Phys.*, 256(August), 123657.

- Leunda, J., Sanz, C., and Soriano, C. (2016). "Laser cladding strategies for producing WC reinforced NiCr coatings inside twin barrels." *Surf. Coatings Technol.*, 307.
- Li, J., He, Y., Xiong, D., Qin, Y., Chen, J., and Zhu, H. (2016). "Tribological properties of silver coatings with laser surface textured nickel as interlayer." *Tribol. Int.*, 100, 178–185.
- Li, J., Xiong, D., Wu, H., Dai, J., and Cui, T. (2009). "Tribological properties of molybdenized silver-containing nickel base alloy at elevated temperatures." *Tribol. Int.*, 42(11–12), 1722–1729.
- Lipp, A., Schwetz, K. A., and Hunold, K. (1989). "Hexagonal boron nitride: Fabrication, properties and applications." *J. Eur. Ceram. Soc.*, 5(1), 3–9.
- Liu, C., Wei, D., Xu, R., Mai, Y., Zhang, L., and Jie, X. (2020). "Electroplated Co-Ni/WS<sub>2</sub> Composite Coating with Excellent Tribological and Anticorrosion Performance." *Tribol. Trans.*, 63(5), 857–866.
- Liu, E., Zhang, J., Chen, S., Du, S., Du, H., Cai, H., and Wang, L. (2021a). "High temperature negative wear behaviour of VN/Ag composites induced by expansive oxidation reaction." *Ceram. Int.*, 47(11), 15901–15909.
- Liu, Q., He, T., Guo, W. Y., Bai, Y., Ma, Y. S., Chang, Z. D., Liu, H. B., Zhou, Y. X., Ding, F., Sun, Y. W., Han, Z. F., and Tang, J. J. (2019). "Tribological behavior of SAPS sprayed Al<sub>2</sub>O<sub>3</sub>-TiO<sub>2</sub> and NiCr-Cr<sub>3</sub>C<sub>2</sub> coatings under severe load conditions." *Surf. Coatings Technol.*, 370(October 2018), 362–373.
- Liu, X., Meng, X., Liu, H., Shi, G., Wu, S., and Sun, C. (2014). "Development and characterization of laser clad high temperature self-lubricating wear resistant composite coatings on Ti–6Al–4V alloy." *J. Mater.*, 55, 404–409.
- Liu, X., Shi, X., Huang, Y., Deng, X., Lu, G., Yan, Z., and Xue, B. (2018). "Tribological behavior and self-healing functionality of M50 material covered with surface micropores filled with Sn-Ag-Cu." *Tribol. Int.*, 128, 365–375.
- Liu, Y., Ding, Y., Yang, L., Sun, R., Zhang, T., and Yang, X. (2021b). "Research and progress of laser cladding on engineering alloys: A review." *J. Manuf. Process.*, 66(December 2020), 341–363.
- Liyanage, T., Fisher, G., and Gerlich, A. P. (2012). "Microstructures and abrasive wear performance of PTAW deposited Ni-WC overlays using different Ni-alloy chemistries." *Wear*, 274–275, 345–354.

- Lu, S., Zhou, J., Wang, L., and Liang, J. (2021). "Effect of V and Cr transition layers on microstructure and mechanical properties of Ni-based coating on titanium alloy fabricated by laser cladding." *Surf. Coatings Technol.*, 405(December 2020), 126734.
- Lu, X. L., Liu, X. B., Yu, P. C., Qiao, S. J., Zhai, Y. J., Wang, M. Di, Chen, Y., and Xu, D. (2016). "Synthesis and characterization of Ni60-hBN high temperature self-lubricating anti-wear composite coatings on Ti6Al4V alloy by laser cladding." *Opt. Laser Technol.*, 78, 87–94.
- Luo, X., Li, J., and Li, G. J. (2015). "Effect of NiCrBSi content on microstructural evolution, cracking susceptibility and wear behaviors of laser cladding WC/Ni-NiCrBSi composite coatings." *J. Alloys Compd.*, 626, 102–111.
- M S, S., Sharma, A., and Kumar, P. (2011a). "Microwave processing of metallic joints and their characterization." *I – Manag. J. Mech. Eng.*, 1, 21–25.
- M S, S., Sharma, A., and Kumar, P. (2011b). "Investigation on microstructural and mechanical properties of microwave processed dissimilar joints." *J. Manuf. Process.*, 13, 141–146.
- Mao, Y., Yan, J., Wang, L., Dong, W., Jia, Y., Hu, X., and Wang, X. (2018). "Formation and properties of bioactive barium titanate coatings produced by plasma electrolytic oxidation." *Ceram. Int.*, 44(11), 12978–12986.
- Mason, S. E., and Rawlings, R. D. (1989). "Structure and hardness of Ni–Mo–Cr–Si wear and corrosion resistant alloys." *Mater. Sci. Technol.*, 5(2), 180–185.
- Mason, S. E., and Rawlings, R. D. (1994). "Effect of iron additions on microstructure and mechanical properties of Ni–Cr–Mo–Si hardfacing alloy." *Mater. Sci. Technol.*, 10(10), 924–928.
- Md Idriss, A. N., Maleque, M. A., Yaacob, I. I., Nasir, R. M., Mridha, S., and Baker, T. N. (2017). "Wear behaviour at 600°C of surface engineered low-alloy steel containing TiC particles." *Mater. Sci. Technol. (United Kingdom)*, 33(14), 1688–1695.
- Medabalimi, S. R., Ramesh, M. R., and Kadoli, R. (2019). "High-temperature wear and frictional behavior of partially oxidized Al with NiCr composite coating." *Mater. Res. Express*, 6(12).
- Mendez, P. F., Barnes, N., Bell, K., Borle, S. D., Gajapathi, S. S., Guest, S. D., Izadi, H., Gol, A. K., and Wood, G. (2014). "Welding processes for wear resistant

- overlays.” *J. Manuf. Process.*, 16(1), 4–25.
- Ming, Q., Lim, L. C., and Chen, Z. D. (1998). “Laser cladding of nickel-based hardfacing alloys.”
- Mishra, P., Sethi, G., and Upadhyaya, A. (2006). “Modeling of microwave heating of particulate metals.” *Metall. Mater. Trans. B Process Metall. Mater. Process. Sci.*, 37(5), 839–845.
- Mishra, R. R., and Sharma, A. K. (2017a). “On melting characteristics of bulk Al-7039 alloy during in-situ microwave casting.” *Appl. Therm. Eng.*, 111, 660–675.
- Mishra, R. R., and Sharma, A. K. (2017b). “Effect of susceptor and mold material on microstructure of in-situ microwave casts of Al-Zn-Mg alloy.” *Mater. Des.*, 131, 428–440.
- Mo, J. L., and Zhu, M. H. (2009). “Sliding tribological behaviors of PVD CrN and AlCrN coatings against Si<sub>3</sub>N<sub>4</sub> ceramic and pure titanium.” *Wear*, 267(5–8), 874–881.
- Mondal, A., Upadhyaya, A., and Agrawal, D. (2009). “Microwave sintering of W-18Cu and W-7Ni-3Cu alloys.” *J. Microw. Power Electromagn. Energy*, 43(1), 43111–43116.
- Nair, R. B., Arora, H. S., Boyana, A. V, Saiteja, P., and Grewal, H. S. (2019). “Tribological behavior of microwave synthesized high entropy alloy claddings.” *Wear*, 436–437(January), 203028.
- Niranatlumpong, P., and Koiprasert, H. (2011). “Phase transformation of NiCrBSi–WC and NiBSi–WC arc sprayed coatings.” *Surf. Coatings Technol.*, 206(2), 440–445.
- Ohlsson, T. (1989). “Dielectric Properties and Microwave Processing.” *Food Prop. Comput. Eng. Food Process. Syst.*, R. P. Singh and A. G. Medina, eds., Dordrecht: Springer Netherlands, 73–92.
- Panda, S. S., Singh, V., Upadhyaya, A., and Agrawal, D. (2006). “Sintering response of austenitic (316L) and ferritic (434L) stainless steel consolidated in conventional and microwave furnaces.” *Scr. Mater.*, 54(12), 2179–2183.
- Peterson, M. B., Murray, S. F., and Florek, J. J. (1959). “Consideration of Lubricants for Temperatures above 1000 F.” *A S L E Trans.*, 2(2), 225–234.
- Phanendra Kumar, K., Mohanty, A., Lingappa, M. S., Srinath, M. S., and Panigrahi, S. K. (2020). “Enhancement of surface properties of austenitic stainless steel by nickel based alloy cladding developed using microwave energy technique.” *Mater.*

*Chem. Phys.*, 256, 123657.

Prasad, C. D., Joladarashi, S., Ramesh, M. R., Srinath, M. S., and Channabasappa, B. H. (2018). "Influence of microwave hybrid heating on the sliding wear behaviour of HVOF sprayed CoMoCrSi coating." *Mater. Res. Express*, 5(8).

Prasad, C. D., Joladarashi, S., Ramesh, M. R., Srinath, M. S., and Channabasappa, B. H. (2019a). "Microstructure and tribological behavior of flame sprayed and microwave fused CoMoCrSi/CoMoCrSi-Cr<sub>3</sub>C<sub>2</sub> coatings." *Mater. Res. Express*, 6(2).

Prasad, C. D., Joladarashi, S., Ramesh, M. R., Srinath, M. S., and Channabasappa, B. H. (2019b). "Effect of microwave heating on microstructure and elevated temperature adhesive wear behavior of HVOF deposited CoMoCrSi-Cr<sub>3</sub>C<sub>2</sub> coating." *Surf. Coatings Technol.*, 374(May), 291–304.

Qu, C. C., Li, J., Juan, Y. F., Shao, J. Z., Song, R., Bai, L. L., and Chen, J. L. (2019). "Effects of the content of MoS<sub>2</sub> on microstructural evolution and wear behaviors of the laser-clad coatings." *Surf. Coatings Technol.*, 357(September 2018), 811–821.

Quan, X., Hu, M., Gao, X., Fu, Y., Weng, L., Wang, D., Jiang, D., and Sun, J. (2016). "Friction and wear performance of dual lubrication systems combining WS<sub>2</sub>-MoS<sub>2</sub> composite film and low volatility oils under vacuum condition." *Tribol. Int.*, 99, 57–66.

Ramesh, M. R., Prakash, S., Nath, S. K., Sapra, P. K., and Krishnamurthy, N. (2011). "Evaluation of Thermocyclic Oxidation Behavior of HVOF-Sprayed NiCrFeSiB Coatings on Boiler Tube Steels." *J. Therm. Spray Technol.*, 20(5), 992–1000.

Ramesh, M. R., Prakash, S., Nath, S. K., Sapra, P. K., and Venkataraman, B. (2010). "Solid particle erosion of HVOF sprayed WC-Co/NiCrFeSiB coatings." *Wear*, 269(3), 197–205.

Sabzi, M., Dezfuli, S. M., and Far, S. M. (2018a). "Deposition of Ni-tungsten carbide nanocomposite coating by TIG welding: Characterization and control of microstructure and wear/corrosion responses." *Ceram. Int.*, 44(18), 22816–22829.

Sabzi, M., Dezfuli, S. M., and Far, S. M. (2018b). "Deposition of Ni-tungsten carbide nanocomposite coating by TIG welding: Characterization and control of microstructure and wear/corrosion responses." *Ceram. Int.*, 44(18), 22816–22829.

Sahoo, C. K., and Masanta, M. (2017). "Microstructure and tribological behaviour of TiC-Ni-CaF<sub>2</sub> composite coating produced by TIG cladding process." *J. Mater.*

*Process. Technol.*, 243, 229–245.

Saitou, K. (2006). “Microwave sintering of iron, cobalt, nickel, copper and stainless steel powders.” *Scr. Mater.*, 54(5), 875–879.

Savan, A., Pflüger, E., Goller, R., and Gissler, W. (2000). “Use of nanoscaled multilayer and compound films to realize a soft lubrication phase within a hard, wear-resistant matrix.” *Surf. Coatings Technol.*, 126, 159–165.

Sharma, A. K., and Gupta, D. (2012). “On microstructure and flexural strength of metal-ceramic composite cladding developed through microwave heating.” *Appl. Surf. Sci.*, 258(15), 5583–5592.

Shi, X., Song, S., Zhai, W., Wang, M., Xu, Z., Yao, J., Qamar ud Din, A., and Zhang, Q. (2014). “Tribological behavior of Ni<sub>3</sub>Al matrix self-lubricating composites containing WS<sub>2</sub>, Ag and hBN tested from room temperature to 800°C.” *Mater. Des.*, 55, 75–84.

Shi, X., Zhai, W., Wang, M., Xu, Z., Yao, J., Siyuan, S., and Wang, Y. (2013). “Tribological behaviors of NiAl based self-lubricating composites containing different solid lubricants at elevated temperatures.” *Wear*, 310.

Si-yue, D. (2012). “Fabrication and High Temperature Tribological Properties of Plasma Sprayed WC-Co-Cu-BaF<sub>2</sub>/CaF<sub>2</sub> Self-lubricating Wear Resistant Coatings.” *China Surf. Eng.*

Silva, L. J. da, Scheuer, C. J., and D’Oliveira, A. S. C. M. (2019). “Effect of microstructure on wear performance of NiCrSiBC coatings.” *Wear*, 428–429(January), 387–394.

Singh, B., and Zafar, S. (2019). “Effect of microwave exposure time on microstructure and slurry erosion behavior of Ni + 20% Cr 7 C 3 composite clads.” *Wear*, 426–427, 491–500.

Singh, B., and Zafar, S. (2020). “Understanding time-temperature characteristics in microwave cladding.” *Manuf. Lett.*, 25, 75–80.

Singh, J., and Mazumder, J. (1987). “Effect of extended solid solution of Hf on the microstructure of the laser clad Ni-Fe-Cr-Al-Hf alloys.” *Acta Metall.*, 35(8), 1995–2003.

Sitek, R., Kaminski, J., Borysiuk, J., Matysiak, H., Kubiak, K., and Kurzydowski, K. J. (2013). “Microstructure and properties of titanium aluminides on Ti6Al4V titanium

alloy produced by chemical vapor deposition method.” *Intermetallics*, 36, 36–44.

Sliney, H., Lukaszewicz, V., and Dellacorte, C. (1994). “The Tribology of PS212 Coatings and PM212 Composites for the Lubrication of Titanium 6Al-4V Components of a Stirling Engine Space Power System.” *Tribol. Trans.*, 38.

Sundaramoorthy, R., Tong, S. X., Parekh, D., and Subramanian, C. (2017). “Effect of matrix chemistry and WC types on the performance of Ni-WC based MMC overlays deposited by plasma transferred arc (PTA) welding.” *Wear*, 376–377, 1720–1727.

Surender, M., Basu, B., and Balasubramaniam, R. (2004). “Wear characterization of electrodeposited Ni-WC composite coatings.” *Tribol. Int.*, 37(9), 743–749.

TAKAYAMA, S., LINK, G., MATSUBARA, A., SANO, S., SATO, M., and THUMM, M. (2008). “Microwave Frequency Effect for Reduction of Magnetite.” *Plasma Fusion Res.*, 3(September 2014), S1036–S1036.

Tan, H., Sun, Q., Chen, W., Zhu, S., Cheng, J., and Yang, J. (2021). “Tribological performance and wear mechanisms of a high-temperature wear-resistant Al-Si/SiAlON composite.” *Tribol. Int.*, 164(August), 107227.

Tian, X. J., Zhang, S. Q., Li, A., and Wang, H. M. (2010). “Effect of annealing temperature on the notch impact toughness of a laser melting deposited titanium alloy Ti-4Al-1.5Mn.” *Mater. Sci. Eng. A*, 527(7–8), 1821–1827.

Torres, H., Caykara, T., Rojacz, H., Prakash, B., and Rodríguez Ripoll, M. (2020). “The tribology of Ag/MoS<sub>2</sub>-based self-lubricating laser claddings for high temperature forming of aluminium alloys.” *Wear*, 442–443(May), 203110.

Torres, H., Vuchkov, T., Slawik, S., Gachot, C., Prakash, B., and Rodríguez Ripoll, M. (2018). “Self-lubricating laser claddings for reducing friction and wear from room temperature to 600 °C.” *Wear*, 408–409(May), 22–33.

Tudela, I., Cobley, A. J., and Zhang, Y. (2019). “Tribological performance of novel nickel-based composite coatings with lubricant particles.” *Friction*, 7(2), 169–180.

Tyagi, R., Xiong, D., and Li, J. (2011). “Effect of load and sliding speed on friction and wear behavior of silver/h-BN containing Ni-base P/M composites.” *Wear*, 270(7–8), 423–430.

Ulutan, M., Yildirim, M. M., Buytoz, S., and Çelik, O. N. (2011). “Microstructure and wear behavior of TIG surface-alloyed AISI 4140 steel.” *Tribol. Trans.*, 54(1), 67–79.

Vilar, R. (1999). “Laser cladding.” *J. Laser Appl.*, 11(2), 64–79.

- Wang, C., Gao, Y., Zeng, Z., and Fu, Y. (2017a). "Effect of rare-earth on friction and wear properties of laser cladding Ni-based coatings on 6063Al." *J. Alloys Compd.*, 727, 278–285.
- Wang, H. M., Yu, R. L., and Li, S. Q. (2002). "Microstructure and tribological properties of laser clad NiO/Al<sub>2</sub>O<sub>3</sub> self-lubrication wear-resistant ceramic matrix composite coatings." *Mocaxue Xuebao/Tribology*, 22(SUPPL.), 157–160.
- WANG, H. yu, ZUO, D. wen, SUN, Y. li, XU, F., and ZHANG, D. (2009). "Microstructure of nanometer Al<sub>2</sub>O<sub>3</sub> dispersion strengthened Ni-based high-temperature protective coatings by laser cladding." *Trans. Nonferrous Met. Soc. China (English Ed.)*, 19(3), 586–591.
- Wang, L., Zhou, J., Yu, Y., Guo, C., and Chen, J. (2012). "Effect of powders refinement on the tribological behavior of Ni-based composite coatings by laser cladding." *Appl. Surf. Sci.*, 258(17), 6697–6704.
- Wang, T.-G., Li, B.-S., Yan, B., Fan, Q.-X., Liu, Y.-M., Gong, J., and Sun, C. (2017b). "Tribological Behavior of Multi-layered WC-Co/MoS<sub>2</sub>-Ni Self-lubricating Coating Fabricated by Detonation Gun Spraying." *Cailiao Gongcheng/Journal Mater. Eng.*, 45, 73–79.
- Wang, W. (2004). "Application of a high temperature self-lubricating composite coating on steam turbine components." *Surf. Coatings Technol.*, 177–178, 12–17.
- Wang, Z., Cai, Z., Sun, Y., Peng, J., and Zhu, M. (2017c). "Low velocity impact wear behavior of MoS<sub>2</sub>/Pb nanocomposite coating under controlled kinetic energy." *Surf. Coatings Technol.*, 326.
- Weglowski, M. S., Błacha, S., and Phillips, A. (2015). *6 - Electron beam welding-Techniques and trends. Weld. Join. Aerosp. Mater.*, Elsevier Ltd.
- Weng, Z., Wang, A., Wu, X., Wang, Y., and Yang, Z. (2016). "Wear resistance of diode laser-clad Ni/WC composite coatings at different temperatures." *Surf. Coatings Technol.*, 304, 283–292.
- Xiang, Z.-F., Liu, X.-B., Ren, J., Luo, J., Shi, S.-H., Chen, Y., Shi, G.-L., and Wu, S.-H. (2014). "Investigation of laser cladding high temperature anti-wear composite coatings on Ti6Al4V alloy with the addition of self-lubricant CaF<sub>2</sub>." *Appl. Surf. Sci.*, 313, 243–250.
- Yaedu, A. E., and D'Oliveira, A. S. C. M. (2005). "Cobalt based alloy PTA



hardfacing on different substrate steels.” *Mater. Sci. Technol.*, 21(4), 459–466.

Zafar, S., and Sharma, A. K. (2015). “Dry sliding wear performance of nanostructured WC–12Co deposited through microwave cladding.” *Tribol. Int.*, 91, 14–22.

Zhang, X., Cheng, J., Niu, M., Tan, H., Liu, W., and Yang, J. (2016). “Microstructure and high temperature tribological behavior of Fe<sub>3</sub>Al–Ba<sub>0.25</sub>Sr<sub>0.75</sub>SO<sub>4</sub> self-lubricating composites.” *Tribol. Int.*, 101.

Zhang, Y., Huang, J., Ye, Z., Cheng, Z., and Li, W. (2017). “Process optimization for novel tungsten/metal gas suspended arc welding depositing iron base self-fluxing alloy coatings.” *Int. J. Adv. Manuf. Technol.*, 89(5–8), 2481–2489.

Zhao, H., Liu, Y. feng, Xu, B., Lu, Y. jun, Zhou, C. lan, Wu, X. yu, and Li, J. jun. (2019). “Fabrication and tribological properties of a self-lubricating wear-resistant coating based on structural coupling.” *Ceram. Int.*, 45(3), 3910–3920.

Zhou, J. li, Cheng, Y. hai, Yang, J. yong, Wang, Q. qing, and Liang, X. bing. (2021). “Effects of WS<sub>2</sub> and Ti<sub>3</sub>AlC<sub>2</sub> additions on the high temperature wear properties of laser cladding YW1/NiCoCrAlY tool coating.” *Ceram. Int.*, (August).

Zhou, S., Huang, Y., Zeng, X., and Hu, Q. (2008). “Microstructure characteristics of Ni-based WC composite coatings by laser induction hybrid rapid cladding.” *Mater. Sci. Eng. A*, 480(1–2), 564–572.

Zhu, S., Bi, Q., Yang, J., and Liu, W. (2012). “Ni<sub>3</sub>Al matrix composite with lubricious tungstate at high temperatures.” *Tribol. Lett.*, 45(2), 251–255.

Zhu, S., Bi, Q., Yang, J., Liu, W., and Xue, Q. (2011). “Ni<sub>3</sub>Al matrix high temperature self-lubricating composites.” *Tribol. Int.*, 44(4), 445–453.

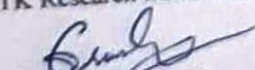
Zhu, S., Cheng, J., Qiao, Z., and Yang, J. (2019). “High temperature solid-lubricating materials: A review.” *Tribol. Int.*, 133(December 2018), 206–223.

Zhu, S., Li, F., Ma, J., Cheng, J., Yin, B., Yang, J., and Qiao, Z. (2015). “Tribology International Tribological properties of Ni<sub>3</sub>Al matrix composites with addition of silver and barium salt.” *Tribology Int.*, 84, 118–123.


## List of Publications based on PhD Research Work

Sl. No.	Title of the paper	Authors (in the same order as in the paper. Underline the Research Scholar's name)	Name of the Journal/ Conference, Vol., No., Pages	Month, Year of Publication	Category*
1.	Evolution of Microstructure and High-Temperature Tribological Performance of Self-Lubricating Nickel-Based Composite Tungsten Inert Gas Coatings	<u>GUDALA SURESH</u> , Ramesh M R and N. Shiva shanmugam	Journal of Materials and Engineering Performance	June, 2021	1
2.	Development of Self-lubricating Nickel Based Composite Clad using Microwave Heating in Improving Resistance to Wear at Elevated Temperatures	<u>GUDALA SURESH</u> , Ramesh M R and M S Srinath	Metals and Materials International	August, 2021	1
3	Microstructure and wear behavior of self-lubricating microwave clads deposited on titanium alloy	<u>GUDALA SURESH</u> , Ramesh M R and M S Srinath	Journal of Materials and Engineering Performance	April, 2022	1
4	Influence of solid lubricants on microstructure and tribological performance of nickel-based composite coatings	<u>GUDALA SURESH</u> , Ramesh M R and N. Shiva shanmugam	Metallography Microstructure and Analysis	February, 2022	1
5	Microstructure and tribological performance of self-lubricate cladding produced by tungsten inert gas and microwave hybrid heating techniques	<u>GUDALA SURESH</u> , Ramesh M R, N. Shiva Shanmugam and M S Srinath	Surface review and letters	Under Review	1

\*Category: 1: Journal paper, full paper reviewed 2: Journal paper, Abstract reviews 3: Conference/Symposium paper, full paper reviewed 4: Conference/Symposium paper, abstract reviewed 5: others (including papers in Workshops, NITK Research Bulletins, Short notes etc.)

  
(Gudala Suresh)

Research Scholar  
Name & Signature, with Date

  
(Dr. Ramesh M R) 13/05/2022

Research Guide  
Name & Signature, with Date

## **BIO-DATA**

- 1. Name** : Gudala Suresh  
**2. Father's Name** : Gudala Rambabu  
**3. Date of Birth** : 25<sup>th</sup> July 1992  
**4. Nationality** : Indian  
**5. Marital Status** : Married  
**6. Address** : Department of Mechanical Engineering  
National Institute of Technology Karnataka  
Surathkal, PO Srinivasnagar 575 025  
Karnataka, India.  
**7. Mobile Number** : +91 9148665136  
**8. E-mail id.** : *gsuresham@gmail.com*  
**9. Educational Qualification** :

---

<b>Qualification</b>	<b>University/Board</b>	<b>Year of Passing</b>
Ph.D. (Mechanical Engineering)	National Institute of Technology Karnataka	Pursuing
M.Tech. (Mechanical Engineering)	National Institute of Technology Silchar	2018
B.E. (Mechanical Engineering)	Uttar Pradesh Technical University	2014

---